THE UNIVERSITY OF HOUSTON
DEPARTMENT OF CHEMICAL ENGINEERING

STUDIES OF MOMENTUM AND ENERGY TRANSFER ACROSS WAVY GAS-LIQUID INTERFACES

FINAL TECHNICAL REPORT ON RESEARCH CARRIED OUT WITH ONR SPONSORSHIP UNDER CONTRACT N00014-90-J-1090

BY A. E. DUKLER
PRINCIPAL INVESTIGATOR

JUNE 1, 1993

Statement A per telecon
Steven Ramberg ONR/Code 1121
Arlington, VA 22217-5000

NWW 6/25/93

67 pgs

DISCLAIMER NOTICE

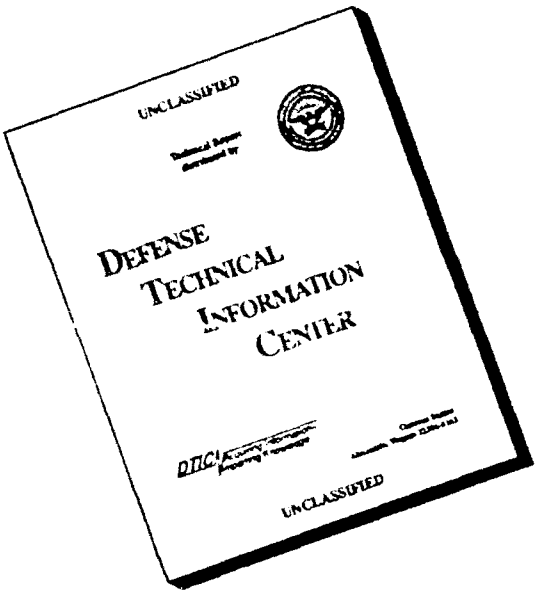

THIS DOCUMENT IS BEST QUALITY AVAILABLE. THE COPY FURNISHED TO DTIC CONTAINED A SIGNIFICANT NUMBER OF PAGES WHICH DO NOT REPRODUCE LEGIBLY.

DISCLAIMER NOTICE

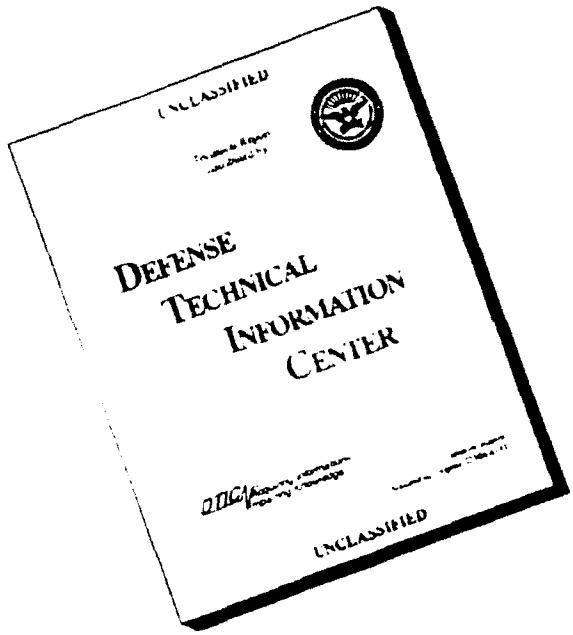

THIS REPORT IS INCOMPLETE BUT IS THE BEST AVAILABLE COPY FURNISHED TO THE CENTER. THERE ARE MULTIPLE MISSING PAGES. ALL ATTEMPTS TO DATE TO OBTAIN THE MISSING PAGES HAVE BEEN UNSUCCESSFUL.

INTRODUCTION

Two phase gas-liquid flow and its associated interfaces exist in a wide variety of situations of importance to the Navy and this has prompted the study of the basic flow mechanics which underlie this complex process. The existence of wind-wave interactions over large bodies of water have long been recognized as a special case of two phase flow where the presence of the deformable interface plays a commplex role in the generation of waves due to the action of the wind. Less well recognized, but of great importance, are situations of two phase flow which are found in componenet of power systems such as condensedrs, boilers refrigeration loops and cryogen lines. Here the characteristics of two phase flow are critical to the reliable design and safe operation of such systems. A basic understanding of gas-liquid flows is also central to the design of safety systems for nuclear reactors. In fact some of the earliest research contributions to the mechanics of two phase flow was motivated by the necd to design such emergency safety systems for the early versions of the Navy nuclear submarine fleet.

During simultaneous flow of gas and liquid in a conduit the phases distribute in a variety of patterns. These include gas bubbleds distributed in the liquid, alternating flows of gas and liquid plugs and annular flow where the two phases are separated with the liquid flowing predominately along the wall and the gas flowing in the core. It is the latter configuration which has been the subject of this study. In this configuration the interface is covered by a complex chaotic system of waves of considerable ampolitude compared to the thin film over which it rides. Furthermore the high speed gas causes detachment of the some of the liquid from the waves and this forms an entrained droplet phase which travels with the gas. IN this research program this complec problem has been attacked from a number of directions.

A. Phase plane and bifurcation analysis of the complex wavy structure of the interface. These results appeared in two published papers attached:

- Phase plane and bifurcation analysis of thin wavy films under shear. AIChE J 35, 177-186 (1989)

• Methods of deterministic chaos applied to flow of thin wavy films. AIChE J 37 481-489 (1991)

B. Experimental and numerical investigations of the mechanics of wavy flow including the solution of the momentum equation for the velocity field under the free wavy surface and the interactions between the waves and this field. These appear in two publications which are attached.

•Insights into the hydrodynamics of free falling wavy film. AICHE J. 35 187-195 (1989)

• Numerical investigation of large wave interactions on free falling films. Int. J. Mult. Flows 15, 357-370 (1989)

C. Studies of mass transfer and the role of the waves on the enhancement of the transfer process. These work is presented in two publications attached.

• A numerical study of mass transfer in free falling wavy film. AIChE J 36, 1379-1390 (1990)

•An experimental study of mass transfer from a wall into a wavy falling film. Chem Eng Sci 47 4323-4331 (1992)

Two studies initiated and carried out under this study and now nearing completion are

• Studies of turbulent gas flow over a wavy interface.

• Entrainment from a wavy interface and drop dynamics of the entrained phase.

PhD theses for each of these areas are now essentially complete. Papers have been accepted for presentation on both subjects at the next annual meeting of the American Institute of Chemical Engineers. Copies of the manuscripts will be forwarded when ready. It is estimated that they will be available about the end of the year.

Methods of Deterministic Chaos Applied to the Flow of Thin Wavy Films

C. E. Lacy, M. Sheintuch, and A. E. Dukler
Dept. of Chemical Engineering, University of Houston, Houston, TX 77204

The structure of thin, wavy falling films was studied to evaluate whether the random-appearing wave structure is a result of deterministic chaos or a purely stochastic process. The time-varying film thickness was obtained at different spatial locations near the point of wave inception for flow rates in the range of Re = 3-10. Under all conditions the wave structure was aperiodic in nature and displayed none of the known transitions to chaos. However, the power spectra followed an exponential decay law at high frequencies that is characteristic of chaotic systems. The estimated attractor dimension, used to characterize the complexity of a chaotic system, was much higher than those of known model chaotic systems. It is demonstrated that these high values could be explained due to small levels of noise present in experimental situations. Since experimental data are seldom noise free, a basic limitation in applying these methods to experimental measurements is demonstrated.

Introduction

The hydrodynamic behavior of thin wavy falling films has been a subject of intensive investigation for about forty years. These films are widely employed in equipment for heat transfer, mass transfer, and chemical reacting systems. In addition to the practical need for understanding the mechanics of this type of flow, there are challenging theoretical problems embedded in the task of modeling these wavy films. This combination has given rise to an extensive literature on this subject.

The earliest work was based on the use of integral equations of the boundary layer type to solve the equations of motion (Kapitza and Kapitza, 1949; Shkadov, 1967). These approaches were based on the assumed existence of a periodic interface and produced first-order estimates for wavelength and velocity. A long series of papers including work by Benney (1966), Lin (1969), and Whitaker (1964), used linear stability analysis to find the wavelength and velocity of the fastest growing wave, again assuming a periodic perturbation. This initial periodic disturbance is thought to evolve into the more complex waveforms observed in experiments as a result of the nonlinear nature of the equations. Nonlinear stability analyses have also been pursued (Pumir, 1983). Recent work on the nonlinear nature of wavy films (Chang, 1987; Sheintuch and Dukler, 1989) searched for infinitely long periodic waves by finding the conditions for existence of the homoclinic orbit.

But even a cursory examination of measured wave traces raises some doubts as to the usefulness of the idea of a small-amplitude periodic wave as the model for the initial phase of the wave motion or of isolated waves as a model for the developed ones. Figure 1d shows a wave trace for a falling liquid film of water-glycerine solution taken with a conductivity probe mounted in a vertical pipe of 50.8 mm dia. as described below. The flow rate corresponds to a Reynolds number of 3.9. The probe was located 0.346 m below a carefully leveled, sharp-edged overflow weir that served as the feed device. The film thickness data are shown after low-pass digital filtering at 25 Hz to remove noise. At this location the wave amplitude is less than 0.25% of the mean film thickness. At all positions closer to the feed the waves were so small that they could barely be detected even with the special circuitry used for this purpose. Note that while the period between successive waves is quite regular, the amplitude is very random. Kapitza and Kapitza (1949) in their classical study of waves on falling films found it necessary to pulse the feed to produce periodic waves. In the absence of pulsing they too reported that the waves were random in appearance. Thus one must question whether the

The present address of M. Sheintuch is Chemical Engineering, The Technion, Haifa, Israel.

to the reconstructed phase space, since the reconstructed and actual phase space have the same topological properties. If the system is one characterized by deterministic chaos, then its dimension, d, is independent of D. It has been shown by Takens (1981) that $D = 2d + 1$ is necessary to obtain a good estimate of d.

In this study the nearest-neighbor method of Badii and Politi (1985) was used to estimate the dimension since it appears to be more accurate (Kostelich and Swinney, 1987) than the more widely used correlation dimension method of Grassberger and Procaccia, (1983) for systems displaying higher dimensions. Consider a set of N points, constructed as in Eq. 1, that lie on the reconstructed attractor. Arbitrarily select a point x on this attractor as a reference point. Now choose at random a subset of k points denoted by $y_i (i = 1,2,\ldots,k$ and $k < N)$ from the original set of N points and consider the distance from x to each point y_i. Define δ as the single minimum of these distances, that is, the distance to the nearest neighbor.

$$\delta = \min \|x - y_i\| \tag{2}$$

To obtain a statistically useful value of the minimum distance, this calculation is repeated over many randomly chosen reference points and an average obtained, $\langle\delta\rangle$. The process is then repeated for a sequence of k values up to $k = N-1$ for each x. The number of nearest neighbors contained in a D-dimensional hypersphere of radius δ around a given point should vary as δ^d if the attractor is d-dimensional. Thus it is argued that

$$\langle\delta\rangle \sim k^{(-1/d)} \tag{3}$$

Hence

$$\log\langle\delta\rangle \sim \frac{-1}{d}\log k \tag{4}$$

The negative, inverse slope of a log $\langle\delta\rangle$ vs. log k plot is the fractal dimension.

All experimental measurements of forced flow systems include electronic noise as well as noise due to random vibrations reaching the system through piping or pumps. Small-amplitude noise can be expected to distort distances between closest nearest neighbors and their reference point. To partly alleviate this error Kostelich and Swinney (1987) suggest that δ be calculated for the tenth or hundredth nearest neighbor. For each choice of D and nearest neighbor, n, an estimate of d can be calculated assuming k is kept sufficiently larger than n. The value of d is said to converge to the attractor dimension when d becomes independent of D and n as both are increased. Additional aspects of the noise problem are discussed later in this paper.

The computed value of d has been shown to depend on the value of the delay time, τ, used to construct the D-dimensional vectors in Eq. 1. If τ is too small, then each $x(t)$ approaches $x(t+\tau)$, and the reconstructed attractor will be a 45° plane in the phase space. For large values of τ, the attractor dimension tends to approach the embedding dimension, D, of the reconstructed phase space due to the stretching and folding nature of chaotic systems (Fraser and Swinney, 1986).

To obtain the optimal delay, a series of two-dimensional reconstructions of $\{x(t), x(t+\tau)\}$ are generated with increasing values of τ. The optimal reconstruction occurs for the smallest value of τ for which $x(t)$ and $x(t+\tau)$ can first be considered independent. The criterion for choosing this value of τ is the first minimum in the index of mutual information, I, as described by Fraser and Swinney (1986). This index is a measure of the degree of predictability of a measurement $x(t+\tau)$ given a measurement $x(t)$.

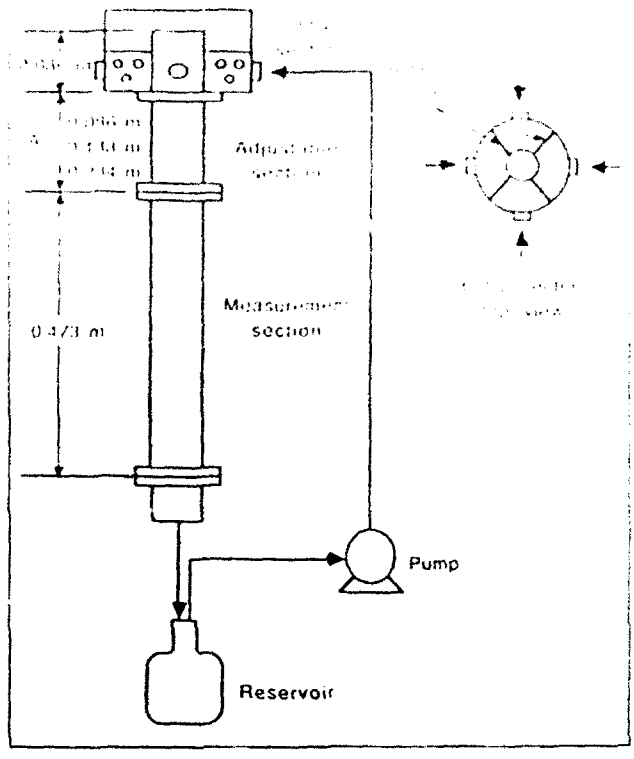

Figure 3. Low *Re* flow system.

Experimental Equipment

Figure 3 is a diagram of the experimental flow loop used for studies of free-falling liquid films at low Re ($Re = 4Q/\nu = 3$–10). Where Q is the volumetric flow rate per unit perimeter and ν is the kinematic viscosity. The measurement section consisted of a 50.8 mm dia. tube 0.47 m long. The liquid feed tank contained a sharp-edged circular weir over which the liquid flowed from the reservoir into the pipe. The distance from the sharp edge to the bottom of the flange was 86 mm. This was followed by a development section having one of three lengths: 86, 138, or 284 mm. Wave motion is not observed immediately after the film is formed at the overflow. The development section provided the length needed at different flow rates to cause the waves to first appear in the measuring section where film thickness probes were located.

Instantaneous film thickness data were obtained using closely spaced parallel wires to make resistivity measurements, which are related to film thickness by calibration. Details of this method including the electronic circuit used appear in the thesis by Zabaras (1985). For these low Re measurements, an array of seven probes was spaced in the direction of flow with distances from the feed point listed in Table 1. A glycerine-water-NaOH solution having a kinematic viscosity of 5.6×10^{-6}

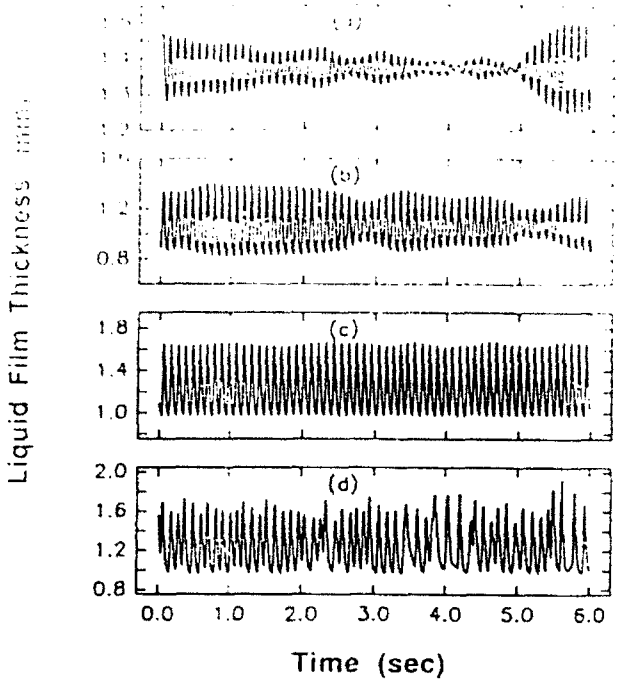

Figure 5. Experimental film thickness traces at $Re = 7.5$.

Distance below overflow weir:
a. 0.21 m; b. 0.26 m; c. 0.41 m; d. 0.61 m

of all the waves returning to a single thickness and the variation of wave amplitude being reflected in differences in the peak value. Figure 7c shows this structure in which the lefthand corner resembles motion in the vicinity of a saddle point. With further distance in the axial direction the wave periods, which heretofore had been regular, now become chaotic, as shown in the time trace, the spectrum, and in Figure 7d.

When two spectral peaks of about equal power exist at wave inception ($Re = 5.6$), the approach to a more uniform wave amplitude is not observed and the waves progress more rapidly to the condition of chaotic wave periods.

The power spectra provide a suggestion that the underlying process may be a manifestation of deterministic chaos. Sigeti and Horsthemke (1987) have shown that for a jth-order sto-

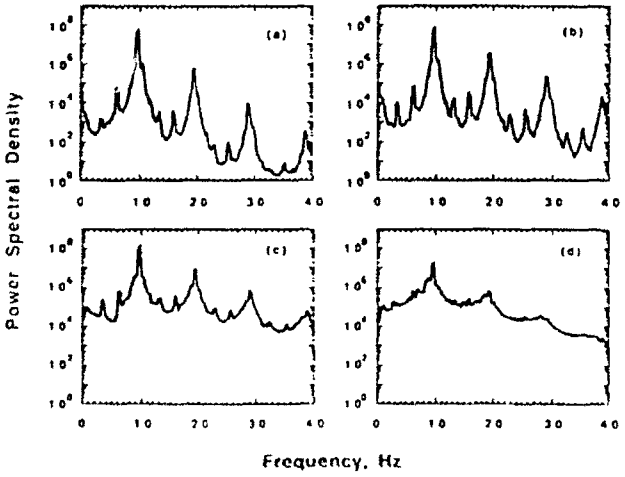

Figure 6. Power spectral density of $Re = 7.5$ data in Figure 5.

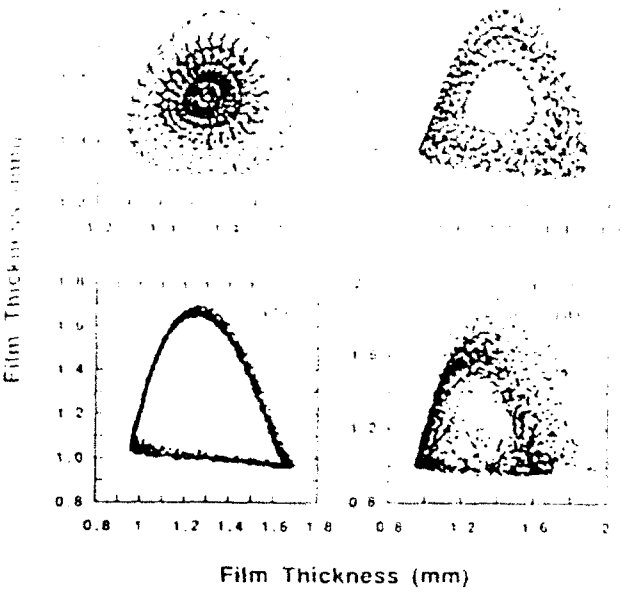

Figure 7. Phase plane portraits of $Re = 7.5$ data in Figure 5.

chastic differential equation the spectral power at high frequencies follows a power law decay, $S = cf^{-N}$. Deterministic equations are, on the other hand, infinitely differentiable and the spectrum must decay exponentially at high frequencies. All spectra observed were characterized by exponential decay.

Attractor Dimension. For each data set listed in Table 1, the nearest-neighbor algorithm for the computation of the attractor dimension was applied using the following parameters:

Total points, N	=	100,000
Embedding dimension, D	=	8–20
Nearest neighbors, n	=	100–600
Subsets of N points, k	=	15,000–100,000

These parameters resulted in processing 2,000–4,000 waves with each wave represented by 30–40 discrete points.

Figure 8 illustrates the method of Badii and Politi (1985) when applied to the time series data from probe 5 at $Re = 7.5$. Figure 8a is a plot of $\log_2 \langle \delta \rangle$ vs. $\log_2 k$ for one D and n pair. An estimate of the attractor dimension, d, is obtained from the slope as given by Eq. 4. The results of repeating this process for each combination of D and n appear in Figure 8b. Here the dimension has converged with increasing D and n, indicating an attractor dimension of about 3.5. There are instances where convergence was not observed with increasing D, as illustrated in Figure 9, although convergence with increasing n was always observed. However, this system does not represent purely stochastic noise, since under that condition one would expect d to be close to D. This behavior seems to be related to the presence of noise in the signal and presents a basic problem in processing and analyzing data from real systems as compared to analyzing data from mathematical models.

Figure 10 shows the trends in complexity of the time traces as position and flow rates are changed. Estimated dimensions appear here that have been computed for $D = 20$, $N = 100{,}000$, $n = 600$ using 1,000 reference points. In some cases definitive

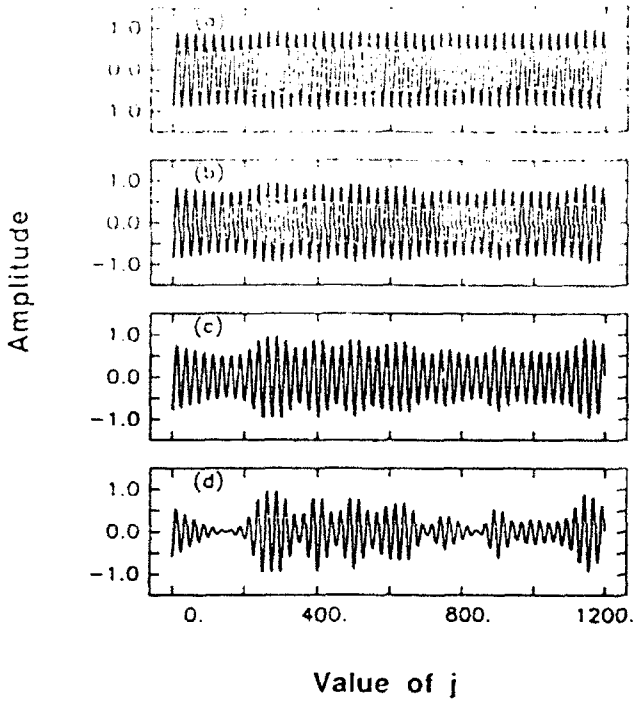

Figure 11. Time trace for a sine wave with multiplicative noise.

a. $z = 0.125$; b. $z = 0.25$
c. $z = 0.5$; d. $z = 1.0$

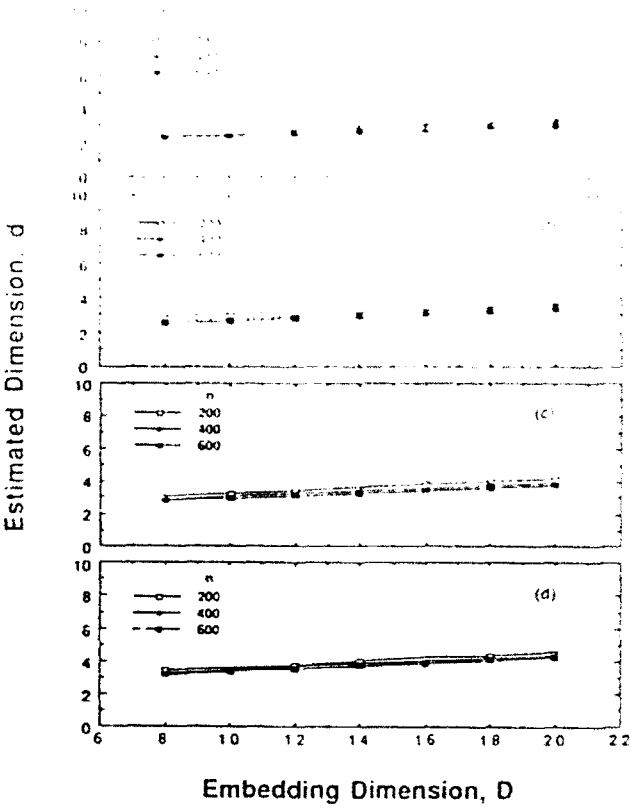

Figure 13. Dimension estimates for a sine wave with multiplicative noise.

a. $z = 0.125$; b. $z = 0.25$
c. $z = 0.5$; d. $z = 1.0$

Attempts to diminish the effects of noise by low-pass filtering had negligible impact on the calculated dimension of the attractor. Methods for eliminating noise have recently been advanced by Kostelich and Yorke (1988), but they appear applicable only when the noise is small (<1%), a condition that does not appear to exist here. Until improved methods are available, it would appear that this method for determining if a process displays the characteristics of deterministic chaos will be of very limited utility when applied to experimental data from physical systems.

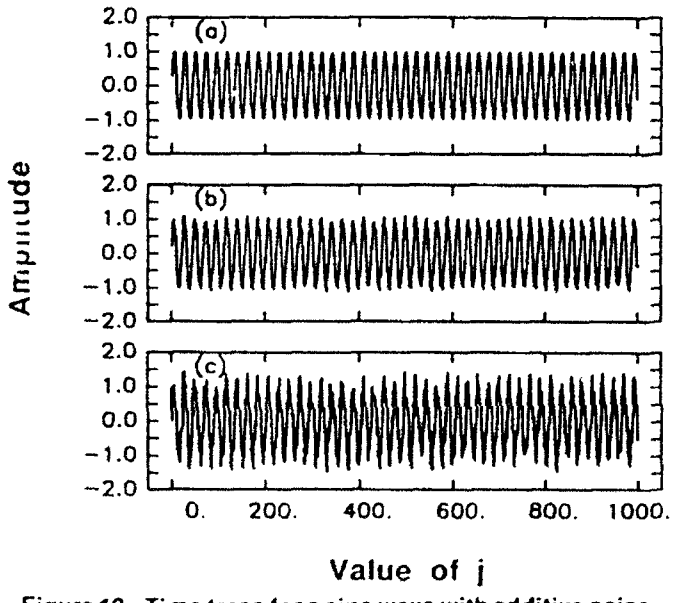

Figure 12. Time trace for a sine wave with additive noise.

a. $z = 0.025$; b. $z = 0.15$; c. $z = 0.5$

High Reynolds number flows

Figure 2 is representative of the time trace obtained at higher flow rates. The spectrum appears in Figure 15. Attractor dimensions were calculated for ten conditions in the range $Re = 310$–$3{,}100$ and include data for free-falling films as well as those with countercurrent and cocurrent interfacial shear. All of these traces were characterized by poor convergence and high dimension. Extensive studies did not reveal any coherent dependence on *Re* or on the amount or direction of the interfacial shear. However, the high-frequency end of the spectrum still indicates an exponential decay, suggesting deterministic chaos. It is likely that noise plays a large role at these high rates where isolation of the system is more difficult.

Discussion

An extensive literature exists for analyzing time-dependent data using methods of fractal geometry. When the data are developed from mathematical models these methods of analysis provide new insights into the behavior of these nonlinear equations. However, attempts to analyze data obtained directly from experiment, as has been presented in this paper, face severe difficulties. Such data are accompanied by significant amounts of noise, and it is shown that noise levels commonly

Grassberger, P., and I. Procaccia, "Measuring the Strangeness of Strange Attractors," *Physica*, **9D**, 189 (1983).

Kapitza, P. L., and S. P. Kapitza, "Wave Flow of Thin Layers of a Viscous Fluid," *Zh. Eksper. i Teor. Fiz.*, **19**, 105 (1949), also in *Coll. Papers of P. L. Kapitza*, Macmillan, New York (1964).

Kostelich, E. J., and H. L. Swinney, "Practical Considerations in Estimating Dimension from Times Series Data," *Chaos and Related Nonlinear Phenomena*, Plenum, New York (1987).

Kostelich, E. J., and J. A. Yorke, "Noise Reduction in Dynamical Systems," *Phys. Rev. A*, **38**(3), 1649, (1988).

Lin, S. P., "Finite Amplitude Stability of Parallel Flow with a Free Surface," *J. Fluid Mech.*, **36**, 113, (1969).

Pumir, A., P. Manneville, and Y. Pomeau, "On Solitary Waves Running Down an Inclined Plane," *J. Fluid Mech.*, **135**, 27 (1983).

Sheintuch, M., and A. E. Dukler, "Phase Plane and Bifurcation Analysis of Thin Wavy Films Under Shear," *AIChE J.*, **35**(2), 177 (1989).

Shkadov, V. Y., "Wave Flow Regimes of a Thin Layer of Viscous Fluid Subject to Gravity," *Izv. Akad. Nauk. Ser. Cekh. Zhidk. i Gaza*, **1**, 43 (1967).

Stucki, D., and W. Horsthemke, "High [illegible] Power Spectra for Systems Subject to Noise," *Phys. Rev. [illegible]*, **[illegible]**, 2[illegible], (1981).

Sivashinsky, G. I., and D. M. Michelson, "On Irregular Wavy Flow of a Liquid Film Down a Vertical Plane," *Prog. Theor. Phys.*, **63**, 2112 (1980).

Takens, F., in *Dynamical Systems and Turbulence*, Lecture Notes in Mathematics, **898**, D. A. Rand, L. S. Young, eds., Springer, Berlin, 137 (1981).

Whitaker, S., "Effect of Surface Active Agents on the Stability of Falling Films," *Ind. Eng. Chem. Fundam.*, **3**, 132, (1964).

Zabaras, G. J., "Studies of Vertical Annular Gas-Liquid Flows," PhD Thesis, Univ. Houston (1985).

Zabaras, G. J., and A. E. Dukler, "Countercurrent Gas-Liquid Annular Flow, Including the Flooding State," *AIChE J.*, **34**(3), 389 (1988).

Manuscript received July 3, 1990, and revision received Jan. 3, 1991.

Reprinted from AICHE JOURNAL, September 1990

A Numerical Study of Mass Transfer in Free Falling Wavy Films

Numerical simulations of mass transfer into falling liquid films, both through the wavy interface and from the wall, have been performed for experimentally measured large waves within which the flow fields have been computed. Experiments have shown that the occurrence of waves on free falling films causes dramatic increases in mass transfer into the film, even under laminar flow conditions. Wave effects have been modeled in several ways, none of which predicts the observed rate of enhancement. The present numerical procedure includes solving the convective-diffusion equation for wavy films by extending a technique developed for hydrodynamic simulation. The presence of waves is shown to cause significant velocities normal to each interface. In conjunction with recirculation within the large waves, these flow patterns produce transfer rates for large waves that are several times larger than predicted for quasiparallel velocity fields. Experimental wave structure data were used to define the dimensions and frequency of an average large wave and surrounding substrate. Computed transfer rates at both the gas-liquid interface and the wall for a film composed of a periodic sequence of average waves agree well with published data. These simulations confirm the inadequacy of parabolic, or Kapitza-type velocity profiles in formulating transport models.

Frederic K. Wasden
A. E. Dukler
Department of Chemical Engineering
University of Houston
Houston, TX 77204

Introduction

The ability of liquid films to transfer large amounts of heat or mass with low hydraulic resistance has led to their use in a wide variety of industrial processes. For unit operations in which the liquid phase is distributed as a film, the throughput of the unit is often determined by the liquid-phase transport resistance; trickle-bed and failing-film reactors, wetted-wall absorbers, and vertical evaporators are examples. Upon contacting a solid surface, liquid films quickly evolve to a complex array of waves whose amplitudes vary from much less to much greater than the mean thickness. This gravity-driven behavior is observed for all flow rates of industrial importance, even in the absence of interfacial stresses due to adjacent gas flow. Figure 1 shows a sample time tracing of the interface of a fully developed laminar film falling freely down a vertical tube without gas flow. The presence of large waves flowing over a thin substrate which itself is covered by small waves is clearly displayed.

Mass transfer in liquids is characterized by extremely long time scales for molecular diffusion. The ratio of thermal to molecular diffusivities in liquids is generally greater than 100, suggesting that mass transfer rates reflect fluctuations in flow field to a greater extent than do heat transfer rates. This speculation has been confirmed by reviews of experimental studies (Seban and Faghri, 1978; Henstock and Hanratty, 1979). This disparity is exploited in the present work to provide a comprehensive examination of a combination of numerical procedures.

A simplified view of a liquid film suggests that transport is limited by diffusion in the direction normal to the transfer surface. The velocity of a contaminant traveling normal to the interface as the result of diffusion is of the order of the ratio of the diffusivity to the film thickness. The comparable velocity in the streamwise direction due to advection is of the order of the average film velocity. The ratio of the advective to the diffusive

F. K. Wasden is presently with Shell Development Company, Westhollow Research Center, Houston, TX.

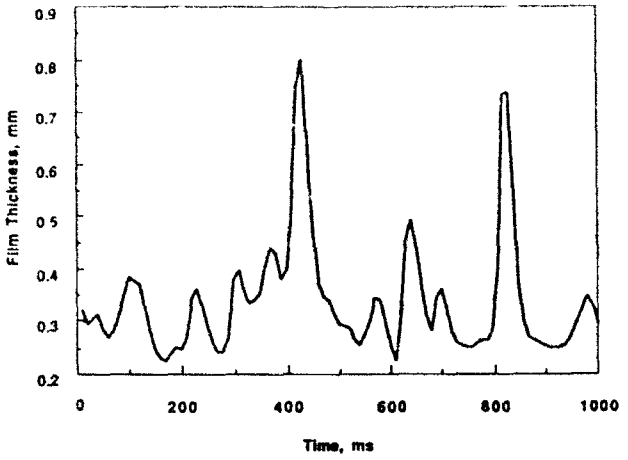

Figure 1. Film thickness time trace, $Re = 880$.

velocity, the Peclet number, is of order 10^4–10^6 for industrially important thin film flows. Experiments have shown that the presence of waves on films causes dramatic increases in heat or mass transfer, even for laminar flows. While a wide range of wave amplitudes exists, it is speculated that the large waves, ranging from two to five times the substrate thickness in amplitude, control the transport rates (Dukler, 1977).

Predicting the enhancement of transport rates due to the wavy interface has provoked many studies of film hydrodynamics. Since first being addressed by Kapitza and Kapitza (1949), studies of the linearized hydrodynamics within wavy films have yet to predict the wide variety of wave shapes, sizes, and speeds observed experimentally. Numerical studies of the problem are limited. Bach and Villadsen (1984) succeeded in predicting velocity profiles in traveling waves using a finite-element technique, but their results were limited to Reynolds numbers less than 100. The film Reynolds number is defined as $Re = 4Q/\nu$, where Q is the mass flow rate per unit perimeter and ν is the kinematic fluid viscosity. Recent numerical studies of hydrodynamics in isolated and interacting large waves at a Reynolds number of 880 (Wasden and Dukler, 1989a, b) have provided information on the flow fields existing in these waves. The hydrodynamic studies predict regions of large streamwise acceleration in the waves as well as recirculating zones. Nakaya (1989) has also found these flow patterns in large waves at low flow rates.

This study focuses on numerical prediction of mass transfer to laminar free falling films for both gas absorption at the free surface and dissolution at the wall in the presence of complicated velocity fields. The former situation has been studied extensively, both experimentally and theoretically, and is reviewed by Henstock and Hanratty (1979). Information on the wall transfer is much more limited.

Existing Models and Experimental Studies

Mass transport in flat films

Early attempts at describing transport in films were limited to situations where the film was assumed to be flat. Transfer from the adjacent gas phase into the film through the free interface is illustrated in Figure 2. The transport is governed by the convective-diffusion equation, which can be written in two

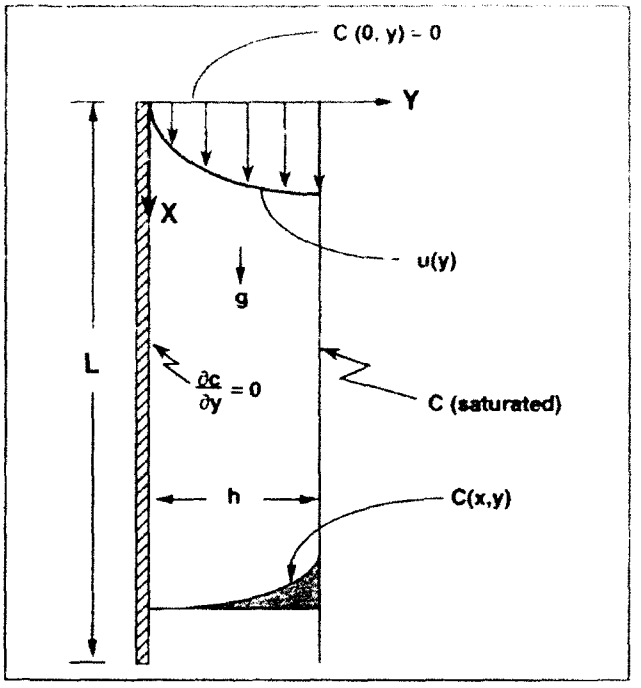

Figure 2. Absorption through the surface of a flat film.

dimensions as

$$\frac{\partial c}{\partial t} + u\frac{\partial c}{\partial x} + v\frac{\partial c}{\partial y} = D\left(\frac{\partial^2 c}{\partial x^2} + \frac{\partial^2 c}{\partial y^2}\right) \tag{1}$$

where $c(x, y, t)$ is the concentration of the species and $u(x, y, t)$ and $v(x, y, t)$ are the velocity components in the streamwise (x) and normal (y) directions. For steady flat film flow, the parabolic velocity profile is used for the axial velocity and the convective-diffusion equation reduces to

$$u(y)\frac{\partial c}{\partial x} = \frac{gh^2}{v}\left(\frac{y}{h} - \frac{y^2}{2h^2}\right)\frac{\partial c}{\partial x} = D\left(\frac{\partial^2 c}{\partial y^2}\right) \tag{2}$$

where streamwise diffusion is negligible at the high Peclet numbers experienced in practice. For absorption, the boundary and initial conditions assume an initially pure solution with a saturated interfacial condition and no flux at the wall:

$$c(x, y) = 0 \quad \text{at} \quad x = 0 \text{ for all } y \tag{3a}$$

$$c(x, h) = c_{\text{saturated}} = c_s \quad \text{at} \quad y = h \text{ for all } x \tag{3b}$$

$$\frac{\partial c}{\partial y} = 0 \quad \text{at} \quad y = 0 \text{ for all } x \tag{3c}$$

The first analytical solution of Eqs. 2 and 3 was presented by Pigford (1941), who assumed that the gas–liquid contact time was short enough that variations in concentration occur only in a boundary layer near the free interface. Replacing the condition of Eq. 3c with $c(x, 0) = 0$ enabled him to find a closed-form solution for the local mass flux at any position x, and for the mass flux averaged over a column length of L. The latter solution

is given below and is referred to as the short contact time theory (SCTT) mass transfer rate,

$$N_{SCTT} = c_i \sqrt{\frac{2Dgh^2L}{\nu\pi}} \tag{4}$$

Mass transfer from the solid wall into the falling liquid film is seldom encountered in industrial practice, although its analog, the process of heat transfer from the wall is quite common. Figure 3 illustrates the mass transfer situation for a flat film in which a portion of the wall is considered to be active, or capable of supplying mass to the film. Boundary and initial conditions are similar to those for the absorption problem. An initially pure solvent is assumed to be saturated at the liquid–solid interface and no transport is allowed at the free interface:

$$c(x, y) = 0 \quad \text{at} \quad x = 0 \tag{3a}$$

$$c(x, 0) = c_i \quad \text{for} \quad y = 0, \quad 0 < x < L_A \tag{5a}$$

$$\frac{\partial c}{\partial y} = 0 \quad \text{at} \quad y = h \tag{5b}$$

$$\frac{\partial c}{\partial y} = 0 \quad \text{at} \quad y = 0 \quad \text{for} \quad x > L_A \tag{5c}$$

No general analytical solution to the governing equations exists for arbitrary lengths of the active region, L_A. For small diffusivities (large Schmidt numbers) and small contact times, a boundary layer analysis similar to Pigford's was proposed by Acrivos (1960). In the limit of low Peclet numbers (high mass diffusivity), Spence and Brown (1968) solved the transport problem using a Frobenius series to solve the ordinary differential equation generated by the Laplace transform of the original partial differential equation. In principle, this method can be extended to the general case, but the Frobenius series does not possess sufficiently robust convergence characteristics to allow its use.

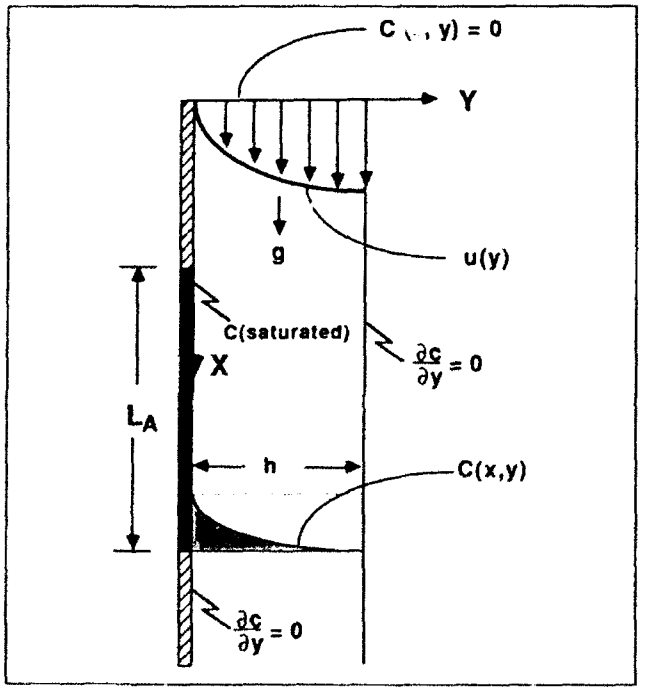

Figure 3. Mass transfer from solid boundary into flat film.

Gas absorption through the wavy interface

Most gas absorption experiments that have been reported provide information on mass flux or mass transfer coefficients averaged over the entire length of film. Simultaneous local measurements of time-varying wavy film thickness and concentrations have not been reported, so little information is available on the local transport process. Emmert and Pigford (1954) reported mass transfer rates in agreement with short contact time predictions, Eq. 4, when a surfactant was added to suppress waves. In the absence of surfactant, mass transfer rates two to three times greater than observed for flat films were measured for Reynolds numbers of 200–1,200 and Schmidt numbers between 400 and 500 in a column 1.1 m long.

Kafesjian et al. (1961) examined the rates at which a species is absorbed and desorbed from a film. No equivalent to the short contact time theory exists for desorption since the concentration is uniform in the incoming fluid. Measured values of desorption from the film suggest an additional 20–30% enhancement over the absorption rate computed from correlations of Emmert and Pigford, implying that waves do more than stretch and contract the velocity profile. By imposing external disturbances and generating standing waves of various amplitudes and frequencies on stationary horizontal films, Goren and Mani (1968) measured mass transfer rates greater than ten times the values expected for smooth films, with increases scaling roughly linearly with wave amplitude.

Data from a variety of investigators published over a three-decade period were correlated to film Reynolds number and Schmidt number by Henstock and Hanratty (1979). The data reflect a variety of columns sizes, with Schmidt numbers ranging from 250 to 1,200 and Reynolds numbers from 100 to 10,000, encompassing laminar and turbulent films. The ratio of the mass transfer coefficient from their correlation to that of the short contact time solution, k_{LSCT}, is:

$$E = \frac{k_L}{k_{LSCT}} = 0.0111 \sqrt{\frac{(L/h_N)}{Re}} [(0.707\sqrt{Re})^5 + (0.0310^{0.9}\sqrt{Re})^5]^{0.30} \tag{6}$$

where k_L is the liquid side mass transfer coefficient averaged over the film length L and h_N is the Nusselt or time-averaged film thickness. Equation 4 can be used to show that

$$k_{LSCT} = \sqrt{\frac{3\,D\nu\,Re}{2\pi\,L\,h_N}} \tag{7}$$

The enhancement, E, depends only on film Reynolds number and length, varying from 1.15 for L/h_N of 3,000 and Reynolds number of 100 to 2.9 for L/h_N of 10,000 and Reynolds number of 1,000. An enhancement of nearly fifteen times is predicted for a turbulent film with a Reynolds number of 10,000 and length L/h_N of 10,000. The additional interfacial area due to the waves over that of a flat interface has been shown to be negligible over a wide range of flow rates (Portalski and Clegg, 1971), so the

enhancement in Eq. 6 is not influenced by differences in interfacial area due to the presence of waves.

The modeling of gas absorption in falling films has proceeded along four paths.

1. Levich (1962) extended the short contact time solution to allow the surface velocity to vary with film thickness. Treating the interface as a periodic array of small-amplitude traveling capillary waves, Levich used the model of Kapitza and Kapitza (1949) to predict the surface velocity and concluded that the enhancement, E, would be about 1.15. Ruckenstein and Berbente (1965, 1968) also used the Kapitza hydrodynamic model and approximated the interface as small-amplitude traveling waves described by two Fourier modes. The concentration profile in the film was approximated by a power series in the coordinate normal to the interface and an enhancement of about 30% was predicted. Since the Kapitza wave model describes only capillary waves the results are applicable only for very low Reynolds numbers.

More recently, Barrdahl (1988) solved the convective-diffusion equation for transport into wavy films at very low Reynolds numbers, near the condition of wave initiation. He showed that mass transfer enhancement due to small waves scales with $Pe^{1/2}$. Howard and Lightfoot (1968) arrived at the same conclusion by treating the interface as a periodically stretching surface. Javdani (1974) suggested a model for wave-induced concentration fluctuations similar to simple eddy viscosity models. Using the Kapitza model for the velocity profile he proved only that enhancement scales as $Pe^{1/2}$.

2. The models discussed above are deficient in their neglect of the presence of large roll waves and the substantial velocities normal to the interface that can be expected to accompany them. Attempts to relate the increased mass transfer to large wave properties using surface renewal models are summarized by Davies (1972) and Dukler (1977). Banerjee et al. (1967) proposed a renewal model which assumed that the large waves mixed with the substrate over which they passed, bringing fresh solution to the interface. Closing the problem required a relation between the Reynolds number and large-wave frequency; this was derived from linear stability considerations. Since linear stability analyses characterize only small capillary waves (Benjamin, 1957), this choice of relationships is questionable. The model was modified by Brumfield et al. (1975), incorporating new data on large-wave frequencies (Telles and Dukler, 1970).

3. Wave-induced turbulence was suggested by Suzuki et al. (1983) as a means of explaining the enhanced mass transfer rates. The method proposed a turbulent diffusivity for both large and small waves whose definition was empirically related to the size and velocity of the waves. Poor agreement between predicted and measured transport rates was reported for instances in which this model was applied to flows with many large waves.

4. Films sheared by the surrounding gas have been studied experimentally (McCready and Hanratty, 1985) and analytically (McCready et al., 1986; Back and McCready, 1988). It is suggested that shear stress variations due to gas flow around waves induce normal velocities near the interface which influence mass transfer. Of course, this mechanism is not applicable to the case of free falling films.

The experimental evidence accumulated over the past three decades shows that mass transfer enhancement due to waves on films cannot be explained with models using any variant of the Kapitza capillary wave velocity profile. Models based on large-wave-induced surface renewal suffer for lack of a complete characterization of wave structure, frequency, and amplitude distribution. Analyses based on more robust hydrodynamic models appear to be the logical next step toward reconciling experimental measurements and predicted transfer rates.

Mass transfer from the wall

Few experimental studies of this problem have been reported. Referring to Figure 3, most experiments have been conducted with a contaminant affixed to a tube wall or flat plate over a distance L_A. A film was allowed to flow over the solute, with careful attention to complete wetting of the surface. Mass transfer rates were determined either by weighing the plate before and after the experiments or by measuring the outlet bulk concentration of the fluid.

Stirba and Hurt (1955) attempted to relate the increased transfer rate due to the waves to a universal eddy diffusivity. Experiments in 2 m long tubes coated with organic acids over lengths from 1 to 1.5 m showed apparent diffusivities ranging from three to twenty times the molecular diffusivity, depending on the Reynolds and Schmidt numbers. Reynolds numbers in the study varied from 300 to 3,000, and Schmidt numbers from 600 to 18,000. No general correlation of the results was presented.

Oliver and Atherinos (1968) conducted experiments in an inclined channel at angles of 30° or less with the horizontal, $Re < 200$, and length of about 0.3 m. They found that transfer rates were described adequately by a short contact time, smooth liquid film theory analogous to that of Pigford for gas–liquid transfer. However, the conditions of the experiment were such that large waves were not present. Oliver and Atherinos suggest that the difference between their result and that of Stirba and Hirt is due to the presence of large waves in the latter experiments while theirs only showed capillary wave motion.

Mass transfer from a wall to a liquid is represented by a substantial body of literature because of interest in the use of electrochemical probes to measure wall shear stress (Hanratty and Campbell, 1983). However, these models all assume the existence of a very thin concentration boundary layer near the wall through which the velocity profile can be assumed to be linear. This condition is a very specialized one and not of general applicability. No analytical theories exist that can be used to explore the effect of wave motion on this wall to fluid transfer. Speculation about the effect of large waves on transfer rates is possible through an examination of the velocity profile near the wall, where the streamwise velocity can be approximated using a Taylor expansion,

$$u(x, y, t) \sim u(x, 0, t) + \left(\frac{\partial u}{\partial y}\right)_{(x,0,t)} y + \ldots \qquad (8)$$

where $u(x, 0, t)$ is identically zero, and the derivative term represents the wall shear stress. Using the continuity equation, the normal velocity is seen to be approximated by

$$v(x, y, t) \sim \frac{y^2}{2} \frac{\partial}{\partial x}\left(\frac{\tau_w}{\mu}\right) \qquad (9)$$

This simple scaling shows that mass transport enhancement is expected near the front and rear or large waves, where wall

hear stress values are rapidly changing (Wasden and Dukler, 1989a, b).

Computational Procedure

The numerical study focused on simulating mass transfer in a series of seven experimentally measured large wave shapes chosen from film thickness traces obtained at a Reynolds number of 880. The wave shapes chosen included both isolated and interacting waves and were representative of all large waves existing on the film. Simulation of mass transfer through either the wavy interface or from the wall combined three numerical algorithms. First, the u and v velocity fields were computed for each wave using a finite-difference numerical algorithm based on the TEACH-T code (Gosman and Ideriah, 1976) and described elsewhere (Wasden and Dukler, 1989a, b). The hydrodynamic simulation was performed under the assumption of passive scalar transport, that is, the presence of the diffusing species did not affect the physical properties of the fluid. Boundary conditions required to specify the concentration distribution in the flat film surrounding the large waves were then computed from a numerical solution of Eqs. 2 and 3 or Eqs. 2 and 5. The final step in the transport simulation was the solution of the convective-diffusion equation using the velocity and spatial shape profiles determined in the hydrodynamic simulations.

Gas absorption through the wavy interface

The gas absorption problem simulated in this study is illustrated in Figure 4. Each large wave is modeled as being surrounded by a flat film in which the concentration field is described by the solution of the flat film problem, Eqs. 2 and 3, for a given position of the wave in the column, L. Mass transfer through the wavy interface is computed as the wave passes a location L below the feed. A locally variable wave velocity, $V_w(z)$, is determined in the course of the hydrodynamic simulation and used to approximate the unsteady terms in Eq. 1,

$$\frac{\partial c}{\partial t} = -V_w(z)\frac{\partial c}{\partial z} \tag{10}$$

The solution is then generated for a steady problem in a coordinate system moving with the wave. The convective-diffusion equation for this planar flow is then written

$$(u - V_w)\frac{\partial c}{\partial z} + v\frac{\partial c}{\partial y} = D\left(\frac{\partial^2 c}{\partial z^2} + \frac{\partial^2 c}{\partial y^2}\right) \tag{11}$$

where the coordinates are shown in Figure 4. At the solid boundary, $y = 0$, a no-flux condition, Eq. 3c, is imposed while the free surface streamline corresponds to a saturated solution, Eq. 3b. The inlet condition, at $z = L$, is determined by a numerical solution of Eqs. 2 and 3 for given Peclet number, substrate thickness, and fluid properties. The outlet condition, at $z = L - \lambda$, corresponds to negligible steamwise concentration gradients, or

$$\left(\frac{\partial c}{\partial z}\right)_{z=L-\lambda} \approx 0 \tag{12}$$

where λ is the wavelength of the large waves and includes only the sloped portions of the wave.

The solution of the transport problem was generated from a modified version of the finite-difference algorithm developed for the hydrodynamic problem (Wasden and Dukler, 1989b). In order to increase accuracy, a novel version of a quadratic upwind differencing technique, QUICK (Leonard, 1979), called NU-QUICK-ER was developed for approximating convective terms in both streamwise and normal directions. A mass source calculated using the concentration gradient at the surface was added to the mass conservation equation for those control volumes bordering the free interface, while no mass was allowed to leave the control volume through the wall. Details of the numerical method and surface treatment techniques appear elsewhere (Wasden, 1989).

The concentration field within each wave determined in this way was used to compute values of the local mass flux at the interface through Fick's law. Of particular interest is the mass flux integrated over the wavelength. The local flux given by the short contact theory can be integrated over the wavelength to yield

$$\int_{z=L-\lambda}^{L}\left[-D\left(\frac{\partial c}{\partial y}\right)_{y=h_N}\right]dz = \sqrt{\frac{gD\,h_N^2}{2\pi\nu}}\left[\sqrt{L} - \sqrt{(L-\lambda)}\right] \tag{13}$$

Grid refinement studies showed that the grid mesh necessary to fully resolve hydrodynamic details in the large waves provided sufficient detail for transport modeling. Approximately 2,000

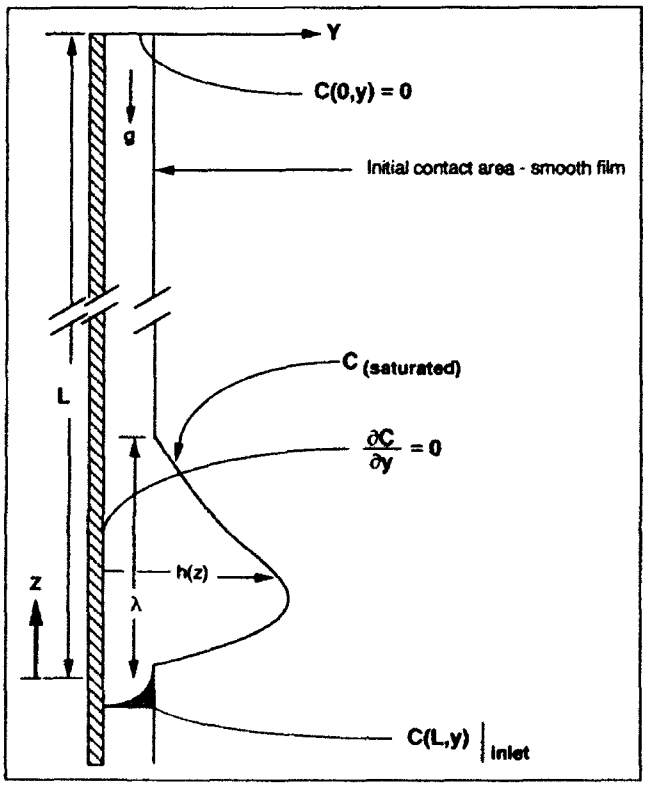

Figure 4. Absorption through large waves.

mesh cells were used in each case. The iterative solution of the transport problem was continued until the sum of mass residuals throughout the wave was less than one part in 10^4 of the total mass transferred across the interface. Execution time for the code was between 200 and 300 CPU seconds on an NAS 9000 mainframe computer.

Mass tansfer from the wall

Mass transfer from the wall was computed by tracking the evolution of concentration profiles with time as the waves traversed the soluble surface. The total amount of mass accumulated by a wave was compared to that numerically computed for a smooth film having the same time of exposure to determine the enhancement due to the presence of the wave.

This simulation procedure required an algorithm designed specifically for unsteady simulations. The physical situation described by the model is shown in Figure 5. For this problem, the unsteady convective-diffusion equation is given by Eq. 1 with the coordinates as defined in Figure 5. Time begins when the wave front reaches the upper end of the active surface, where the film is assumed to be composed of pure solvent, Eq. 3a. Along the soluble surface, the concentration is equal to the value of a saturated solution, Eq. 5a, while no flux is allowed at the wall in regions outside the active region, requiring

$$\left(\frac{\partial c}{\partial y}\right)_{(x,0,t)} = 0, x < 0, x > L_A \tag{14}$$

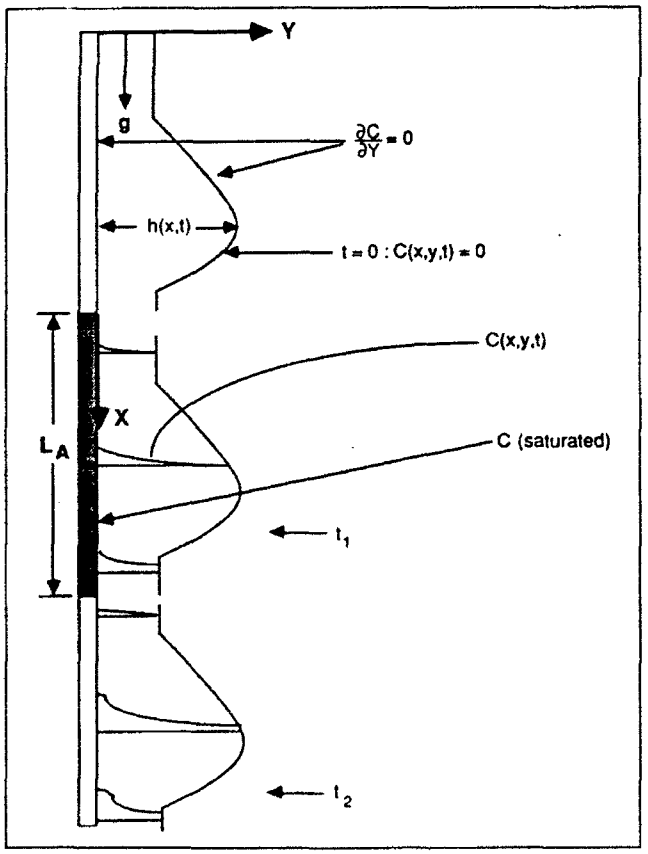

Figure 5. Mass transfer from solid boundary into a passing wave.

No mass is allowed to pass through the wavy interface, or

$$\left(\frac{\partial c}{\partial y}\right)_{(x,h(x,t),t)} = 0, -\infty < x < \infty, t > 0 \tag{15}$$

The problem formulation includes two parameters, the length of the active surface, L_A, and the Schmidt number. As in the case of mass transfer to the interface, the simulation used the same rectangular grid mesh as the hydrodynamic simulation; roughly 2,000 grid points were specified for each large wave. The small grid spacing used near the wall to resolve the wall shear stress in the hydrodynamic problem was suitable for the mass transfer problem where the concentration varied rapidly near the wall.

The unsteady term in the convection-diffusion equation was approximated with a first-order implicit finite-difference technique as recommended by Patankar (1980). The unsteady term adds a source term to the discretized equations that is easily assimilated into the control-volume-based method on which the algorithm was based. The implicit method is unconditionally stable for the present problem, insuring that the temporal behavior of the results are reasonable approximations to the true solution. To reduce errors in the solution, time step sizes of less than 1 ms were used.

The solution procedure began with the concentration field set to zero. As time advanced one step, the wave moved a distance determined by the velocity near the wall for the first grid cell. The first streamwise wall cell was specified as having a constant concentration boundary condition, therefore allowing a flux of solute, while all other wall cells were bounded by the solid wall, with a no-flux condition imposed. At this location and time, the concentration field was determined by solving the system of linear equations representing the finite-difference form of Eq. 1 using an alternating direction implicit (ADI) technique. This iterative technique was continued until the solution had converged to within one part in 10^4. The wave was then allowed to move downward another time step. The distance moved with each time step depended on the velocity associated with each grid near the wall; the algorithm adjusted the time step such that each step corresponded to moving the wave sufficiently that one more whole grid cell was subject to a flux condition. The grid mesh spacing in the streamwise direction was specified such that smaller grids were assigned to regions in which the velocity fields were changing rapidly. This grid spacing scheme insured that smaller time steps were taken in these regions, and that the mass transport was accurately approximated. Implicit in the simulation is the condition that each wave continues to evolve in the same way that was determined for a single location. This assumption is justified for an isolated wave changing very little with distance. In contrast, evolving and interacting waves are probably not well described by this criteria over a long distance. The present simulation will be limited to reasonably short active surface lengths in order to minimize this error.

Concentration fields were determined for each wave for fixed values of the active surface length and various Schmidt numbers. The algorithm required about 1 CPU second (on an NAS 9000 computer) for each time step, and for most cases, 200–300 CPU seconds were sufficient to complete each simulation.

Average Wave Structure of the Falling Film

An average wave structure was defined from time records of film thickness measurements taken at $Re = 880$ to determine

whether the statistically defined average wave, if distributed along the surface, would yield computed mass transfer rates comparable to experimental values. The film is modeled as periodic average waves separated by a rippled substrate.

Film thickness data from which the large wave profiles were taken were examined to determine the characteristics of an average large wave. Figure 6 illustrates the components of the proposed film structure, a series of triangular waves traveling over a flat substrate. Data consisting of 45 s of film thickness signals taken at two locations and sampled at 1kHz per channel were analyzed using traditional statistical techniques to arrive at the dimensions and velocity of the wave structure.

The wave velocity was determined by dividing the distance separating two film thickness probes (63 mm) by the time delay of the maximum of the cross-covariance of the signals. The time of the first zero of the film thickness autocorrelation provided an average wave frequency, f, from which the total length of the wave in the time domain was determined as

$$\frac{1}{f} = t_f + t_b + t_s \tag{16}$$

where t_f, t_b, and t_s are the lengths (in a time domain) of the front of the wave, the tail, and the separating substrate. Averaging over the ensemble of all measured waves separated by a substrate thinner than the mean thickness provided average values for t_f and t_b. The extent of the substrate, t_s, is then determined using Eq. 16.

The average substrate thickness, h_s, was chosen as the value below which 5% of the film thickness points fell. This value approximates the average of the minimum values of film thickness between large waves. With this value, the problem was closed using the volume conservation equation

$$h_N = h_s + \left(\frac{h_p - h_s}{2}\right)\frac{(t_b + t_f)}{(t_s + t_f + t_b)} \tag{17}$$

which can be solved for the peak thickness,

$$h_p = \left[\frac{2\,(h_N - h_s)\,(t_b + t_f + t_s)}{(t_b + t_f)}\right] + h_s \tag{18}$$

The experimental data analyzed with this method had an average thickness, h_N, of 0.365 mm, an average substrate thickness, h_s, of 0.260 mm, and an average peak thickness, h_p, equal to 0.614 mm. The peak to substrate ratio is 2.36. An average frequency of 6.9 Hz was computed, along with average t_f of 33.3 ms and t_b of 51.0 ms. The substrate duration, t_s, was computed to be 60.7 ms. The wave velocity for the film was determined to be 1.15 m/s. Streamlines resulting from the hydrodynamic simulation of the average wave are shown in Figure 7.

Results

Gas absorption through the wavy interface

Simulations were carried out for seven large waves whose profiles were measured 3.1 m below the feed and which were representative of all isolated and interacting waves. For each wave, the Schmidt number was varied from 250 to 1,000, while the distance below the feed ranged from 1,000 to 6,000 Nusselt thicknesses. This parameter space encompasses nearly all industrially important gas–liquid diffusion systems and column heights. For each of the parameter pairs, a concentration field was determined. The local variation of mass flux could then be computed from the gradient of this concentration at the interface and the total flux through the interface determined from the integration of this local flux along the wave. Two waves will be discussed in detail: an isolated wave with peak/substrate thickness of approximately three and an interacting wave. Streamline maps for these waves are given in Figures 8 and 9.

Concentration fields computed for the isolated large wave are shown in Figure 10 for Schmidt numbers of 500 and 1,000 at a distance of 4,500 mean film thicknesses below the feed (1.63 m for a Reynolds number of 880). These conditions are comparable to those investigated experimentally by Emmert and Pigford (1954). The concentration profiles are presented as contour plots with intervals of 0.1 saturated concentration units dividing successive contour lines. Both concentration profiles show significant deviations from parallel isoconcentration lines predicted by the short contact time theory (SCTT). Normal (v) velocities within the wave peak carry solute from the surface into the wave. Near the front and rear of the wave, normal velocities resulting from the wave peak interacting with the substrate force the solute into the substrate. The effect of the Schmidt number is seen in the extent to which the concentration field penetrates the wave substrate; for a higher Schmidt number, this penetration occurs to a lesser extent.

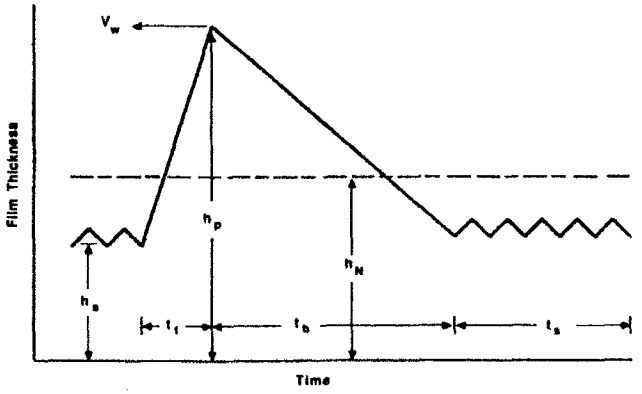

Figure 6. Average film structure dimensions.

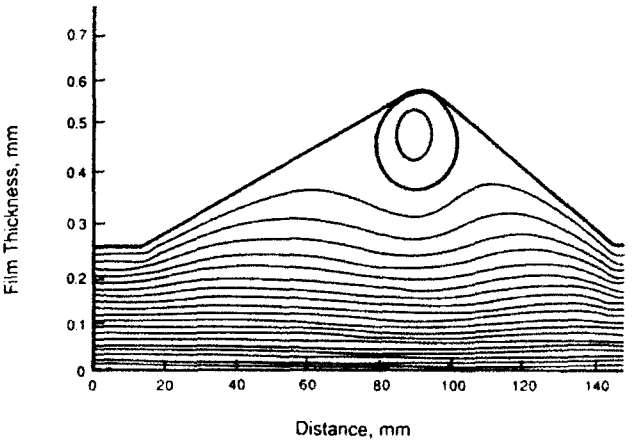

Figure 7. Streamline map for average large wave.

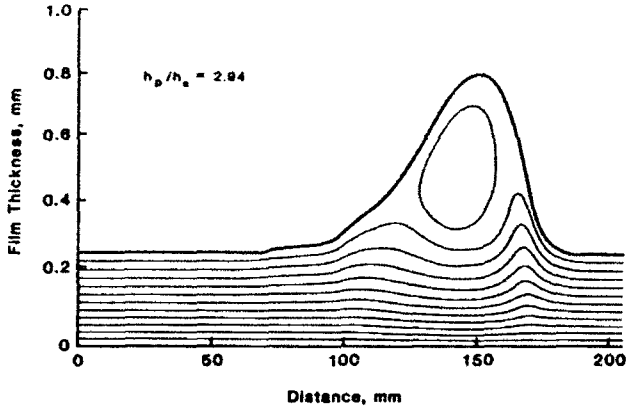

Figure 8. Streamline map for representative isolated wave.

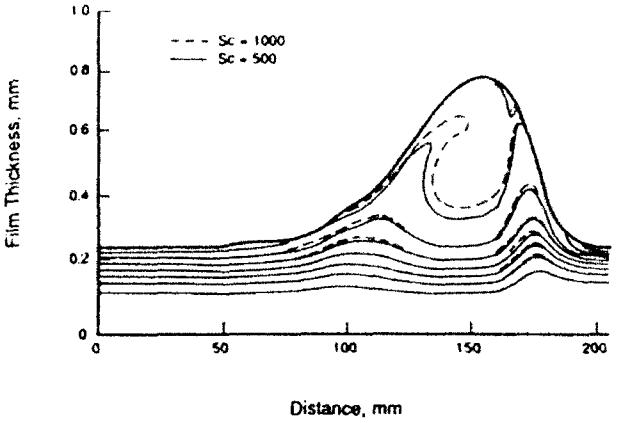

Figure 10. Concentration profiles in isolated wave 4,500 mean film thicknesses below feed for Schmidt nos. 500 and 1,000.

A profile of the local mass flux (for a saturated concentration of 1 kg/m^3) for the isolated wave is presented in Figure 11 for a Schmidt number of 500. The absence of normal velocities near the interface greatly affects the local flux near the front and rear stagnation points, where the local fluxes approach those expected for a purely diffusive situation. In contrast, near the front and behind the peak of the wave, convection increase the local flux by several times over the diffusive limit. Comparison of Figures 10 and 11 shows that the maxima in local flux values correspond to regions in which the wave peak interacts with the slowly moving substrate. This hydrodynamic process is also responsible for the dramatic increase in wall shear stress over that for parallel flow. Concentration and local flux profiles for the average wave were similar to those computed for the isolated wave. Previous models that suggest surface renewal as a result of large waves interacting with the substrate are now seen as clearly inconsistent with the computed concentration profiles.

Figure 12 shows the concentration profile in an interacting wave for a Schmidt number of 500 appearing 4,500 mean film thicknesses below the feed. The local flux profile for this interacting wave is shown in Figure 13. The profile appears to approximate the sum of the profiles obtained from isolated waves. The extra stagnation points create additional extrema in the profile, with the minimum occurring in the trough between the waves as a result of the stagnation region separating the two counterrotating recirculation zones. The presence of the stagnant zone separating the peaks dampens the effect of the interacting waves on mass transport. Compared to the SCTT prediction, enhancements are close to those associated with isolated waves.

The integral of the local flux along the wave was normalized by that expected for SCTT as given in Eq. 13. The predicted mass transfer to an isolated wave was then computed by weighting the flux through the wavy interface and the rippled substrate. Since the substrate was covered with capillary waves it was modeled using an enhancement of 30% as given by the model of Ruckenstein and Berbente (1968). The enhancement for the wave and its associated substrate was then computed from:

$$\frac{\text{Total flux}}{\text{SCTT prediction}} = \left(\frac{t_f + t_b}{t_f + t_b + t_s}\right)\frac{\text{Flux due to wave}}{\text{SCTT prediction}} + \left(\frac{t_s}{t_f + t_b + t_s}\right)(1.30) \quad (19)$$

Enhancement factors computed for the seven waves whose profiles were measured are presented in Figure 14 for several

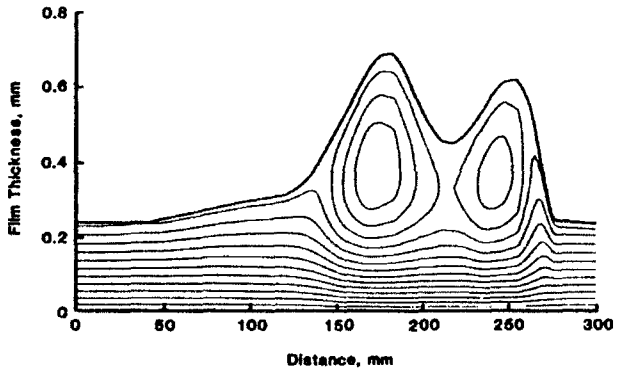

Figure 9. Streamline map for representative interacting wave.

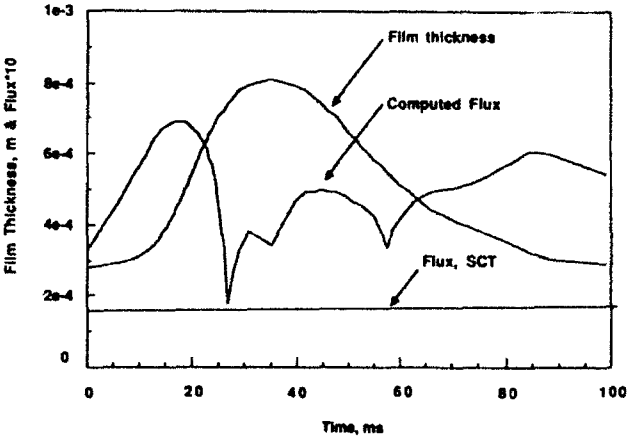

Figure 11. Local mass flux values for isolated wave for conditions of Figure 10 and $Sc = 500$.

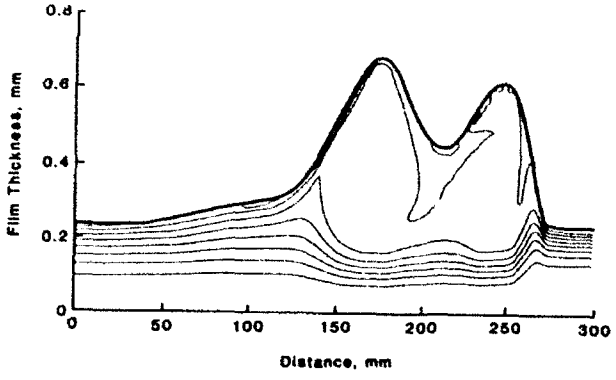

Figure 12. Concentration profiles in interacting wave 4,500 mean film thicknesses below feed for $Sc = 500$.

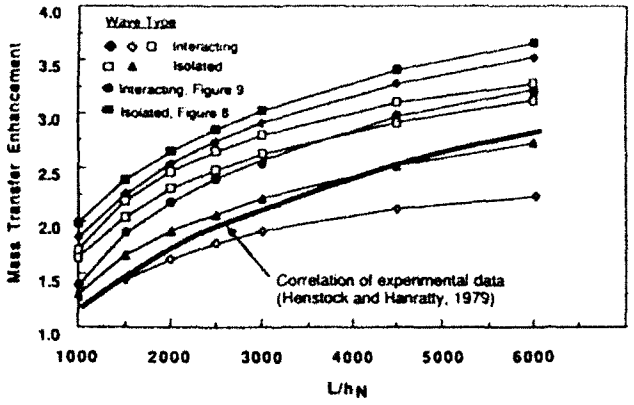

Figure 14. Computed and observed mass transfer enhancement for transfer through wavy interface at $Sc = 500$.

locations below the entry. It should be recognized that the wave profile and velocity vary along the length of the film (Zabaras and Dukler, 1988) while for these computations the profile measured at $L/h_N = 8{,}550$ (3.1 m) was used for the mass transfer computation at all locations. The numerical analysis predicts mass transfer rates 1.7–3.5 times greater than the short contact time predictions. A comparison with experimental data as correlated by Henstock and Hanratty (1979) is included in this figure. The experiments represent mass transfer rates averaged from L/h_N of zero to the indicated value while the computation describes the local rate as the wave passes a particular L/h_N. Similar qualitative trends in enhancement are clearly seen in both computed and measured values.

Figure 15 compares the enhancement computed for the average wave uniformly distributed across the length of the interface with the experimental enhancement given by the Henstock and Hanratty (1979) correlation. The agreement in magnitude and trend is now semiquantitative. Furthermore, the discrepancies can readily be understood. For short columns the waves are smaller and the rate of mass transfer would be less than that computed for the average film structure in the figure. At large values of L/h_N the existence of waves above this location changes the inlet condition used in the computations to one of a more uniform concentration as a result of the successive mixing induced by the upstream waves. This would lead to larger concentration gradients at the surface and consequently a higher mass transfer rate than predicted by the simulation. Inclusion of these effects would produce even closer agreement between the model and experiment. Once the ability to predict the average profile as a function of position along the film is developed these factors can readily be incorporated into the computation.

Mass transfer from the wall

Simulations of the mass transfer in the two waves discussed in the previous section will be presented. Concentration fields, average concentration values [across the film, from $y = 0$ to $y = h(x, t)$], and total mass accumulation were determined for fixed values of the active surface length and various Schmidt numbers. Mass transfer enhancement due to large waves was determined by computing the total mass within the large wave after it had passed over the active surface and comparing it to the amount of mass accumulated by a flat film of thickness h_N which had been in contact with the active surface for the same amount of time. The active surface length for the present results was 800 average film thicknesses, or roughly 0.29 m for a Reynolds number of 880. This value represents about one

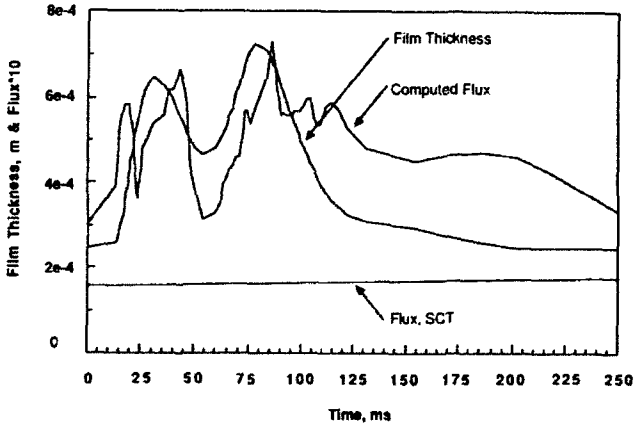

Figure 13. Local mass flux values for interacting wave for conditions of Figure 12.

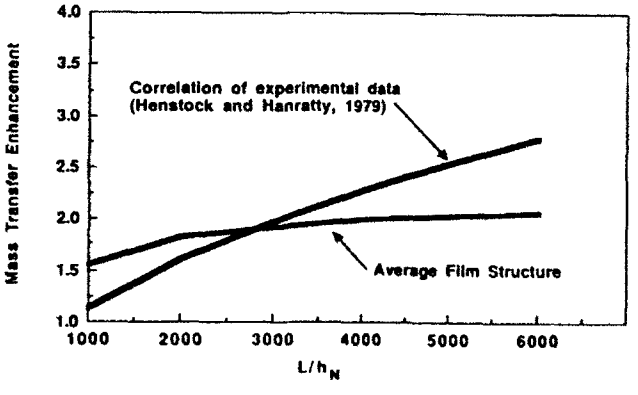

Figure 15. Mass transfer enhancement computed for average film structure compared to observed values for $Sc = 500$.

wavelength. Results for Schmidt numbers of 200 and 1,200 are presented. Fluid physical properties were taken as identical to those used for the hydrodynamic simulation, leading to Peclet numbers ranging from 1.76×10^5 to 1.056×10^6.

Average concentration profiles (normalized by the saturated wall concentration) for the isolated large wave are presented in Figure 16. The increase in average concentration ahead of the peak is due to the strong normal velocities at the wall in this region, which result from the rapid change in wall shear stress. The average concentration profiles appear to be affected most by the strong hydrodynamic interactions between the wave peak and body with the surrounding flat film. Other hydrodynamic processes caused by the wavy interface apparently do not penetrate to a level sufficient to alter the transport processes at the wall.

Further evidence of the strong normal velocities near the wall is found in the profiles of near wall concentrations, Figure 16b. The near wall concentrations are those that are found in the first cell inside the boundary and are proportional to the concentration gradient at the wall. These values are significantly lower directly under the steepest part of the wave front, which corresponds to the region in which the shear stress is a maximum. Average and near wall concentrations are closest in magnitude near the front and under the peak of the wave. In contrast, the surrounding regions of substrate are characterized by near wall and average concentrations that differ by as much as a factor of ten.

Increasing the Schmidt number reduces mass diffusivity, increasing the resistance to mass transport into the waves. However, the presence of significant normal velocities near the wall reduces this effect. For large Peclet numbers, increasing the Schmidt number sixfold (from 200 to 1,200) would be expected to decrease the average concentration by the same factor if no normal velocities were present. However, Figure 16a shows that the average concentration is reduced by no more than three when the hydrodynamic effects are included. In a flat film, the near wall concentrations would be expected to scale inversely with Schmidt number, as the flux is directly proportional to the diffusivity. Figure 16b shows that the near wall concentration decreases by no more than one-half when the Schmidt number is increased sixfold, further illustrating the extent to which normal velocities alter the mass transfer resistance.

Flow within the interacting wave produces the concentration profiles shown in Figure 17. The presence of two interacting but separate closed recirculation regions within the peaks significantly increases mass transfer through the wavy surface and apparently has the same effect on transport from the wall. Pronounced changes in the average concentration accompany increasing mass diffusivity in the interacting wave. While the near wall concentration variation is magnified by low diffusivity, the variation in average values suggests that once the mass is transported into the peak regions, diffusion becomes important, as the average concentration profile associated with a lower diffusivity is smoother than expected.

Mass transfer enhancements for three interacting waves, the isolated wave, and the average film are presented in Figure 18. Experimentally determined enhancements from Stirba and

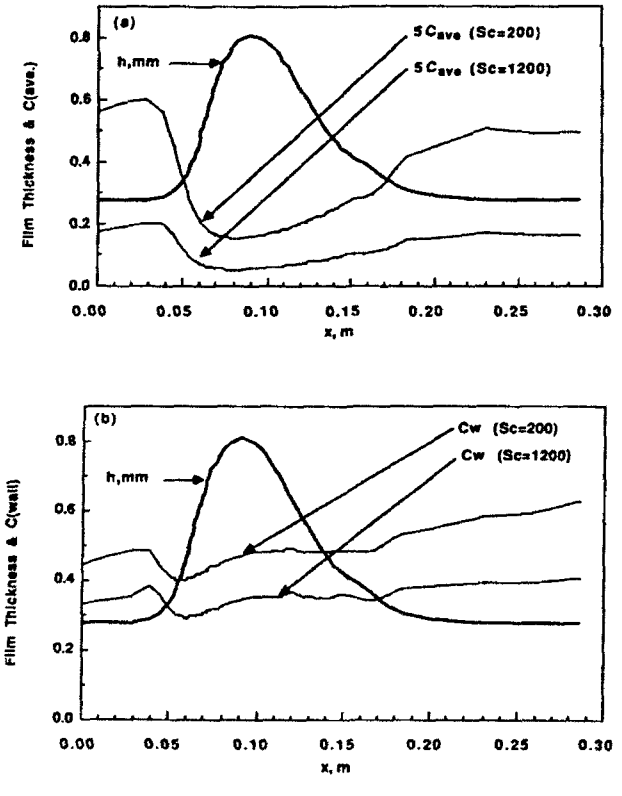

Figure 16. Variation of concentration with film thickness and Schmidt number for isolated wave.

(a) Average concentration
(b) Rear wall concentration.

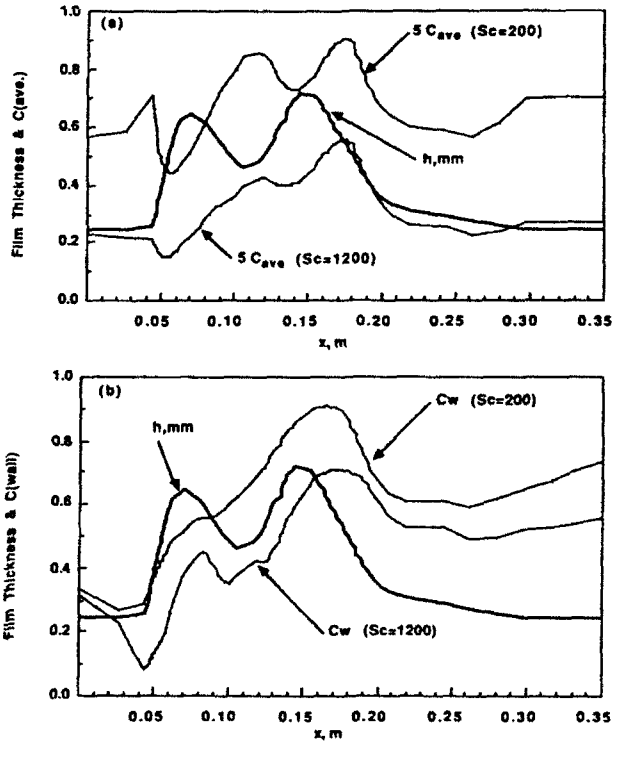

Figure 17. Variation of concentration with film thickness and Schmidt number for interacting wave.

(a) Average concentration
(b) Near wall concentration.

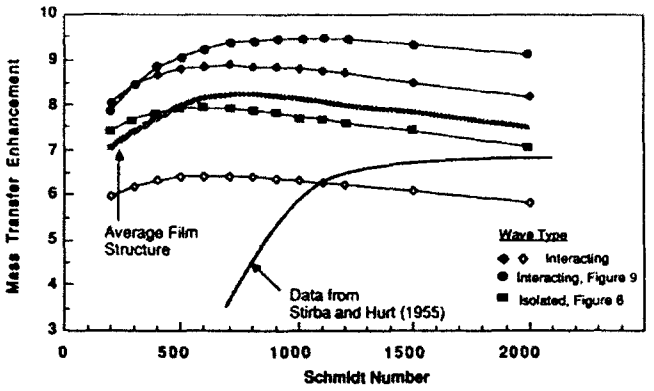

Figure 18. Computed and observed mass transfer enhancement for transfer from wall for *Re* = 880.

Hurt (1955) at Reynolds numbers between 850 and 900 are included for comparison. Values for the average film fall between the large waves and agree reasonablly well with the data at higher Schmidt numbers. At lower Schmidt numbers, the simulations appear to overpredict the enhancement. The discrepancy results from two experimental limitations. Stirba and Hurt report difficulties in fully wetting the surface of the benzoic acid with water (Schmidt number 609), which would decrease the accumulation by the wavy film. For alcohol–organic acid systems (Schmidt numbers > 800) no wettability problems were encountered and the comparison is correspondingly more favorable.

In the limit of very small Schmidt numbers, the enhancement due to the complex hydrodynamics vanishes, but for Schmidt numbers as low as 200 this enhancement may still be as large as 500%. As the Schmidt number increases above roughly 1,200 the enhancement associated with large waves begins to decrease due to the inability of the fluid to diffuse into the regions of the flow in which normal (v) velocities exist. It is expected that for Schmidt numbers of industrial interest, normally less than 5,000, the enhancement due to large wave hydrodynamics will be at least 500%.

Conclusions

The interface of a falling liquid film is covered with a random array of small and large waves interacting in a complicated manner, including many with peak thicknesses several times the mean. Neglecting the influence of the large waves causes most models to seriously underpredict experimentally observed transfer rates. Numerical simulations of the hydrodynamics within large waves presented previously (Wasden and Dukler 1989a, b) exposed mechanisms through which transport would be augmented. Hydrodynamic data obtained from this procedure were used in the simulation of passive transport in these large waves. The importance of the complex hydrodynamics within the waves has been demonstrated by the semiquantitative agreement between computed and measured transfer rates at both interfaces. Future modeling of transport processes in wavy films must include provisions for predicting the significant normal velocities at each interface and relating them to the interfacial structure.

The random interface has been approximated by an interface composed of periodically occurring, statistically average waves interspersed among smaller ripples. Mass transfer rates computed for such an array are 1.5 to 2.5 times greater than that predicted for gas absorption into nonwavy films and four to seven times greater than the flat film prediction for a dissolving wall. These enhancements are in reasonable agreement with experimental observations.

Acknowledgment

Financial support of this research by the Office of Naval Research is gratefully acknowledged. F. K. Wasden was supported by a National Science Foundation Graduate Fellowship.

Notation

c = local contaminant concentration, kg/m^3
D = gas–liquid or liquid–liquid diffusion coefficient, m^2/s
E = mass transfer rate enhancement, Eq. 6
f = average wave frequency, Hz
g = acceleration of gravity, m/s^2
h = local film thickness, mm
h_s = substrate thickness of average wave, mm
h_p = peak thickness of average wave, mm
h_N = time average, or Nusselt film thickness, mm
k_L = liquid-side mass transfer coefficient, m/s
L = length over which gas contacts a falling film, m
L_A = length of contaminated portion of wall, m
n = coordinate normal to wavy interface, m
N_{SCTT} = mass transfer rate predicted by short contact time theory, kg/m · s
Pe = Peclet number, $Re \cdot Sc$
Q = liquid film flow rate per unit perimeter, $U_N h_N$, m^2/s
Re = film Reynolds number, $4Q/\nu$
Sc = Schmidt number, ν/D
t_b = duration of average wave back, ms
t_f = duration of average wave front, ms
t_s = duration of substrate separating average waves, ms
u = local streamwise velocity, m/s
U_N = time average, or Nusselt film velocity, m/s
v = local velocity normal to boundary, m/s
V_w = wave velocity, m/s
x = axial coordinate in lab frame, m
y = coordinate normal to boundary, m
z = axial coordinate fixed on wave, m

Greek letters

ρ = liquid density, kg/m^3
ν = liquid kinematic viscosity, m^2/s
μ = liquid absolute viscosity, kg/m s
τ_w = wall shear stress, N/m^2
λ = length of sloped sections of large wave, m

Literature Cited

Acrivos, A., "Solution of the Laminar Boundary Layer Energy Equation at High Prandtl Numbers," *Phys. Fluids*, **3**, 657 (1960).
Bach, P., and J. Villadsen, "Simulation of the Vertical Flow of a Thin, Wavy Film Using a Finite-element Method," *Int. J. Heat Mass Transfer*, **27**, 815 (1984).
Back, D. D., and M. J. McCready, "Theoretical Study of Interfacial Transport in Gas–Liquid Flows," *AIChE J.*, **34**, 1789 (1988).
Banerjee, S., E. Rhodes, and D. S. Scott, "Mass Transfer to Falling Wavy Liquid Films at Low Reynolds Numbers," *Chem. Eng. Sci.*, **22**, 43 (1967).
Barrdahl, R. A. G., "Mass Transfer in Falling Films: Influence of Finite-amplitude Waves," *AIChE J.*, **34**, 493 (1988).
Benjamin, T. B., "Wave Formation in Laminar Flow Down an Inclined Plane," *J. Fluid Mech.*, **2**, 554 (1957).
Brumfield, L. K., R. N. Houze, and T. G. Theofanous, "Turbulent Mass Transfer at Free, Gas–Liquid Interfaces, with Applications to Film Flows," *Int. J. Heat Mass Transfer*, **18**, 1077 (1975).
Davies, J. T., *Turbulence Phenomena*, Academic Press, London (1972).

Dukler, A. E., "The Role of Waves in Two-phase Flow: Some New Understanding," *Chem. Eng. Educ.*, 1976 Award Lecture, 108 (1977).
Emmert, R. E., and R. L. Pigford, "A Study of Gas Absorption in Falling Liquid Films," *Chem. Eng. Prog.*, **50**, 87 (1954).
Goren, S. L., and R. V. S. Mani, "Mass Transfer through Horizontal Liquid Films in Wavy Motion," *AIChE J.*, **14**, 57 (1968).
Gosman, A. D., and F. J. K. Ideriah, *Teach-T: A General Computer Program for Two-dimensional, Turbulent, Recirculating Flows*, Dept. Mech. Eng., Imperial College, London (1976).
Hanratty, T. J., and J. A. Campbell. "Measurement of Wall Shear Stress," *Fluid Mechanics Measurement*, R. J. Goldstein, ed., Hemisphere (1983).
Henstock, W. H., and T. J. Hanratty, "Gas Absorption by a Liquid Layer Flowing on the Wall of a Pipe," *AIChE J.*, **25**, 122 (1979).
Howard, D. W., and E. N. Lightfoot, "Mass Transfer to Falling Films. 1: Application of the Surface-stretch Model to Uniform Wave Motion," *AIChE J.*, **14**, 458 (1968).
Javdani, K., "Mass Transfer in Wavy Liquid Films," *Chem. Eng. Sci.*, **29**, 61 (1974).
Kafesjian, R., C. A. Plank, and E. R. Gerhard, "Liquid Flow and Gas-phase Mass Transfer in Wetted-wall Towers," *AIChE J.*, **7**, 463 (1961).
Kapitza, P. L., and S. P. Kapitza, "Wave Flow in Thin Layers of a Viscous Fluid," *Zh. Exper. i Teor Fiz.*, **19**, 105 (1949), also in *Collected Papers of P. L. Kapitza*, II, Macmillan, New York (1964).
Leonard B. P., "A Stable and Accurate Convective Modeling Procedure Based on Quadratic Upstream Interpolation," *Comp. Meth. Appl. Mech. Eng.*, **12**, 59 (1979).
Levich, V. G., *Physicochemical Hydrodynamics*, Prentice-Hall, New York, (1962).
McCready, M. J., and T. J. Hanratty, "Effect of Air Shear on Gas Absorption by a Liquid Film," *AIChE J.*, **31**, 2066 (1985).
McCready, M. J., E. Vassiliadou, and T. J. Hanratty, "Computer-simulation of Turbulent Mass Transfer at a Mobile Interface," *AIChE J.*, **32**, 1108 (1986).
Nakaya, C., "Waves on a Viscous Fluid Film Down a Vertical Wall," *Phys. Fluids*, **A1**, 1143 (1989).
Oliver, D. R., and T. E. Atherinos, "Mass Transfer to Liquid Films on an Inclined Plane," *Chem. Eng. Sci.*, **23**, 525 (1968).
Pantakar, S. V., *Numerical Heat Transfer and Fluid Flow*, Hemisphere, Washington, DC (1980).
Pigford, R. L., Ph.D. Thesis, Univ. Illinois (1941).
Portalski, S., and A. J. Clegg, "Interfacial Area Increase in Rippled Film Flow in Wetted Wall Columns," *Chem. Eng. Sci.*, **26**, 773 (1971).
Ruckenstein, E., and C. P. Berbente, "Mass Transfer in Wave Flow," *Chem. Eng. Sci.*, **20**, 795 (1965).
———, "Mass Transfer to Falling Liquid Films at Low Reynolds Numbers," *Int. J. Heat Mass Transfer*, **11**, 743 (1968).
Seban, R. A., and A. Faghri, "Wave Effects on the Transport to Falling Laminar Liquid Films," *J. Heat Transfer*, **100**, 143 (1978).
Spence, D. A., and G. L. Brown, "Heat Transfer to a Quadratic Shear Profile," *J. Fluid Mech.*, **33**, 753 (1968).
Stirba, C., and D. M. Hurt, "Turbulence in Falling Liquid Films," *AIChE J.*, **1**, 178 (1955).
Suzuki, K., Y. Hagiwara, and T. Sato, "Heat Transfer and Flow Characteristics of Two-phase Two-component Annular Flow," *Int. J. Heat Mass Transfer*, **26**, 597 (1983).
Telles, A. S., and A. E. Dukler, "Statistical Characteristics of Thin, Vertical, Wavy, Liquid Films," *Ind. Eng. Chem. Fundam.*, **9**, 412 (1970).
Wasden, F. K., "Studies of Mass and Momentum Transfer in Free Falling Wavy Films," *Ph.D. Diss.*, Univ. Houston (1989).
Wasden, F. K., and A. E. Dukler, "Insights into the Hydrodynamics of Free Falling Wavy Films," *AIChE J.*, **35**, 187 (1989a).
———, "Numerical Investigation of Large Wave Interactions on Free Falling Films," *Int. J. Multiph. Flow*, **15**, 357 (1989b).
Zabaras, G. J., and A. E. Dukler, "Countercurrent Gas–Liquid Annular Flow, Including the Flooding State," *AIChE J.*, **34**, 389 (1988).

Manuscript received Nov. 30, 1989, and revision received July 6, 1990.

Reprinted from AICHE JOURNAL, February 1989

Insights into the Hydrodynamics of Free Falling Wavy Films

Three isolated waves of differing amplitude and shape were selected from experimental measurements of a falling liquid film at $Re = 880$ for study using an algorithm developed for solution of the Navier-Stokes equations. The method computes the velocity and pressure fields as well as the velocity of the wave. The results show that large streamwise accelerations exist along with regions of recirculating flow in a moving coordinate system. These features can explain the enhanced rates of heat and mass transfer observed in wavy film flow. Computed wave velocities and wall shear stress were in reasonably good agreement with measurements. Wave velocity is shown to be sensitive to small variations in the wave shape and explains the apparent random variation of wave velocity with amplitude that has been observed experimentally. This numerical experiment points to the shortcomings of the many methods used to model large waves on falling films that have been based on parabolic velocity profiles.

Frederic K. Wasden, A.E. Dukler
Department of Chemical Engineering
University of Houston
Houston, TX 77004

Introduction

Thin liquid films falling under the influence of gravity along solid surfaces are encountered in a wide variety of industrial process equipment, including wetted-wall absorbers, falling-film chemical reactors, condensers, and vertical tube evaporators. Reliable design of these processes depends on the ability to accurately predict the transport rates of heat and mass to the flowing film. At flow-rates of industrial interest, falling films (even in the absence of gas flow) evolve to a highly irregular wavy interface. Figure 1 displays a short time trace of such a falling film. The surface is covered by a complex array of large and small waves moving over a substrate that is less than the mean film thickness. The large waves, which range in amplitude from two to five times the substrate thickness, carry a large fraction of the total mass flowing, and are speculated to control the rate of transport (Dukler, 1977). Before the heat or mass transfer rates to such films can be modeled it will be necessary to understand the velocity distributions that exist within these waves, as well as their evolution. The present work focuses on the former question.

Making reliable experimental measurements of the velocity distribution in the films is exceedingly difficult due to the extremely small film heights (~1 mm), very short passage time of each wave (~60 ms) and the random location of the wave height, as seen in Figure 1. Nonintrusive methods such as LDA (Laser Doppler Annenometer) do not provide sufficiently fine resolution to investigate velocity profiles. Thus, experimental measurements appear limited to the time variation of wall shear stress and film thickness. As a result, analytical models have been developed in the absence of hard data on the true flow conditions that appear to exist in the waves.

Most analytical models extend the concepts advanced by Kapitza (1964) based on the use of a parabolic velocity profile and assuming that the streamwise hydrodynamic variables scale with the wavelength. In examining various models developed to that date, Dukler (1972) concluded that all failed to accurately represent any measured characteristics of the wave except at Reynolds numbers well below those of industrial interest.

Maron et al. (1985) treated isolated waves as a series of segments, each having a different type of velocity distribution depending on the physics of the region. In the substrate, a parabolic velocity profile was adequate, while the flow under the front of the wave was assumed to be fully mixed. The slowly varying wave back was described with a boundary layer model. Upon matching these solutions at the segment boundaries, it was possible to predict wave mean characteristics (height, length, velocity, substrate thickness) in reasonable agreement with the values measured by Zabaras (1985). The model was fitted with a limited amount of data from experimental measurements and it failed to explain the large variation observed in individual wave amplitudes and lengths.

Modeling the wavy film flow by a direct solution of the Navier-Stokes equations is hampered by numerical stiffness imposed by the stress-free interface; as a result, convergence is difficult except at the lowest flow rates. Bach and Villadsen (1984) explored the application of a finite-element scheme to the unsteady problem of waves developing from initial perturbations

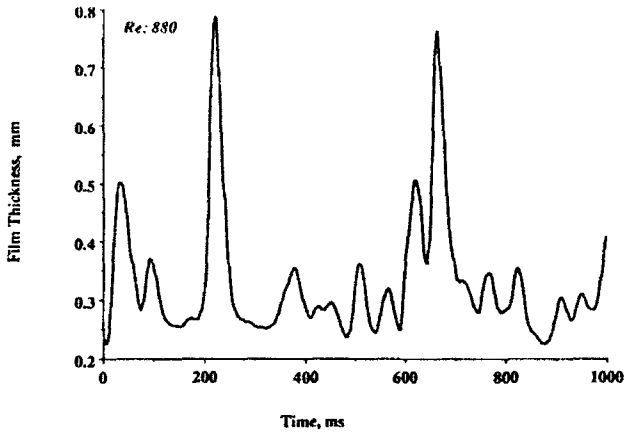

Figure 1. Film thickness time trace.

on the smooth film for Reynolds numbers up to 100. Their work predicted that the equilibrium condition would consist of waves having one general shape, a condition contrary to experimental fact even at film Reynolds numbers as low as 1. The film Reynolds number is defined as $Re = 4\,Q/\nu$, where Q is the mass flow rate per unit perimeter, and ν is the kinematic fluid viscosity. Kheshgi and Scriven (1987) applied a finite-element technique to a problem with periodic boundary conditions in the flow direction, and verified the evolution of infinitesimal disturbances as predicted by Orr-Sommerfeld analyses. Their work was limited to low flow rates, and failed to generate waveforms comparable to those observed experimentally for fully developed flow.

In the absence of analytical models for velocity profiles that appear to represent reality, and due to the absence of suitable experimental methods for measuring these profiles, a series of numerical experiments were undertaken. Wave shapes, wall shear stress profiles, and wave velocities were measured in our laboratory for a film Reynolds number of 880, chosen to insure significant inertial forces while remaining viscous in nature. A novel method of solving free surface flows was developed, using experimentally determined film thickness data for large, isolated waves to solve for the position of the free interface. The results of these computations demonstrate the complex dependence of velocity distributions on wave shape, and represent an early step toward realistic modeling of large waves.

Experimental Procedure

Flow loop

For fully developed wavy film flow, film thickness and wall shear stress data were collected in a 50.8 mm ID vertical test section in a flow loop described by Zabaras et al. (1986). After being pumped through a calibrated rotameter, the aqueous solution entered the column through an annulus whose inner wall consists of a stainless steel porous sinter having 100 μm pore size. Combined with careful leveling of the column prior to data collection, this entry section insured minimal deviations from axisymmetric flow and produced a smooth inlet flow. The measuring station was located 3.1 m below this entry section.

Measuring station and measurement techniques

The measuring station, shown in Figure 2, is patterned after that described by Zabaras et al. The removable section allows

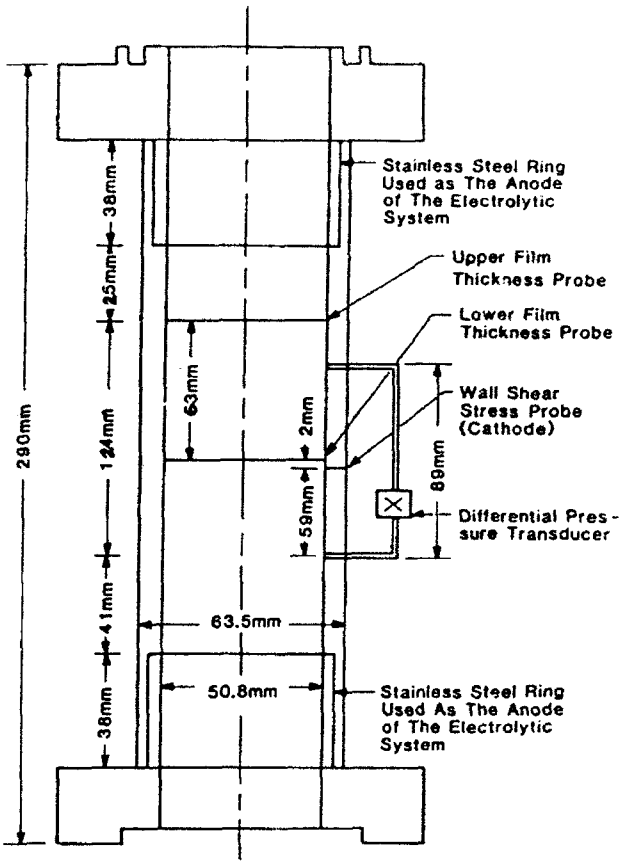

Figure 2. Measuring station.

simultaneous measurement of film thickness and wall shear stress at one location and of thickness at another. The station was constructed of the same material as the flow loop, and was carefully machined to insure a smooth transition to the station.

Film thickness probes consisted of twin parallel platinum-13% rhodium wires of 0.05 mm dia., spaced 2.5 mm apart, which penetrated the flow. As described in detail by Brown et al., (1978), a linear relation exists between the resistance of the film between the wires and the film thickness. Calibration proceeded by setting the measuring station horizontal, blocking the ends, and introducing different fluid levels, determined to within 10 μm by using a cathetometer, followed by measurement of the resulting resistance. Downstream electronics for converting this resistance to a DC voltage signal are described elsewhere (Zabaras et al., 1986). Conductance of the fluid was monitored closely at all times during the calibration and data collection procedures to insure proper correction of any thermally induced conductance drift.

Wall shear stress measurements were based on the electrochemical mass transfer method described by Hanratty and Campbell (1983). For the present series of measurements, the iodine/tri-iodide system was chosen. The working solution contained 0.1M KI and 0.004M I_2(s) in demineralized water, and was replaced every 2 h to minimize errors due to iodine evaporation. A dry nitrogen atmosphere was used in the flow loop to minimize oxygen saturation of the solution. Fluid properties at 25°C are: density, 1,010 kg/m^3; absolute viscosity, 8.50×10^{-4} kg/m · s; and surface tension, 7.12×10^{-2} N/m. The cathode

for this system consists of a flush-mounted strip of platinum foil, 0.075 mm (in the flow direction) by 1 mm wide, embedded in Plexiglas to insure electrical isolation. By measuring the current produced by an electrochemical reaction at the surface of the cathode, the wall shear stress at that location is determined. For the redox reaction

$$I_3^- + 2e \rightarrow 3I^- \qquad \text{(cathode)}$$
$$3I^- \rightarrow I_3^- + 2e \qquad \text{(anode)}$$

a concentration boundary layer develops on the cathode surface, which is polarized at -0.8 VDC to insure the concentration approaches zero. For the iodine system, the range of polarization voltage is quite broad, insuring that large increases in flow rate will not deplete the electron source at the cathode. Details concerning the downstream electronics and calibration associated with this measurement technique are found elsewhere (Zabaras et al., 1986).

It is now recognized (Mao and Hanratty, 1985) that the response of the electrochemical probe is highly dependent on the nature of the "input" wall shear stress. For the ionic system employed in this study, errors in both phase and magnitude are expected to be small due to the large ($10^3\,s^{-1}$) mean velocity gradient, small cathode surface area, and large Schmidt number (ν/D) of the fluid ($\approx$780). The relationship given by Hanratty and Campbell (1982) between cathode current and wall shear stress was used in this study, as the frequencies in the data were sufficiently low to allow the use of a quasi-steady analysis.

Data collection, processing, and analysis

Voltage signals from two film thickness probes and the wall shear stress probe were first low-pass filtered at 1 kHz, then fed to a microcomputer-based analog to digital (A/D) converter. Each signal was digitized at 1 kHz by a Data Translation 12 bit A/D converter installed in a DEC Micro 11/73 microcomputer. The data set comprised 1 min of data, and was stored on the system Winchester disk prior to applying calibration curves and writing the data to magnetic tape for further analysis. Digitization and collection errors are expected to be negligible for all data, while calibration errors for the film thickness measurement are expected to be less than 3%. Errors inherent in applying steady state wall shear stress calibration curves depend on the nature of the input signal, requiring separate examination of individual results. Zabaras (1985) reports estimated errors of less than 7% for this technique.

Film thickness and wall shear stress data was examined to locate isolated waves, defined by a wave having a peak to substrate thickness ratio greater than 2, and surrounded by at least one wavelength of reasonably flat film. For the sequences of raw data, three representative waves of various dimensions were chosen for computational domains. For each case, a nominal wave velocity was determined from the time necessary for the wave to travel from the upper to lower film thickness probes.

Numerical Method

Solution of free-boundary problems requires methods for both the solution of the governing momentum equations and shape determination. The velocity and pressure fields within the wave were determined by solving the Navier-Stokes equations in primitive variable form. For a film Reynolds number of 880, the wave thickness generally was less than 1% of the pipe radius, and therefore a two-dimensional Cartesian coordinate system was chosen. The transformation of time traces of film thickness to this coordinate system comprised the shape determination portion of the overall algorithm. The common method of computing the position of a free interface, $h(x)$, is to determine the value of the film thickness, h, at given values of the streamwise variable, x. The present method inverts the process: for given, measured values of h, we find the values of x that result in $h(x)$ satisfying all of the free interface boundary conditions. To insure accurate representation of the interfacial pressure, a fourth-order-accurate, divided-differences scheme was used to compute the curvature of the interface:

$$h_{xx}/(1 + h_x^2)^{3/2} \qquad (1)$$

Initially, the waves were modeled as though their shape remained constant with time; these waves are termed "solitary." The new streamwise coordinate, z, is fixed on the wave, and originated at the front of the wave. The film thickness profile in the time domain, $h(t_i)$, was converted to the length domain, $h(z_i)$, through the transformation

$$z_i = z_o + V_w(t_i - t_o) \qquad (2)$$

for i ranging from 1 to the number of film thickness points in the isolated wave. In this manner, the wave profile was "stretched" for use as a computational domain, and time was removed from the problem. For this coordinate system, the wave remains fixed, and the wall moves upward at a constant speed given by V_w, the wave velocity for the solitary wave.

It is useful to define a new streamwise velocity component,

$$u(z, y) = u'(x, y) + V_w, \qquad (3)$$

where $u'(x, y)$ is the streamwise velocity in a coordinate system fixed on the wall. The governing equations for this viscous, incompressible, and isothermal flow relative to the moving wave become

$$uu_z + vu_y = -P_z/\rho + \nu\Delta u + g \qquad (4)$$

$$uv_z + vv_y = -P_y/\rho + \nu\Delta v \qquad (5)$$

$$u_z + v_y = 0 \qquad (6)$$

where v is the velocity in the normal (y) direction, P is the pressure, g represents gravitational acceleration, and ν and ρ are the kinematic viscosity and density of the fluid, respectively. At the stress-free interface, $y = h(z)$, tangential and normal stress balances require

$$(u_y + v_z)(1 - h_z^2) - 2h_z(u_z - v_y) = 0 \qquad (7)$$

$$P = \sigma h_{zz}/(1 + h_z^2)^{3/2} + [2\mu/(1 + h_z^2)]\,[u_z h_z^2 - (u_y + v_z)h_z + v_y] \qquad (8)$$

where σ is the surface tension coefficient. At the wall, $y = 0$,

$$u = V_w, \qquad v = 0, \qquad (9)$$

represent the standard no slip and no flux conditions. Velocities at the interface are related through the kinematic condition in a moving frame,

$$v = uh_z, \qquad y = h(z). \tag{10}$$

The inlet velocity profile is parabolic, representing an acceleration-free falling film, while a sufficient and physically consistent outlet condition for a solitary wave requires a zero streamwise derivative for all variables. The variable V_∞ replaced $h(z)$ as the final variable to be iteratively determined in the free-surface problem, and completes a now well-posed problem.

For each wave profile, a unique, nonuniform finite-difference grid mesh was constructed. The mesh for a typical domain is shown in Figure 3. The particular wave shape determined the grid spacing used. Mesh refinement continued until no further change in either the computed wave velocity or wall shear stress profile was observed. Of particular importance was the concentration of cells near the front and top of the wave, since the velocity fields change drastically in this region due to the large interfacial slope and curvature. For most waves, 1,200 cells of dimension $\delta x \delta y$ were sufficient, and produced grid Reynolds numbers [$Re_{G_x} = u(z, y)\,\delta x/\nu$, $Re_{G_y} = v(z, y)\,\delta y/\nu$] of order 1 in the y direction, and ranging from 1 to 100 in the streamwise direction.

The curved interface was accommodated by allowing boundary cells to be cut by the boundary, $h(z)$, thus reducing their volume. This situation is illustrated in Figure 4. This technique produced areas adjoining two boundary cells, the centers of which were outside the computational domain. As the stress-free interface requires a zero normal derivative of the velocity vector with respect to the boundary, $h(z)$, these regions were treated as inviscid channels through which all fluid leaving one boundary cell on its shared side passed into the neighboring cell through its respective shared side. The total area of these regions represents less than 0.1% of the total domain, and had little effect on the results.

The equation set was solved on a finite-difference grid using a variant of the TEACH-T code (Gosman et al., 1969), incorporating the SIMPLER pressure-continuity solution procedure; the principles of this method are described in detail elsewhere (Patankar, 1980). The domain includes regions of significant streamwise variation in all variables, thus necessitating an accurate method of discretizing convective momentum terms. The simplest method of convective discretization, upwind differencing insures a reasonably stable numerical solution, but introduces numerical diffusion in regions of the flow where streamlines are oblique with respect to the grid lines (Raithby, 1976). More importantly, the upwide scheme lacks sensitivity to cross-stream diffusion and source terms (Leonard, 1979), which are of tremendous importance in the case of a thin film. This lack of sensitivity diminishes the effects of the y direction diffusion as well as the v velocity in the solution of the streamwise velocity. These deficiencies in the upwind and hybrid methods require the use of a QUICK-based scheme, which improves accuracy by expanding the number of neighboring points included in interpolated values of velocity.

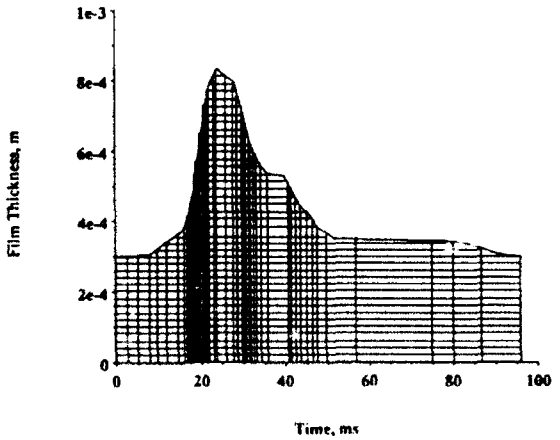

Figure 3. Sample finite-difference grid.

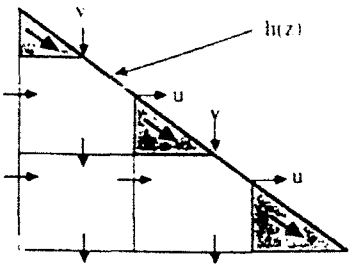

Figure 4. Interface finite-difference grid.

Based on Leonard's (1979) third-order-accurate discretization scheme QUICK, Pollard and Siu (1982) developed the QUICK-ER (Extended and Revised) method of discretizing convective terms. The QUICK-ER method overcomes stability problems inherent in the QUICK procedure at the expense of slower convergence, and is considered the most satisfactory method of handling convective momentum terms (Huang et al., 1985). For application to nonuniform grids, a new version of QUICK-ER was developed. This method follows the spirit of the QUICK-ER formulation, but includes locally variable weighting factors to account for the nonuniformity of the grid in both directions. Although QUICK-ER schemes requires more computational effort per iteration than upwinding, particularly for nonuniform grids, improvements in accuracy allow the use of a slightly coarser grid, so total computational time exceeds that required by the upwind method by only 20%.

The solution procedure began with choosing a value for V_∞ and creating the transformed domain, given by Eq. 2. The u velocity field was set to a parabolic profile everywhere, and the v velocity field was set to zero. The pressure at each z location was set to the surface pressure due to curvature. Updated velocity and pressure fields within the wave were then computed using Eqs. 4, 5, and 6. Through interpolation for the velocity gradients in the interfacial shear stress balance, Eq. 7, streamwise and normal velocities in the interior of the flow field were used to derive an expression for the streamwise surface velocity. Coupled with the kinematic condition, Eq. 10, the velocities on the surface were known for each iteration. The surface pressure computed from Eq. 8 was used to determine the first pressure value in the interior of the domain through the use of parabolic interpolation using the surface pressure and two interior pressures. With the newly computed surface variables, the velocity and pressure fields were updated until the sum of residuals of mass and momentum (normalized by the inlet quantities) over the domain was less than 10^{-3}. This condition also required the

interfacial shear and normal stress balances to be within 10^{-2} Pa of zero, and thus, the governing equations and boundary conditions were satisfied.

Upon convergence of the velocity and pressure fields, the average pressure in the flat outlet section was examined. If the average pressure did not approach zero, as required for a nonaccelerating film surrounding a solitary wave, a new value of V_w was chosen and the process repeated. The adjustment procedure for V_w was simple: If the pressure in the outlet section was higher than zero, the wave (wall) velocity was too high, since the wall was pushing excess fluid through the wave, and a positive pressure at the outlet was opposing this extra fluid in an attempt to satisfy the mass balance for the wave.

Examination of the experimental data reveals that the large waves do not remain precisely constant in shape. Incorporating this unsteady effect is accomplished through the use of a locally constant stretching parameter, as opposed to the globally constant value used for the classical solitary wave. The domain transformation for this case is given by:

$$z_i = z_o + V_{wi}(t_i - t_o) \tag{11}$$

where z is the streamwise coordinate. In general, this pseudo-wave velocity is

$$V_{wi} = V_w [1 - e(z_i)] \tag{12}$$

where $e(z_i)$ is an iteratively determined local stretching variable, and V_w represents the wave velocity associated with the substrate. The solitary wave case is recovered by setting $e(z_i) = 0$ for all i. As before, we define a new streamwise velocity component as

$$u(z, y) = u'(x, y) + V_w(z_i) \tag{13}$$

which allows the same governing equations and boundary conditions, Eq. 4–10, to apply, The transformation, Eq. 12, introduces a locally variable mass and momentum source due to the evolving nature of the wave, which does not appear in a solitary wave. The solution procedure is identical to that of the purely solitary wave. The solution procedure is identical to that of the purely solitary wave, with the exception that now a profile of V_{wi} must be specified instead of a single value. When the velocity and pressure fields have converged for a given set of V_{wi}, the wave shape is adjusted through $e(z_i)$ to meet two criteria. The baseline wave velocity, V_w, was adjusted such that the average pressure in the flat outlet section approached zero, as before. The computed wall shear stress profile was then compared to the experimental profile, and adjustments made to $e(z_i)$ to correct deviations. In this sense, the classical free-boundary problem is recovered, albeit supplemented by experimental data.

The procedure developed for the solitary waves required an average of 300 iterations of the velocity and pressure fields to converge, with an underrelaxation factor of 0.5 used for all variables. Between four and eight adjustments to the solitary wave velocity were required to produce a flow with an average outlet pressure less than 10^{-2} Pa. For the quasi-unsteady case, the same number of iterations was required to achieve convergence of the velocity and pressure fields, while the adjustment of the variable wave velocity to match wall shear stress data took anywhere from five to 20 iterations.

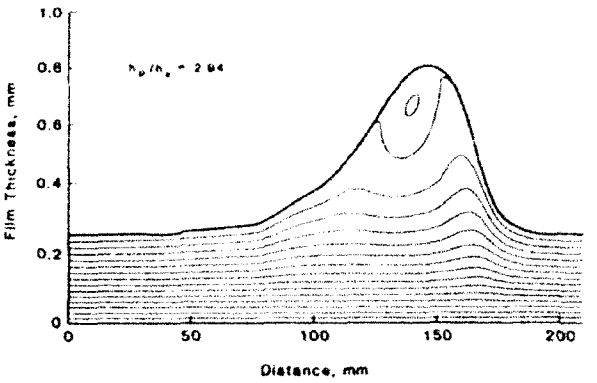

Figure 5. Solitary wave streamline map, peak/substrate ≈3.

The program was coded in FORTRAN 77, and required 2 MB of task space. Execution times for convergence of the velocity and pressure fields were approximately 5 CPU h on a VAX 11-750 computer.

Results

Initial computations explored the validity of neglecting the evolution of the wave shape. For a peak/substrate thickness ratio of approximately 3, the resulting streamline map and wall shear stress profile comparisons are shown in Figures 5 and 6. The body force due to gravity, ρgh, is presented to accommodate comparison with the wall shear stress predicted by a parabolic velocity profile. The shear stress comparison suggests that the front and back of the wave are accurately described as moving undeformed, but neglecting the evolution of the peak of the wave causes discrepancies between computed and measured wall shear stresses. Figure 7 shows superposed traces of the film thickness measured at locations 63 mm apart, and clearly illustrates the slight difference in speed between the front and back of the wave as it moves down the tube, suggesting $e(z_i) > 0$ in this front region. In order to evaluate the effect of small changes in velocity along the wave, the parameter $e(z_i)$, given by Eq. 12, was varied by trial and the effect on the resulting wall shear stress comparison noted. Figure 8 shows the very slight degree of

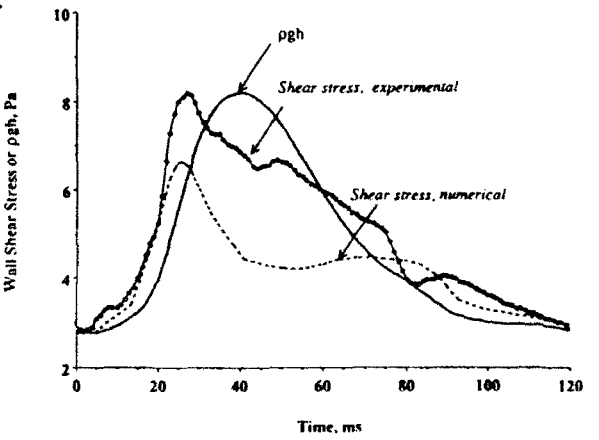

Figure 6. Solitary wave shear stress comparison, peak/substrate ≈3.

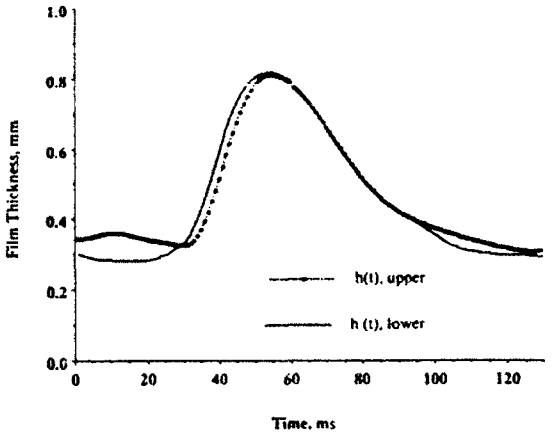

Figure 7. Evolution of nearly solitary wave, peak/substrate ≈3.

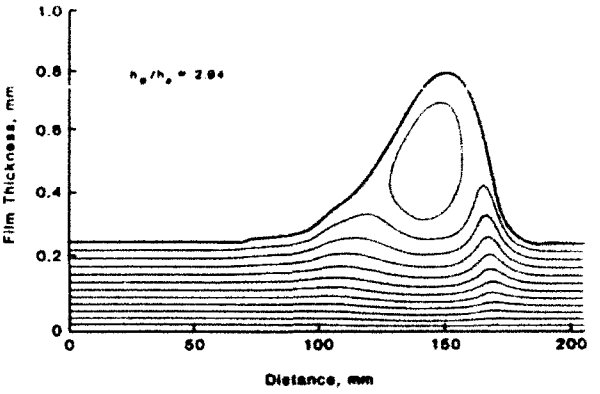

Figure 9. Streamline map for evolving wave, peak/substrate ≈3.

variation in V_w along the front of the wave, which resulted in satisfactory agreement between measured and computed wall shear stress data along the wave. To accomplish this match, the wave velocity was increased gradually over the front of the wave, reaching a maximum deviation of roughly 10% directly under the peak. The effect of this variation on the streamlines and shape of the domain is small, but still significant, as seen in comparing Figure 9 with Figure 6. While the flow near the wall appears quite sensitive to unsteady effects, global flow patterns show only small sensitivity to these changes. These results emphasize the importance of the interfacial shape in the computation of the flow field.

Streamline maps of two additional waves, having peak/substrate thicknesses of approximately 4 and 5, are presented in Figures 10 and 11. Streamlines for these larger waves were less affected by the transition from solitary to evolving waves than the smaller wave. For these larger waves, the $e(z_i)$ factors were slightly larger than in the previous wave, and the wall shear stress comparisons were similarly favorable. These streamline maps, in conjunction with Figure 9, suggest it is reasonable to view the waves as lumps of fluid overrunning a slow moving substrate. Note that for all three of these waves of different amplitude, a well-defined recirculatory region appears when viewed in a coordinate system fixed on the wave. Of importance is the presence of large normal velocities near the front and rear of the recirculating region. Previous modeling characterized all normal velocities as small corrections to the dominant streamwise flow, a supposition now seen to be inaccurate. These normal velocities can be expected to enhance transport by refreshing the surface with fluid from the substrate.

Surface velocity of the waves is nearly uniform over a large portion of the wave peak, while varying rapidly near the front. Note the presence of stagnation points in front of and behind each wave peak. While not physically important features of the flow, these points correspond to zero curvature of the streamwise velocity, and are unrealizable for a parabolic velocity profile.

Most previous modeling efforts have regarded acceleration within the wave as negligible compared to the gravitational acceleration. In the Kapitza, or long-wave, analysis, the inertial terms are neglected to produce a linear hydrodynamic problem, which yields the streamwise velocity

$$u(z, y) = (g/\nu)\,[yh(z) - y^2/2] \tag{14}$$

For this simple velocity profile, it is easily shown that the inertial forces, normalized with respect to gravity, are

$$(u\partial u/\partial z + v\partial u/\partial y)/g = (g/\nu^2)\,y^2 h(z)/2(dh/dz) \tag{15}$$

which has a maximum value at the interface, $y = h(z)$, given

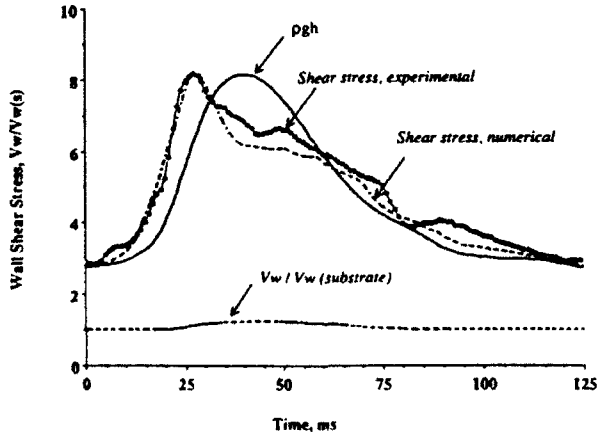

Figure 8. Shear stress comparison for evolving wave, peak/substrate ≈3.

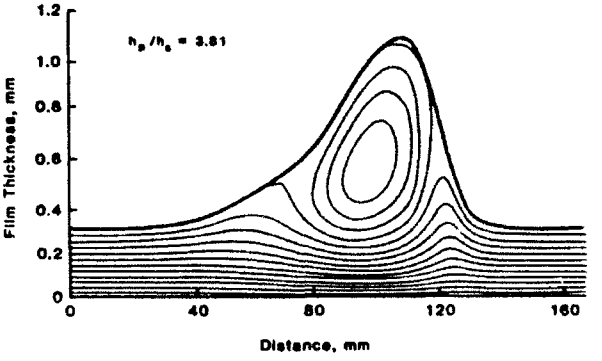

Figure 10. Streamline map for evolving wave, peak/substrate ≈4.

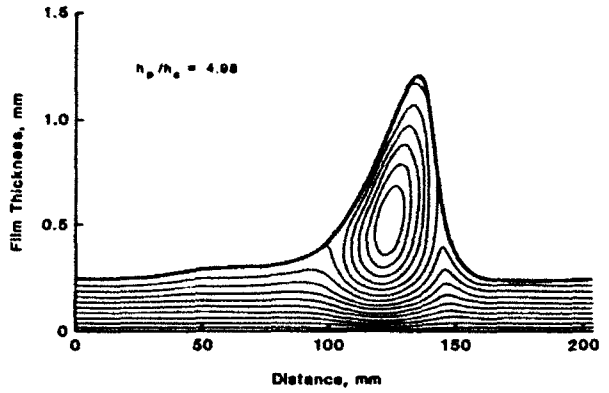

Figure 11. Streamline map for evolving wave, peak/substrate ~5.

by

$$gh(z)^3(dh/dz)/(2\nu^2) \tag{16}$$

Using the physical properties given previously, this quantity (for $Re = 880$) becomes $O(10^2)$ dh/dz. For the original linearization of the problem to be valid, Eq. 16 suggests dh/dz should be less than $O(10^{-3})$. The large waves discussed here have slopes as great as 0.07, in which case inertial forces are predicted to dominate gravity, and the original premise is violated. Further comparison of the computed inertial forces and the long wave predictions, Eqs. 15–16, must be limited to the location of extrema and existence of inertial forces when the interfacial slope is small.

As seen in the streamline maps, large accelerations exist near the surface, particularly near the front and rear of the recirculating region. For the wave having a peak/substrate thickness ratio of roughly 3 (a ratio commonly seen in experimental data), consider the three locations shown in Figure 12. Near the front of the wave, maximum normalized inertial forces (convective momentum terms/gravity), shown in Figure 13, are several times greater than gravity. Beneath the wave peak, roughly 25% of the flow is free of acceleration, a stagnant lump riding on the substrate. In this region, the interfacial slope is nearly zero, for which Eq. 16 predicts no acceleration whatsoever. However, the

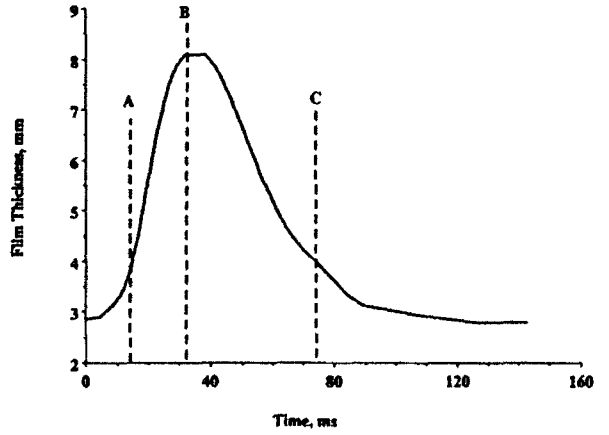

Figure 12. Location of acceleration and velocity fit examples, peak/substrate ~3.

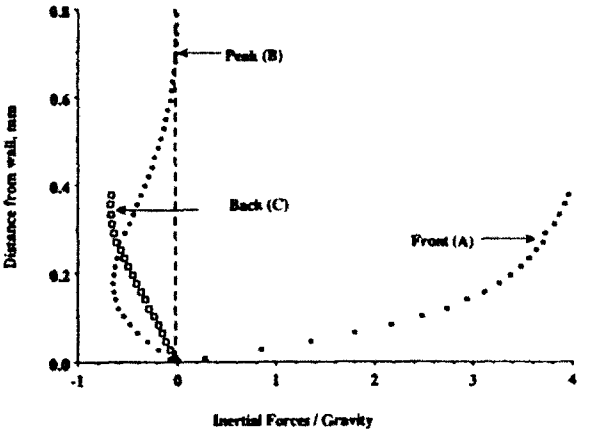

Figure 13. Convective acceleration profile, peak/substrate ~3.

substrate beneath the peak shows moderate deceleration, with the maximum occurring far from the interface, contradicting Eq. 15, which requires the maximum inertial force to exist at the free interface. Further toward the back of the wave, the acceleration is again maximum at the surface, showing a deceleration of the order of gravity, while Eq. 16 predicts a maximum acceleration of the order of 10^{-1} g for this nearly flat region. These variations in acceleration in the streamwise direction support the premise of large waves pushing material from the surface to the substrate, exchanging either heat or mass, and thereby enhancing transport properties.

Acceleration effects are further illustrated in Figure 14; a particle on a surface streamline would undergo greater changes in acceleration than one near the wall. The process of transport enhancement is again clearly shown, as particles in front of the peak accelerate toward the mass of stagnant fluid, exchanging heat or mass, and then are forced to return to the substrate.

To examine the suitability of various polynomial representations of the streamwise velocity profile, data from the numerical experiment were compared to the velocity profile predicted by Kapitza analysis,

$$u(z, y) = 2u[z, y = h(z)]\{y/h(z) - \tfrac{1}{2}[y/h(z)]^2\} \tag{17}$$

where the surface velocity was taken from the numerical experiment. In addition, the computed velocity profile was fit with a least-squares cubic polynomial in y. For illustrative purposes, consider the streamwise locations within the wave shown in Figure 12. Near the front and beneath the peak, the parabolic fits

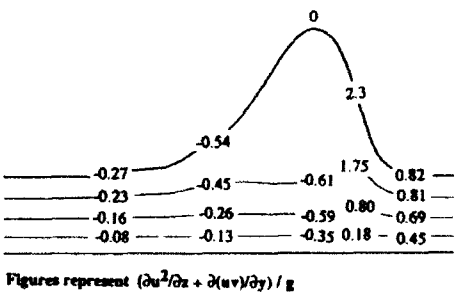

Figure 14. Fluid particle acceleration, peak/substrate ~3.

shown in Figures 15a and 15b show significant deviations from the computed velocities, while the cubic polynomial appears to faithfully represent the profile. Use of the cubic polynomial allows the curve to fit the velocity gradient at the wall as well as the surface and wall velocity accommodated by the parabolic fit. This extra degree of freedom enables a nearly perfect fit of the data, and represents the physically desirable property of matching wall shear stress as well as surface velocity. Near the back of the wave, where the shear stress suggests the flow has small acceleration forces, the cubic and parabolic fits are shown in Figure 15c to coincide more closely than at other locations.

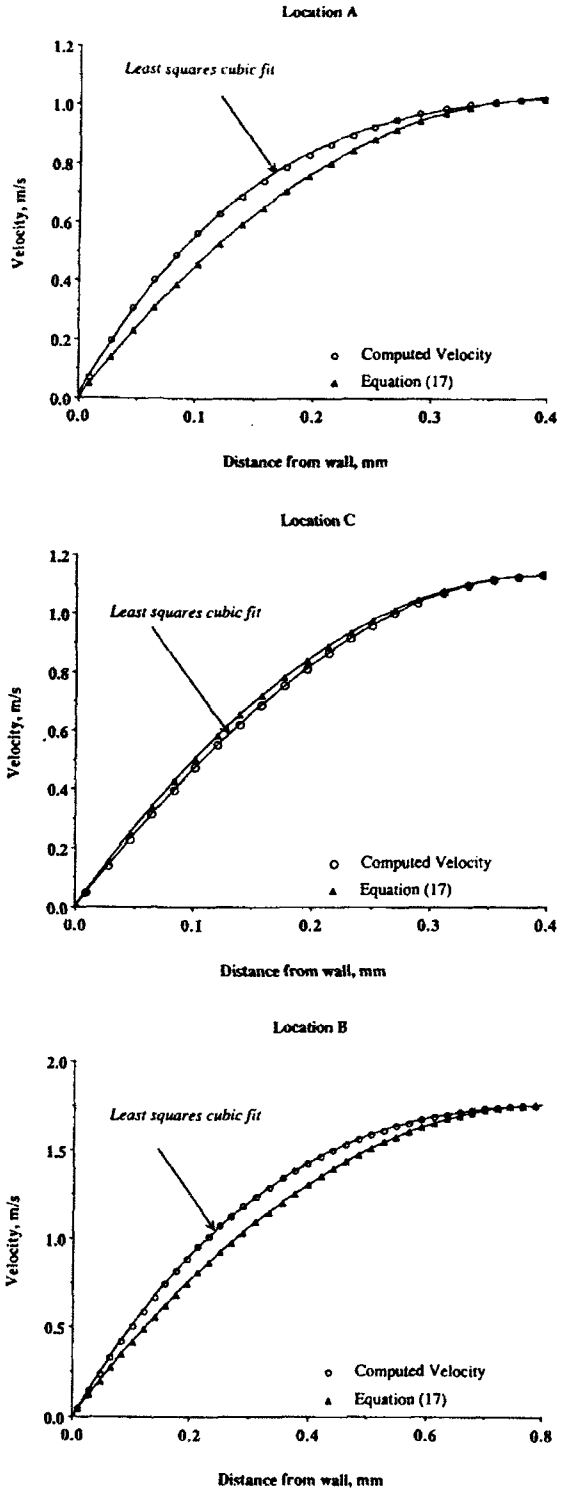

Figure 15. Curve fits of velocity profiles, peak/substrate ≈3.

In the cases of both solitary and evolving waves, the wave velocity V_w was computed by choosing V_w such that the average outlet pressure was close to zero. The dependence of average outlet pressure on the wave velocity is shown in Figure 16 for the solitary wave with a peak/substrate ratio of approximately three. This nearly linear dependence allowed quick convergence to V_w. For each wave, the substrate or base wave velocity V_w was compared to that determined by dividing the length between the upper and lower film thickness probes by the passage time of the wave peak. In cases where the wave traveled between the probes with only slight deformation, this comparison showed the computed values to be within roughly 10% of the experimental ones. For those waves evolving rapidly, this crude comparison produced less favorable results, with errors as high as 30% for the wave and peak/substrate of approximately 5.

Figure 17 shows the values of non-dimensional wave velocity determined by simulating flow in various solitary waves at different flow rates. The hydrodynamic character of these waves was similar to those presented in detail: of primary interest was the lack of correlation of wave velocity to peak/substrate thickness, in agreement with the experimental findings of Zabaras (1985).

Conclusions

The interface of a falling liquid film consists of a random array of waves of varying amplitude, length, and velocity, some isolated and some overlapping. Even at moderate Reynolds numbers, these waves display amplitudes that are two to five times the substrate thickness. Three typical isolated waves obtained from measurements of the time traces of the film thickness were selected as computational domains. A method was developed to solve the Navier-Stokes equations for this free-surface problem which yields both velocity and pressure fields in the wave and wave velocity. The measured wall shear stresses and wave velocities were in reasonable agreement with those determined from the numerical solutions. The results of these computations confirm certain earlier speculations on the me-

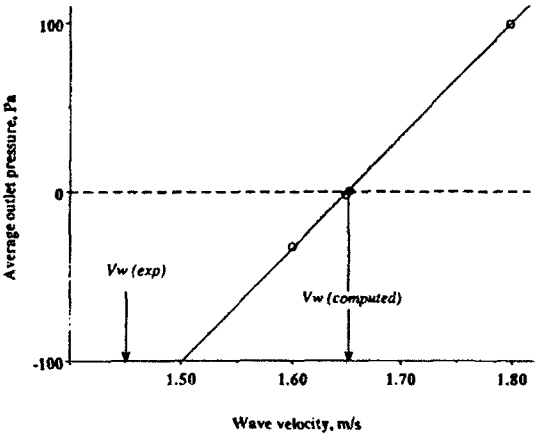

Figure 16. Average outlet pressure dependence of wave velocity, peak/substrate ≈3.

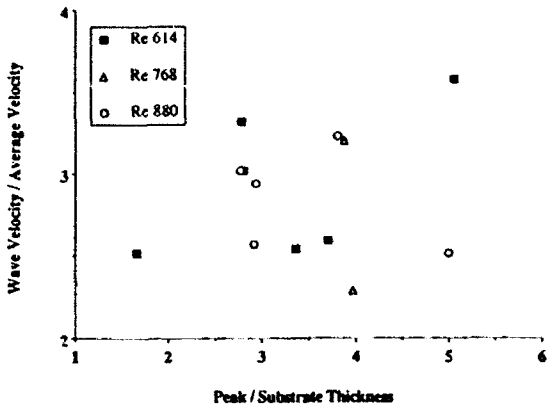

Figure 17. Numerical predictions of wave velocity.

chanics of wavy film flow and point to the inadequacies of others.

The large wave moves rapidly over a slow substrate, the bulk of the liquid being carried in the wave; this liquid is nearly stationary in a coordinate system moving with the wave. The interaction between the wave and substrate causes the acceleration of fluid at the front of the wave from the substrate in the peak. The fluid then decelerates as it passes out the wave back, generating a close recirculation region in the wave whose size depends on the wave amplitude. This process of recirculation would appear to account for the enhanced rates of heat and mass transfer known to exist in wavy films. This picture of the waves is in rough accord with the speculations of Dukler (1977).

The presence of secondary flows can be expected to enhance rates of interfacial mass transfer. Levich (1962) showed that velocities normal to wall as small as 1% of the streamwise velocity produces a 15% increase in the rate of mass transfer to the interface. As the present work shows that normal velocities may be ten times this large, we expect substantial enhancement.

Most previous studies of wavy film flows, starting with the classical work of Kapitza (1964), are based on the parabolic streamwise velocity profile, which is presumed to exist at all positions along the wave. This numerical experiment points to the inadequacy of that assumption for these large waves, and shows that a cubic profile faithfully reproduces the streamwise velocity gradient at all axial locations. Attempts to develop evolutionary equations for this flow should use the higher order velocity profile to insure that the accelerations which exist can be incorporated into the model.

Most theoretical models have shown that the wave velocity and amplitude are uniquely related. Careful measurements by Zabaras (1985) show that the wave amplitude varies widely with both amplitude and wave length. These numerical studies show that for a given amplitude, the computed wave velocity is sensitive to relatively small changes in wave shape, rationalizing the experimental observations and raising questions as to the usefulness of some of the simpler models.

The use of a single wavelength as a scaling parameter for the streamwise hydrodynamics is shown to be incorrect. The present computations show that strong differences in accelerations exist at various positions along the wave. Each of these domains should be analyzed separately if integral equations are to be used, as suggested by Maron et al. (1985). The use of evolutionary equations can eliminate this problem.

Acknowledgment

Financial support of this research by the Office of Naval Research is gratefully acknowledged. F. K. Wasden was supported by a National Science Foundation Graduate Fellowship.

Notation

D = liquid -liquid diffusion coefficient, m^2/s
g = acceleration of gravity, m/s^2
P = pressure, N/m^2
Q = liquid film flow rate per unit perimeter, m^2/s
Re = film Reynolds number, $4Q/\nu$
Sc = Schmidt number, ν/D
u = local streamwise velocity, m/s
v = local velocity normal to boundary, m/s
V_∞ = solitary wave velocity, m/s
x = axial coordinate in lab frame, m
y = coordinate normal to boundary, m
z = coordinate fixed on wave, m
ρ = liquid density, kg/m^3
ν = liquid kinematic viscosity, m^2/s
Δ = Laplacian operator, $\partial^2/\partial x^2 + \partial^2/\partial y^2$

Literature Cited

Bach, P., and J. Villadsen, "Simulation of the Vertical Flow of a Thin, Wavy Film Using a Finite-Element Method," *Int. J. Heat Mass Transfer*, **27**, 815 (1984).

Brown, R. C., et al., "The Use of Wire Probes for the Measurement of Liquid Film Thickness in Annular Gas-Liquid Flows," *Can. J. Chem. Eng.*, **56**, 754 (1978).

Dukler, A. E., "Characterization, Effects and Modelling of the Wavy Gas-Liquid Interface," *Prog. Heat Mass Transfer*, **6**, 207 (1972).

———, "The Role of Waves in Two Phase Flow: Some New Understanding," *Chem. Eng. Educ., 1976 Award Lecture*, 108 (1977).

Gosman, A. D., et al., *Heat and Mass Transfer in Recirculating Fluid Flow*, Academic Press, London (1969).

Hanratty, T. J., and J. A. Campbell, "Measurement of Wall Shear Stress," *Fluid Mechanics Measurements*, R. J. Goldstein, ed., Hemisphere, Washington, DC, 559 (1983).

Huang, P. G., et al., "Discretization of Nonlinear Convection Processes: A Broad-Range Comparison of Four Schemes," *Comp. Meth. Appl. Mech. Eng.*, **48**, 1 (1985).

Kapitza, P. L., "Wave Flow of Thin Layers of a Viscous Fluid," *Collected Papers of P. L. Kapitza*, **II**, Macmillan, New York (1964).

Kheshgi, H. S., and L. E. Scriven, "Disturbed Film Flow on a Vertical Plate," *Phy. Fluids*, **30**, 990 (1987).

Leonard, B. P., "A Stable and Accurate Convective Modelling Procedure Based on Quadratic Upstream Interpolation," *Comp. Meth. Appl. Mech. Eng.*, **12**, 59 (1979).

Levich, V. G., *Physiochemical Hydrodynamics*, Prentice-Hall, New York, 692 (1962).

Mao, Z.-X., and T. J. Hanratty, "The Use of Scalar Transport Probes to Measure Wall Shear Stress in a Flow with Imposed Oscillations," *Exp. Fluids*, **3**, 129, (1985).

Maron, D. M., et al., "Interfacial Structure of Thin Falling Films: Piecewise Modeling of the Waves," *Physico-Chem. Hydrodynam.*, **6**, 87 (1985).

Patankar, S. V., *Numerical Heat Transfer and Fluid Flow*, Hemisphere, Washington, DC, (1980).

Pollard A., and A. L. W. Siu, "The Calculation of Some Laminar Flows Using Various Discretization Schemes," *Comp. Meth. Appl. Mech. Eng.*, **35**, 293 (1982).

Raithby, G. D., "A Critical Evaluation of Upstream Differencing Applied to Problems Involving Fluid Flow," *Comp. Meth. Appl. Mech. Eng.*, **9**, 75 (1976).

Zabaras, G. J., "Studies of Vertical, Annular Gas-Liquid Flow," Ph.D. Diss., Univ. Houston (1985).

Zabaras, G. J., et al., "Vertical Upward Cocurrent Gas-Liquid Annular Flow," *AIChE J.*, **32** (5), 829 (May, 1986).

Manuscript received May 9, 1988, and revision received Aug. 23, 1988.

Reprinted from AICHE JOURNAL, February 1989

Phase Plane and Bifurcation Analysis of Thin Wavy Films under Shear

A long-wave equation for film thickness as a function of position is derived for a general case incorporating viscous, surface tension, and interfacial shear effects. The derivation considers both the parabolic and the power-law velocity profiles. The analysis is aimed at revealing the wave velocity that induces infinitely long (homoclinic) periods as well as substrate thickness and wave peak amplitude. Phase plane analysis shows that at $Re \gg 1$, due to time-scale separation, the homoclinic velocity is near that at the Hopf bifurcation. That enables analytical derivation of the wave characteristics.

Comparison with experimental results in the range of Re-310-3,100 with countercurrent gas flow, shows encouraging agreement. At very high Re the wave velocity suggests the onset of turbulence, in agreement with theory. Phase plane analysis predicts also that the wave shape consists of a simple peak with a steep front, with short waves riding on the main wave at low Re.

M. Sheintuch, A. E. Dukler
Chemical Engineering Department
University of Houston
Houston, TX 77204

Introduction

The prediction of wave characteristics of falling liquid films has been the subject of numerous investigations (Dukler, 1977). Most studies have focused on free-falling films at low Reynolds number (Kapitza and Kapitza, 1949; Alekseenko et al., 1985) and have used linear stability analysis to determine the range of unstable wave velocities and the mode of the fastest growing wave. The film is assumed to be sinusoidal, oscillating about its mean value or even somewhat perturbed from a sinusoidal shape. This type of analysis predicts the wavelength and velocity at the conditions of wave inception. The long-wave approximation (Benney, 1966) considers the limit of very long and shallow waves that reach constant shape in the frame of a moving coordinate. Again, the wave evolves from the mean film thickness. Recent nonlinear analysis searched for wave velocities that induce infinitely long periodic solutions (homoclinic orbits). These studies were limited to falling films at low Reynolds numbers (Pumir et al., 1983) or used a questionable approximation for the flow condition (Needham and Merkin, 1984). Another approach, applied at high Re, is to approximate the wave shape by assuming a sequence of characteristic velocity profiles at different locations along the wave (Maron et al., 1985). Finally, numerical solutions of the evolution equation (Bach and Villadsen, 1984) did show the existence of constant-shape solitary waves. Even at Reynolds number of order 10 such computations are highly time consuming, and problems of numerical instability are encountered.

The purpose of this analysis is to present asymptotic solutions for wave velocities as well as certain dimensional characteristics of falling liquid films experiencing interfacial shear induced by gas flow. For this purpose methods of nonlinear analysis are used. Experiments have shown that at positions well below the plane of wave inception, two classes of waves exist on the surface (Dukler, 1977). Large waves can be observed riding on a thin substrate, with the ratio of peak wave height to substrate thickness ranging from 2 to 4. A second class of waves that are capillary in nature and of much smaller amplitude than the first is also present. These ride on the substrate and are sometimes seen on the trailing edge of the large waves. In the presence of gas flow parallel to the mean surface, interfacial shear is generated and the wave structure changes but the two wave class structure can still be seen. At sufficiently high countercurrent gas flow rates a condition of flooding can be reached where part of the liquid introduced on the vertical surface flows upward.

For complex problems such as this one, two rather divergent approaches are available. At low Reynolds numbers an analyti-

The current address of M. Sheintuch is: Chemical Engineering Department, The Technion, Haifa, Israel.

cal method is possible in the vicinity of certain singular points that can be shown to exist (Chang, 1986). For high Re a different approach is possible if it can be shown that the system is characterized by two or more widely different time scales. This paper takes the latter avenue, which has been largely unexplored. First we derive the integral momentum equation for the film under conditions of constant interfacial shear along the wave. Surface tension effects are incorporated and we assume alternatively a parabolic (laminar) or a power law (turbulent) profile. A complete analysis of the parabolic profile case is developed including interfacial shear while for turbulent flow the solution is explored only for free-falling films in the absence of gas flow.

The analysis strategy is then outlined and this is followed by the development of the solution to the flow equations for the two profiles, neglecting surface tension. For the parabolic profile it is shown that the shear makes no qualitative changes in the behavior of the system, having only a quantitative effect on the interfacial characteristics. As long as flooding is not induced the results are similar to those of the free-falling case. This same conclusion was reached by Zabaras and Dukler (1988) based on experimental observations. Turbulent flow may significantly reduce the wave velocity to a value approaching the mean liquid film velocity. Then the role of surface tension is explored. In the absence of surface tension an ordinary differential equation of the second order is generated and it is shown that the smooth film (Nusselt) solution cannot be a saddle point. When surface tension is added, a third-order ordinary differential equation is generated and every solution may be the saddle point and thus can be the source of the homoclinic orbit. The analysis of this complete form of the problem reveals that capillary waves can exist along the wave and substrate where the profile is flat, in addition to the large, long waves characterized by the homoclinic orbit; this too is in accord with experiment.

Finally, we compare the results with experiments of Zabaras and Dukler (1988).

The Film Equation

The Navier-Stokes equations are integrated in the direction y perpendicular to the wall, using both parabolic and power-law velocity profiles. The work may be extended to higher polynomial velocity profiles by numerical methods. We then apply a moving coordinate frame and arrive at one third-order equation for the film thickness.

Parabolic laminar profile

The film flowing downward under interfacial shear, τ_i, is described by

$$u_t + uu_x + vu_y = \frac{1}{\rho}(-P_x) + g + \nu(u_{xx} + u_{yy}) \tag{1}$$

$$u_x + v_y = 0 \tag{2}$$

subject to

$$u = v = 0 \quad \text{at} \quad y = 0 \tag{3}$$

$$u_y = \tau_i/\mu, \quad v = h_t + uh_x, \quad P = P_0 - \sigma h_{xx} \quad \text{at} \quad y = h \tag{4}$$

With integration in the y direction, Eq. 1 yields

$$Q_t + \frac{\partial}{\partial x}\int_0^h u^2\,dy = gh + \frac{\sigma h}{\rho}h_{xxx} + \nu\left[\int_0^h u_{xx}\,dy + \frac{\tau_i}{\mu} - u_y(0)\right] \tag{5}$$

with the local flow rate

$$Q = \int_0^h u\,dy \tag{6}$$

Assume a quadratic velocity profile that satisfies the conditions, $u = 0$ at $y = 0$; $\tau_i/\mu = du/dy$ at $y = h$; and $Q(h) = \int_0^h u\,dy$. This yields the following distribution function

$$u = \frac{Q}{h}\frac{3}{2}\eta(2 - \eta) + \frac{\tau_i}{\mu}\frac{h}{2}\eta\left(\frac{3}{2}\eta - 1\right) \tag{7}$$

with $\eta = y/h$. Clearly, this equation also describes the distribution in the undisturbed film (steady state) as well. With this distribution the following integrals can be evaluated.

$$\int_0^h u^2\,dy = \frac{6}{5}\frac{Q^2}{h} + \frac{Q\tau_i h}{20\mu} + \frac{h^3}{120}\left(\frac{\tau_i}{\mu}\right)^2 \tag{8}$$

From Eq. 6 the second x derivative of Q can be evaluated.

$$Q_{xx} = h_{xx}u(h) + h_x\frac{\partial}{\partial x}u(h) + h_x u_x(h) + \int_0^h u_{xx}\,dy \tag{9}$$

For the parabolic profile the last integral can then be evaluated.

$$\int_0^h u_{xx}\,dy = Q_{xx} - h_{xx}\left(\frac{3}{2}\frac{Q}{h} + \frac{1}{4}\frac{\tau_i}{\mu}h\right) - h_x^2\left(\frac{3Q_x}{hh_x} - \frac{3Q}{h^2} - \frac{\tau_i}{2\mu}\right) \tag{10}$$

Substituting these quantities into Eq. 5 gives the following equation for the case of constant shear independent of x.

$$Q_t + Q_x\left(\frac{12}{5}\frac{Q}{h} + \frac{1}{20}\frac{h\tau_i}{\mu}\right) + h_x\left(-\frac{6}{5}\frac{Q^2}{h^2} + \frac{Q\tau_i}{20\mu} + \frac{h^2}{40}\frac{\tau_i^2}{\mu^2}\right) - \left(g - \frac{1}{\rho}\frac{dP}{dx}\right)h + \nu\left(\int_0^h u_{xx}\,dy - \frac{3Q}{h^2} + \frac{3}{2}\frac{\tau_i}{\mu}\right) + \frac{\sigma h}{\rho}h_{xxx} \tag{11}$$

with $\int_0^h u_{xx}\,dy$ defined in Eq. 10. The integral of the continuity equation is

$$Q_x + h_t = 0. \tag{12}$$

Thus Eqs. 11 and 12 are two equations in h and Q as dynamic variables and x and t as independent variables. In a coordinate

frame moving with the wave velocity, c, set

$$\theta = t, \quad \xi = x - ct \tag{13}$$

and the mass conservation condition then becomes

$$h_\theta - ch_\xi + Q_\xi = 0 \tag{14}$$

The momentum balance, Eq. 11, can be modified by substituting $Q_\theta - cQ_\xi$ for Q_t, and $\partial^n/\partial\xi^n$ for ∂^n/dx^n. We make now two important assumptions:

1. The waves propagate without change in shape; thus in a moving coordinate system, $Q_\theta = h_\theta = 0$. Integration of Eq. 14 yields

$$Q - ch = K \tag{15}$$

where Q is the volumetric flow rate at any location ξ along the wave.

2. The integration constant, K should satisfy the steady state solution with $h = h_o$ and $Q = Q_F$, the liquid feed rate. Thus $K = Q_F - ch_o$. By integrating the velocity distribution over the steady state film thickness we find that

$$Q_F = \frac{gh_o^3}{3\nu}(1 + T) \tag{16}$$

with the dimensionless shear $T = 3\tau_i/2\rho g h_o$. Note that Eq. 16 may have more than one real solution for h_o given Q_F and τ_i, as discussed in detail by Maron and Dukler (1984). Substituting K calculated from the steady state solution, Eq. 15 becomes

$$Q = \frac{gh_o^3}{3\nu}(1 + T)[1 + n(H - 1)], \quad H = \frac{h}{h_o}, \quad n = \frac{ch_o}{Q_F} \tag{17}$$

where n is the wave velocity made dimensionless in respect to the average velocity. Substitution of Eq. 17 into the momentum balance, Eq. 11, yields an ordinary third-order differential equation describing the change of dimensionless film thickness, H, with dimensionless length $l = \xi/L$. The length scale, L, and dimensionless parameters are defined as

$$L = \frac{h_o Re}{1 + T} \quad Re = \frac{Q_F}{\nu} \quad W = \frac{\sigma}{\rho g^{1/3}(3\nu^2)^{2/3}} \tag{18}$$

The resulting equation is

$$\epsilon_1 H^3 H_{lll} + \epsilon_2[C_2(H)H_{ll} - C_3(H)H_l^2] + (1 + T)^2 C_1(H)H_l + C_0(H) = 0 \tag{19}$$

where

$$\epsilon_1 = \frac{27W(1 + T)^{11/3}}{Re^{11/3}} \quad \text{and} \quad \epsilon_2 = \frac{27(1 + T)^3}{Re^2}$$

In this development the dimensionless shear stress τ_i is assumed to be independent of the position along the wave l and the coefficients are:

$$C_0 = (H - 1)[H^2 - (T + 1)(n - H - 1)]$$

$$C_1 = -\frac{n^2}{5}\left(H - \sqrt{6}\frac{n - 1}{n}\right)\left(H + \sqrt{6}\frac{n - 1}{n}\right) - \frac{TH^2}{10(1 + T)}\left(2nH + 1 - n + \frac{TH^2}{1 + T}\right)$$

$$C_2 = H\left[\frac{3}{2}(n - 1) - \frac{nH}{2} - \frac{1}{2}\frac{H^2T}{1 + T}\right]$$

$$C_3 = 3(n - 1) - \frac{H^2T}{1 + T} \tag{20}$$

These equations apply for downflow of liquid with countercurrent gas flow ($g > 0, \tau_i < 0, -1 \le T \le 0$) or cocurrent flow ($g > 0, \tau_i > 0, T > 0$) as well as for upflow where x or l is positive in the flow direction ($g < 0, \tau_i > 0, T \le -1$); the inequality, $T \le -1$, follows from the requirement that Q_F be positive in Eq. 16.

A schematic representation of the relation between T and h_o as deduced from Eq. 16 appears in Figure 1 for constant Q_F. Downflow with countercurrent shear takes place for $-1 \le T \le 0$ (band B in the figure). However in the range $-3/4 < T < 0$ the velocities are directed uniformly downward at all locations in the film. For $T = -3/4$ the profile is symmetric, with zero velocity at the interface, and when $-1 < T < -3/4$, downward-directed velocities exist near the wall, with upward velocities near the interface. Band A in Figure 1 represents concurrent downward flow while band C displays the behavior for concurrent upward flow. In these bands, for the range $-1.5 < T < -1$, the velocity profile is again not monotonic. For more negative values of T uniformly upward flow exists in the film. *At* $T = -1.5$ the wall shear is zero and the upward motion of the liquid is driven by the interfacial shear only. The existence of these different patterns of velocity distribution was discussed by Maron and Dukler (1984) and their existence confirmed experimentally by Zabaras et al. (1986).

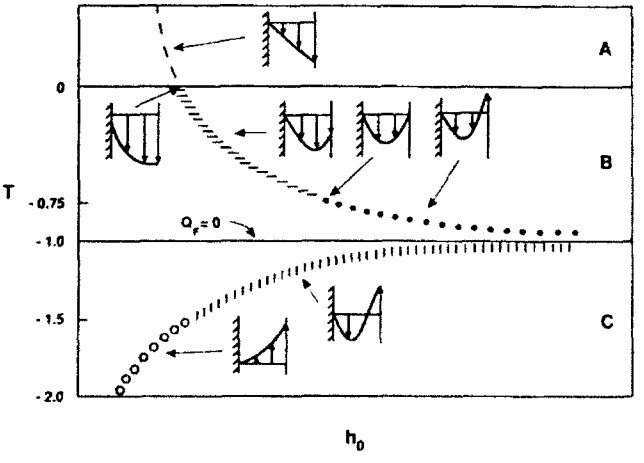

Figure 1. Solutions to steady state film thickness equation.

Turbulent profile in the absence of shear

For turbulent flow, the film velocity profile can be expressed in a power law form:

$$u = \frac{(1+\alpha)}{\alpha}\frac{Q}{h}\eta^{1/\alpha} \tag{21}$$

We find

$$\int_0^h u^2\,dy = \frac{(1+\alpha)^2}{\alpha(2+\alpha)}\frac{Q^2}{h} \qquad \int_0^h u\,dy = Q \tag{22}$$

The integral momentum equation then becomes:

$$h_t\left(-c^2 + \frac{(1+\alpha)^2}{\alpha(2+\alpha)}\frac{Q(2ch-Q)}{h^2}\right) = gh - \frac{\tau_w}{\rho} + \nu h_{\xi\xi}\left(c - \frac{(1+\alpha)}{\alpha}\frac{Q}{h}\right) + O(h_t^2) \tag{23}$$

$$Q - ch = Q_o - ch_o \tag{24}$$

For turbulent flow the wall shear stress τ_w cannot be approximated from the velocity profile and correlations are needed. As shown below, this has no influence on the dimensionless wave velocity but does change the mean film thickness and consequently the dimensional velocity. From the Blasius relation

$$\frac{\tau_w}{\rho} = \frac{1}{2}\bar{u}^2\cdot\frac{\lambda}{8}; \quad \bar{u} = \frac{Q}{h} \tag{25}$$

where the friction factor at the wall, λ, is estimated from single-phase flow models.

$$\frac{\lambda}{8} = 0.056(Q/\nu)^{1/4} \tag{26}$$

When this relation is substituted into Eq. 24 for the flat film, we find

$$\frac{h_{o(\text{turb})}}{h_{o(\text{lam})}} = 0.21\,Re^{1/4} \tag{27}$$

In the application of Eq. 23 at high flow rates the value of α can be expected to vary along the wave. At the substrate the local flow rate is low, turbulence is suppressed, and the quadratic law will apply. In the thicker portions of the wave near the crest, turbulent behavior will result in increased values of α. Methods for accounting for this flow direction variation in α have not yet been fully implemented. As a first approximation we use a constant value of α for the dynamic analysis of the momentum equation.

Strategy of Dynamic Analysis

The dynamic equation for the film thickness, Eq. 19, contains four parameters, Re, W, n, and T, which are to be specified as input variables. Even though the slopes of the waves are known to be small it is not possible to simplify the equation by neglecting the H_{II} and H_{III} terms since these quantities are necessary to the stability and dynamic analysis that follows. Define the following dimensionless term

$$\beta = \frac{\epsilon_2}{\epsilon_1}(1+T)^2 = \frac{(1+T)^{4/3}Re^{5/3}}{W} \tag{28}$$

When β is large the inertial forces are large compared to the surface forces and the first term in Eq. 19 can be neglected.

The steady state solution of Eq. 19 is the space-independent ($H_I = H_{II} = H_{III} = 0$) solution of $C_0(H) = 0$. The qualitative nature of these solutions is shown in Figure 2 for different ranges of T. The unperturbed film ($H = 1$) is always a solution but there is always a range of velocities n for which it is not stable. The other two solutions, for any T, form a parabolic branch $n = H^2/(1+T) + (1+H)$ which intersects $H = 1$ at $n = (3+2T)/(1+T)$ and acquires a turning point at $H = -(1+T)/2$, $n = (3-T)/4$. The parabolas for upflow, Figure 2a, and downflow, Figure 2b, open in opposite directions. The range of values of n over which the $H = 1$ solution is unstable can be determined from linear stability analysis. Specifically, there will usually exist a (Hopf) bifurcation point, which is the value of n at which a transition to periodic behavior takes place and oscillations are observed in the frame of a moving coordinate; that is, waves propagate along the film in the physical system. The H–n diagram for $T = 0$ showing the nature of the various states as determined by linear stability analysis is shown in Figure 3. As the waves grow, their velocities vary in the direction of lower n (more unstable). The waves form a family of closed curves (limit cycles) in the phase plane (H_I vs. H) or phase space (H_{II}, H_I, H) and these closed curves increase in area as the waves grow in amplitude along the film in the coordinate direction. These waves have a peak such that $H > 1$ and a substrate thickness $H < 1$. As the wave grows the substrate becomes smaller. At the condition where the substrate thickness is equal to that of the saddle point the wave can grow no more and its velocity will not change. In the phase plane the largest possible wave will be formed when the limit cycle hits a saddle point forming a homoclinic curve. This curve provides the asymptotic amplitude of the wave and the corresponding velocity, n_s. Further change in n cannot take place since this results in the elimination of the oscillations. The wavelength of this form is infinite since the motion takes place in the vicinity of the saddle point, which is a steady state, and thus is infinitely long. The saddle point satisfies the steady state solution $C_0(H_3) = 0$.

The purpose of the nonlinear analysis is to determine the location, n_s, and form of the homoclinic curve (also termed saddle-loop bifurcation). That is possible analytically only in two cases:

1. In the small neighborhood of higher order singularities such as when Hopf and saddle-node bifurcations coalesce. Then

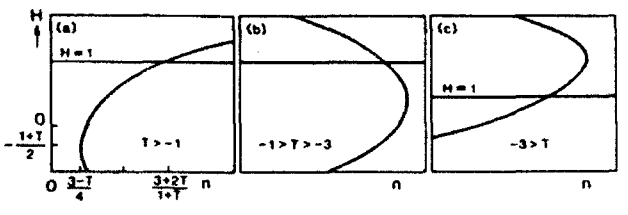

Figure 2. Variation of steady state film thickness with n.

a. Downflow; b, c. Upflow
Coordinates for limit points in (b) and (c) same as in (a)

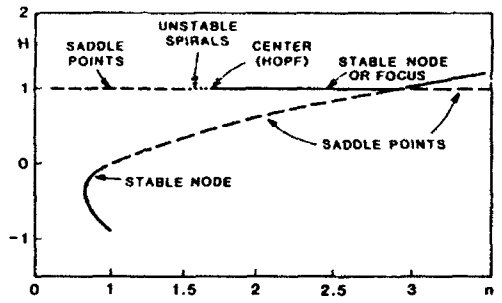

Figure 3. Changes in the nature of the steady states.
Determined from linear stability analysis for $T = 0$ and negligible surface forces

a. $n = n_H$; b. $n < n_H$
c. $n = n_s \rightarrow h_H$; d. $n > n_H$

the oscillations are infinitesimally small and can be described by perturbation of the linear solution.

2. When the system is characterized by different time scales.

We capitalize here on the latter property.

The dynamic analysis of Eq. 19 requires working in the three-dimensional phase space, H, H_I, H_{II}. However many of the essential dynamic features of the system can be discerned by analyzing the phase plane H, H_I. Equation 19 reduces to this problem for high Reynolds numbers when $\beta \rightarrow \infty$. Thus the procedure will be to first analyze the simplified system in the phase plane for both laminar and turbulent flow. Then the analysis will be generalized for cases where β is not large.

Laminar Film Flow for $\beta \rightarrow \infty$

In the case $W = 0$, Eq. 19 can be written in the form

$$H_I = w \tag{29}$$

$$\epsilon_2 C_2 w_I = -(1 + T)^2 C_1 w - C_0 + \epsilon_2 C_3 w^2 = f(H, w) \tag{30}$$

Linear stability analysis requires the determination of the eigenvalues of the Jacobian matrix $\partial(w, f/\epsilon_2 C_2)/\partial(H, w)$ at the steady state $H = 1$, $w = 0$. The matrix is then

$$J = \begin{pmatrix} 0 & 1 \\ \dfrac{f_h}{\epsilon_2 C_2} & \dfrac{f_w}{\epsilon_2 C_2} \end{pmatrix} \tag{31}$$

and the state may destabilize by one of two ways:

1. A Hopf bifurcation to periodic behavior occurs at

$$\text{tr } J = \frac{f_w}{\epsilon_2 C_2} = -\frac{(1 + T)^2 C_1(1)}{\epsilon_2 C_2(1)} = 0 \quad |J| > 0 \tag{32}$$

The state is unstable for $C_1(1)/C_2(1) < 0$, or from Eq. 20 with $T = 0$,

$$\frac{3}{2} < n < \frac{6}{5} + \frac{\sqrt{6}}{5} = n_H \tag{33}$$

2. Exchange of stability from $H = 1$ to the $H \neq 1$ solution occurs when

$$|J| = -\frac{f_H}{\epsilon_2 C_2} = \frac{C_{0H}(1)}{\epsilon_2 C_2} = 0; \quad C_{0H}(1) = \frac{dC_0}{dH}(1) \tag{34}$$

yielding $n = 3$ when $T = 0$, that is, at the intersection point of the two branches. These transitions are observed in Figure 3 where the unstable branches are marked by broken lines.

Oscillations (waves) exist for a certain range of n as shown in Eq. 33. We show now that when $\epsilon_2 = 27(1 + T)^3/Re^2 \rightarrow 0$ the wave velocity at the homoclinic orbit is very close to that at the Hopf ($n_s \rightarrow n_H$). Note that ϵ_2 does not affect the stability boundaries, Eq. 32, but it affects the behavior in the phase plane. From Eq. 30, with $T = 0$ and when the small $\epsilon_2 C_3 w^2$ term is ignored, the direction of the motion (slope in the $H - H_I$ plane) is

$$\frac{dw}{dH} = \frac{\dfrac{n^2}{5}(H - H_4)(H + H_4)w - (H - 1)(H - H_2)(H - H_3)}{\epsilon_2 w H \dfrac{n}{2}(-H + H_5)} - \frac{f(H, w)}{\epsilon_2 w C_2(H)} \tag{35}$$

where $H_{2,3}$ are the roots of $C_0(H) = 0$ with H_4 and H_5 defined from Eq. 20 after setting $T = 0$.

$$H_{2,3} = -0.5 \pm \sqrt{n - 0.75}$$

$$H_4 = \sqrt{6}\,\frac{n - 1}{n}$$

$$H_5 = \frac{3(n - 1)}{n} \tag{36}$$

Since ϵ_2 is small, $dw/dH \rightarrow \infty$ everywhere in the phase plane except when the numerator vanishes. At this condition of $f = 0$

$$w = \frac{(H - 1)(H - H_2)(H - H_3)}{\dfrac{n^2}{5}(H - H_4)(H + H_4)} \tag{37}$$

The shape of the w vs. H curves resulting from this expression are dependent on the velocity, n, since $H_{1\text{-}5}$ are functions of n. Figure 4a shows the solution of Eq. 37 at $n = n_H = 1.689$, Eq. 33. $H = 1$ is one branch of the solution for all w since $H_4 = 1$ at $n = n_H$. The second branch crosses this $H = 1$ branch and intersects the abscissa at H_3. We have already shown that for any point in the phase plane the trajectory must be vertical except near the $f = 0$ curves. Thus all trajectories starting at $H < 1$ flow toward the second branch except for those that originate in the immediate vicinity of the $H = 1$ line. Along the curves the trajectory must be horizontal. As the $f = 0$ lines are approached the trajectory must move along the $f = 0$ curve and increasingly close to it in direction. This direction is indicated in the usual way by heavy arrows on the solution branches. The sign of w_I is an indicator of the direction of the vertical trajectories. As seen in Eq. 30, this direction changes as $f(H, w)$ passes through zero. Similarly, the sign of H_I is an indicator of the direction of horizontal motion. Eq. 29 shows that this direction changes as w passes

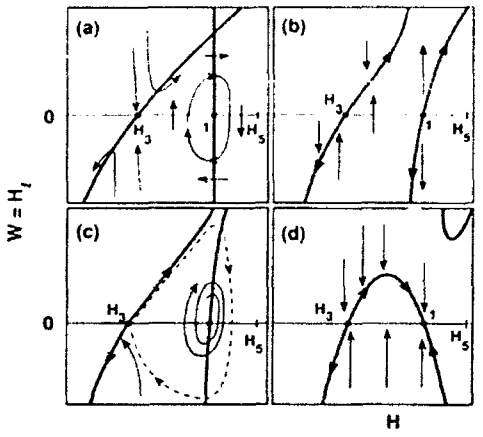

Figure 4. Phase-plane analysis of two-variable model.
Heavy lines, $f = 0$; thin lines, direction of motion

a. $n < n_H$; b. $n_H < n < n_t$,
c. $n = n_t$ for $Re \to \infty$; d. $n = n_t$

through zero. Equation 35 shows that trajectories cannot cross the $H = H_5$ boundary since at this point $C_2(H) = 0$ and a discontinuous change in the direction of motion occurs. When this begins to happen the surface tension terms neglected here become important. Thus waves that initiate from the smooth film cannot achieve an amplitude greater than H_5.

Solutions of Eq. 37 for $n < n_H$ and $n > n_H$ appear in Figures 4b and 4d. In the latter case the steady state, $H = 1$, is stable and all trajectories in its vicinity are attracted there. For $n < n_H$ in Figure 4b, the steady state at $H = 1$ is unstable and all trajectories escape to infinity. Of particular interest is the case where $n \to n_H$, illustrated in Figure 4c. The Hopf theorem indicates that a limit cycle surrounds the unstable state, $H = 1$, near the condition for a Hopf bifurcation. Thus the situation appears as shown in Figure 4c for n somewhat less than n_H. Periodic oscillations wind out in a spiral from its origin at $H = 1$ and gradually grow in amplitude until they disappear in a homoclinic orbit at H_3.

Now it is possible to deduce that the value of n_t at which this takes place must be negligibly different from n_H when ϵ_2 is small. Under these conditions the trajectories are almost vertical, and the limit cycle must be narrow in the H direction and long in the v direction. If the two branches of the $f = 0$ curve are far apart, as they are when n is significantly lower than n_H, the trajectories can readily escape to infinity. As ϵ_2 increases, the trajectories continue to flow toward the left branch of the $f = 0$ curve but now they can travel a short distance, ϵ_2, away from these curves. The separation distance between the two $f = 0$ curves increases as $n_t - n_H$. Thus for the trajectory to move from $H = 1$ on one branch of $f = 0$ to H_3 on the other requires that $n_t - n_H$ be of the order of ϵ_2, a small number under the experimental conditions of interest here. Thus we conclude that $n_t = n_H$.

Pictures of the developing waves can be arrived at by analyzing the trajectory in the phase plane, as shown in Figure 5. The initially flat interface (*a*) displays small sinusoidal waves at the point of wave inception (*b*) with the wave velocity, $n = n_H = 1.689$, Eq. 33, at this condition. But the condition is unstable and the spiral unwinds around $H = 1$ to become a homoclinic orbit at $n = n_t$ in close proximity to n_H. In its homoclinic orbit the minimum or substrate wave amplitude is $H_3 = 0.47$ (Eq. 36 for $n = n_H$). H then increases rapidly at the front of the wave with high

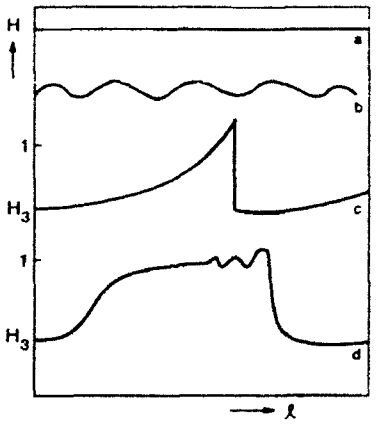

Figure 5. Qualitative sketch of wave profile.

slope, w. As it approaches its peak amplitude the slope drops to zero. The peak cannot exceed $H_5 = 1.25$. Then the sign of the slope changes and along the back the wave tapers more slowly down to the substrate thickness, H_3.

The existence of countercurrent shear does not change this qualitative picture, modifying only the wave characteristics. Steady states are linearly unstable when $C_1(1)/C_2(1) < 0$ or

$$\left(\frac{3}{2} + \frac{s}{2}\right) < n < n_H = \frac{6}{5} + \frac{s}{20} + \frac{\sqrt{6}}{5}\sqrt{1 + \frac{22s}{24} + \frac{41s^2}{96}} \qquad (38)$$

where $s = T/(1 + T)$. The upper root of $C_1(1) = 0$ is n_H and this is the solution of

$$-\frac{n^2}{5}\left[1 - 6\left(\frac{n-1}{n}\right)^2\right] - \frac{s}{10}(1 + n + s) = 0 \qquad (39)$$

The other stability boundary, $J = 0$, occurs at $n = 3 - s$. A map of the linear stability appears in Figure 6 for downflow with countercurrent ($s < 0$) or cocurrent ($s > 0$) shear. The relative positions of the three boundaries are identical to those for the free-falling film problem. They intersect at $s = 1$, $n = 2$, which does not correspond to any physical situation ($T \to \pm\infty$). For upward flow ($T < -1$, $s > 1$) the relative positions of the three

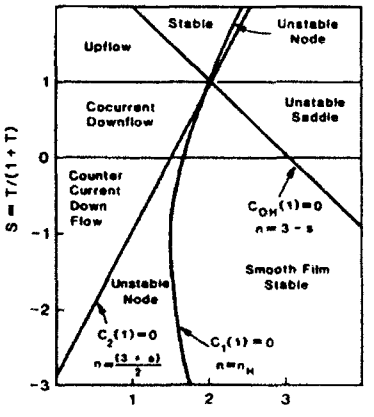

Figure 6. Stability map for smooth film in the presence of shear for two-variable case.

bifurcations are interchanged. The phase plane analysis for downflow with countercurrent shear is analogous to the $T = 0$ case. At $n = n_H$, $H = 1$ is a solution for any w and the $f = 0$ curve acquires the shape of Figure 4a. Changing n modifies the diagram in a similar fashion and we conclude again that a homoclinic orbit must exist close to n_H with the same general shape as in Figure 5. The substrate height, H_3, and the limiting wave amplitude, H_5, are given by

$$H_3 = \frac{-1 + \sqrt{1 + 4(n_H - 1)(1 - s)}}{2(1 - s)}$$

$$H_5 = \frac{-1 + \sqrt{n^2 + 12n - 1}}{2s} \tag{40}$$

This analysis shows the following behavior of the system for downflow with countercurrent shear

1. The wave characteristics depend on the shear parameter, T (or s)
2. The wave velocity, n, which approximates the velocity at the Hopf bifurcation, varies weakly with T (or s), taking on values of 1.69 at $T = 0$ ($s = 0$), 1.5 at $T = -\frac{1}{2}$ ($s = -1$), and 1.75 at $T = -\frac{3}{4}$ ($s = -3$)
3. The maximum wave amplitude increases markedly with countercurrent shear since H_5 increases as s becomes more negative

Extension of the analysis to upflow shows that the relative positions of the bifurcation points, Figures 2, 6, are arranged in a mirror image to the downflow case and the conclusions are thus similar for cocurrent flow. However the existence of multiple values of the equilibrium film thickness for any shear stress and flow rate as discussed above raises these additional issues:

1. Either one or both of these solutions may not be stable
2. The location of the turning point at $n = (3 - T)/4$ may be outside the domain where oscillations can exist

Turbulent Film Flow

The analysis of Eq. 19 for laminar film flow presented above showed that $C_1(H = 1) = 0$ is a necessary condition for instability (see also Figure 6). Note that C_1 is the coefficient of H_l, the slope of the wave in dimensionless form, and $H = 1$ is the condition for the smooth film, $h = h_o$, $Q = Q_F$. For turbulent flow the same condition can be shown to exist. Thus, the coefficient of the dimensional slope, h_ξ, in Eq. 23 must be zero, resulting in the following relation for the dimensionless wave velocity.

$$-n^2 + 2f(\alpha)n - f(\alpha) = 0 \quad f(\alpha) = \frac{(1 + \alpha)^2}{\alpha(2 + \alpha)} \tag{41}$$

or

$$n = f(\alpha) + \sqrt{f(f - 1)} \tag{42}$$

This result is independent of the particular form of the correlation used for the wall stress. At high flow rates, as the flow becomes more turbulent α increases and n approaches 1.0. Thus for a velocity distribution that follows a 1/7th power law, $n = 1.14$. It should be noted that such low values of the wave velocity cannot be predicted from any laminar distribution but have been observed experimentally for high flow rates, Eq. 12.

Laminar Films with Surface Forces: General Case

When surface tension effects are retained in the model a general form of Eq. 19 can be written as follows where $w = H_l$ and $\phi = w_l$:

$$\phi_l = \frac{f(H, w) - \epsilon_2 C_2 \phi}{\epsilon_1 H^3} = \frac{g(H, w, \phi)}{\epsilon_1 H^3} \tag{43}$$

where $w = H_l$ and $\phi = w_l$ and $f(H, w)$ is defined in Eq. 30. The Jacobian matrix at $H = 1$, $w = \phi = 0$ is:

$$J = \begin{pmatrix} 0 & 1 & 0 \\ 0 & 0 & 1 \\ -\dfrac{C_{0H}(1)}{\epsilon_1} & -\dfrac{C_{1H}(1)}{\epsilon_1} & -\dfrac{\epsilon_2}{\epsilon_1} C_2(1) \end{pmatrix} \tag{44}$$

The characteristic equation, $|J - \lambda \bar{I}| = 0$, is

$$\lambda^3 + \frac{\epsilon^2}{\epsilon_1} C_2(1)\lambda^2 + \frac{(1 + T)^2 C_1(1)}{\epsilon_1}\lambda + \frac{C_{0H}(1)}{\epsilon_1} = 0 \tag{45}$$

and its roots are the eigenvalues that determine the stability. Applying Routh-Hurwitz stability criteria reveals that $H = 1$ is stable ($\lambda_1, \lambda_2, \lambda_3 < 0$) if the following three conditions are satisfied

$$\text{(a)}\ C_{0H}(1) > 0$$

$$\text{(b)}\ C_2(1) > 0$$

$$\text{(c)}\ \frac{C_{0H}(1)}{\epsilon_1} - \frac{(1 + T)^2 C_1(1) C_2(1) \epsilon_2}{\epsilon_1^2} > 0 \tag{46}$$

Condition (a) is the exchange of stability, described earlier, and it implies $n < 3 - s$. Condition (b) is also unchanged, requiring $n > (3 + s)/2$. Hopf bifurcation occurs when condition (c) is violated and the bifurcation points depends now on the ratio of the viscous to surface tension terms. It reduces either to the previous Hopf condition ($C_1 = 0$) when $\epsilon_2/\epsilon_1 \to \infty$ or to condition (a) when $\epsilon_2/\epsilon_1 \to 0$. Substituting the relations for the $C_i(H)$, Eq. 20, we find that Hopf bifurcation ($n = n_H$) occurs at

$$\beta = \frac{(1 + T)^{4/3} Re^{5/3}}{W}$$

$$= \frac{(3 - s - n)10}{\left(n - \dfrac{3}{2} - \dfrac{s}{2}\right)[-2n^2 + 12(n - 1)^2 - s(1 + n + s)]} \tag{47}$$

The nature of the steady state is shown in the (β, n) plane of Figure 7 by denoting the sign of the three eigenvalues. Limit cycles may exist in the range $(3 + s)/2 < n < n_H$ and the order of the various points is unaffected by changing T for downward flow.

Analysis of the trajectories in the three-dimensional space (H, w, ϕ) is more intricate than the two-dimensional version. The structure of the analysis follows. We investigate the shape of the $g = 0$ surface, Eq. 43, in the phase space to show that it attracts the motion and ask: is the motion along it stable? It

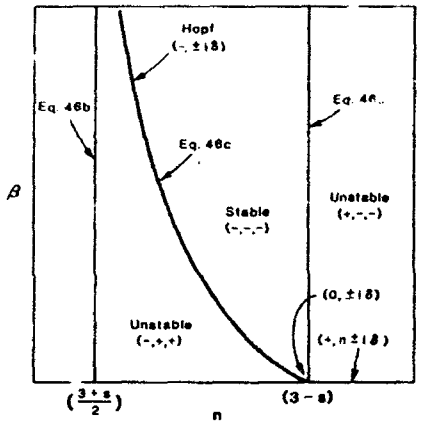

Figure 7. Stability map for general case.

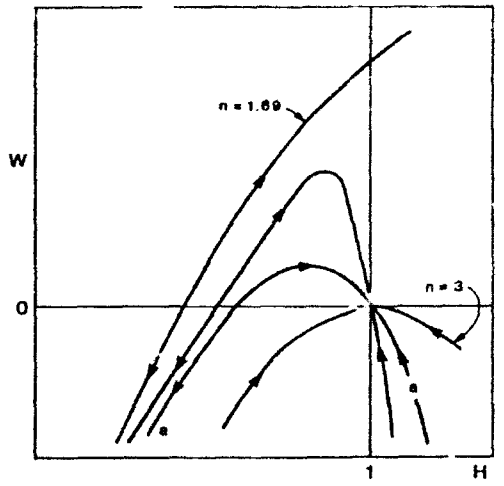

Figure 8. Family of $f = 0$ curves in w–H plane.

turns out that it is unstable in certain sections. We find the stable and unstable manifold and construct the trajectory in space. The steady state $H = 1$ may be the origin of the homoclinic orbit. It has a stable one-dimensional (i.e., a line) manifold and an unstable two-dimensional (surface) manifold along which the motion spirals. These spirals yield the capillary wave and are evident only with relatively small Re (ϵ_1/ϵ_2 large). After it spirals out, the trajectory travels in the vicinity of H_3 so that the dimensionless value of the film thickness is still a good approximation for the substrate thickness.

The slopes of the trajectories can be found readily from Eq. 43 to be:

$$\frac{d\phi}{dH} = \frac{g}{\epsilon_1 H^3 w} \quad \frac{d\phi}{dw} = \frac{g}{\epsilon_1 H^3 \phi} \tag{48}$$

Note that $\epsilon_1 \to 0$ except for the lowest Reynolds numbers. Therefore the slopes of the trajectories in both the $\phi - H$ and $\phi - w$ planes are steep everywhere in the phase space except where $g \to 0$ or when the first and second derivatives of the wave profile, w and ϕ, are large. Data show that these derivatives are everywhere very small indeed. Therefore we now explore the region around $g = 0$.

From the definition for g in Eq. 43, when $g = 0$

$$\phi = \frac{f(H, w)}{\epsilon_2 C_2(H)} \tag{49}$$

For $\epsilon_2 = 0$ this implies that $f = 0$, a situation that was explored earlier. This can be pictured as a cylindrical surface in the phase space perpendicular to the $w - H$ plane. Figure 8 shows $f = 0$ curves for a sequence of values of n as determined from Eq. 37. The case for $n = 1.69$ appeared earlier in Figure 4a where it was shown that the crossing of the abscissa marks the location of H_3, the substrate height. Note that when $n = 3$ the value of H_3 becomes identical with the smooth film thickness, a condition in agreement with the experiment.

Figure 9 pictures the cylindrical surface, $g = 0$, in the phase space ϕ, w, H for $\epsilon_2 = 0$. When ϵ is small but not zero the surface is tilted somewhat. All trajectories starting from any point in the phase space not on $g = 0$ rapidly approach this plane since $\partial\phi/\partial H$ and $\partial\phi/\partial w$ are large. This is evident from Eq. 48 for the condition $\epsilon \to 0$. Once the trajectory reaches the $g = 0$ surface it can be described by the relations

$$H_l = w \quad w_l = \phi = f/\epsilon_2 C_2(H) \tag{50}$$

This is identically the two-dimensional model developed earlier, but the question of stability at any position on the surface must still be explored.

Suppose $H_o(l)$, $w_o(l)$, $\phi_o(l)$ is the solution to Eq. 43 along $g = 0$ with perturbations from this motion $\tilde{H} = H(l) - H_o(l)$, $\tilde{w} = w(l) - w_o(l)$ and $\tilde{\phi} = \phi(l) - \phi_o(l)$ described by

$$\tilde{H}_l = \tilde{w} \quad \tilde{w}_l = \phi \quad \epsilon_1 H^3 \tilde{\phi}_l = g_H \tilde{H} + g_w \tilde{w} + g_\phi \tilde{\phi} \tag{51}$$

Assume that perturbations in H are small and grow slowly so that $g_H = \partial g/\partial H$ can be averaged, and $\langle g_H \rangle$, $\langle g_w \rangle$, and $\langle g_\phi \rangle$ replace the original time-dependent g_H, g_w, g_ϕ. The motion is stable if the trivial solution of Eq. 51, $\tilde{H} = \tilde{\phi} = \tilde{w} = 0$ is stable, that is, if the eigenvalues are all negative. We do a stability analysis similar to that leading to Eq. 46 to find the stability condition

$$-\frac{\langle g_H \rangle}{\epsilon_1 H^3} - \frac{\langle g_\phi \rangle \langle g_w \rangle}{H^6 \epsilon_1^2} < 0 \tag{52}$$

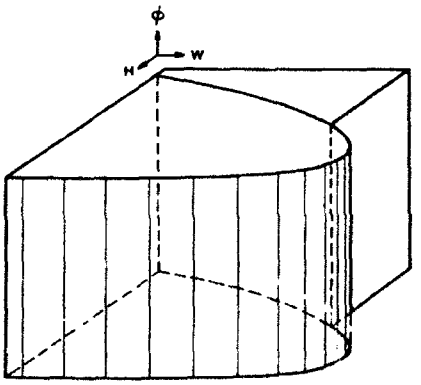

Figure 9. $g = 0$ surface in phase plane.

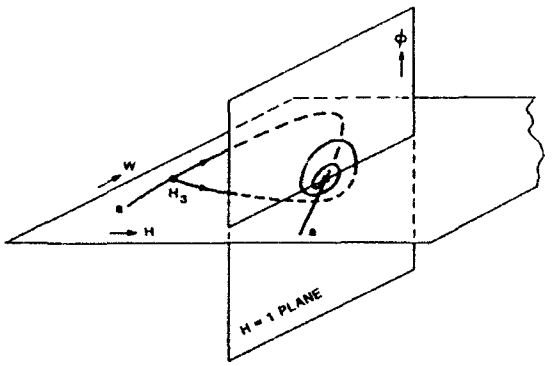

Figure 10. Trajectory of limit cycle.

or

$$\frac{\epsilon_2}{\epsilon_1}\frac{C_2}{H^3} > \frac{\partial}{\partial H}\left(\frac{C_0}{C_1}\right) = -\left(\frac{dw}{dH}\right)_{f=0} \tag{53}$$

An analysis of this equation shows that the transition occurs at $H = 1$. The section $H < 1$ is stable and is the stable manifold near $H = 1$. The motion around $H > 1$ is unstable and the trajectory oscillates around the line $f = 0$.

We now describe the motion in the vicinity of $H = 1$ with $n \sim n_H$. The stable manifold is the portion of the curve $f = 0$, denoted *aa* in Figure 10, that connects the H_3 and $H = 1$ solutions, denoted *ABC*. Its trajectory flows toward the steady state. At $n = n_H$ (Hopf point) there is a pair of imaginary eigenvalues and one negative eigenvalue:

$$\lambda_1 = -\frac{\epsilon_2}{\epsilon_1}C_2(1), \quad \lambda_{2,3} = \pm i\left(\frac{(1+T)^2 C_1(1)}{\epsilon_1}\right) \equiv \pm i\delta \tag{54}$$

The oscillations develop or decay with a period of $\sim(\epsilon_1, C_1(1))^{1/2}$. Since $C_1(1) \sim O(\epsilon_1/\epsilon_2)$ short periods of $O(\sqrt{\epsilon_1})$ are expected when the surface tension is important, while when surface tension effects are negligible the period is of $O(\sqrt{\epsilon_2})$. The eigenvectors that correspond to these imaginary eigenvalues were calculated to be $\phi = \delta^2(H-1)$ and $\phi = \pm i\delta w$; they define the unstable manifold. We note however that $\delta^2 \to \infty$ as $\epsilon_1 \to 0$ or $\epsilon_2 \to 0$. Thus $\delta^2(H-1)$ is finite only for $H = 1$. The plane $H = 1$ is thus a good approximation for the unstable manifold. For n somewhat smaller than n_H, λ_1 does not change significantly, while $\lambda_{2,3} = \Psi \pm i\delta$. The frequency is of order $\epsilon_1^{-1/2}$ or $\epsilon_2^{-1/2}$ as before and Ψ is the amplitude growth rate, which is small for high surface tension and large at the other extreme. For extremely small values of $(n_H - n)$ a limit cycle exists and it lies close to the $H = 1$ plane. Further increase in $(n_H - n)$ will break the cycle and the trajectory is detached from the plane and moves fast toward the stable manifold ($f = 0$). The resulting motion in Figure 10 shows a closed curve composed of a spiraling motion on $H \sim 1$ followed by a loop that travels around H_3. In the time domain we find small capillary waves whose number

Table 1. Wave Characteristics of Free-Falling Film ($T = 0$)

Re	β	h_0 mm	Q_F/h_0 cm/s	c cm/s	n Meas.	n Theory	Substrate Meas.	Substrate Theory
78	1.18	0.28	28.2	68	2.58	2.46	0.8	0.75
192	0.26	0.39	50.3	105	2.14	2.10	0.72	0.72
387	0.08	0.50	76.8	120	1.49	1.77	0.66	0.62
778	0.025	0.63	127.0	140	1.10	1.70	—	0.47

Table 2. Measured Conditions Along Flooding Curve

Re	τ_i N/m²	T	−s	c cm/s	n	h_i cm
15	3.29	0.9778	44.1	35.3	11.4	0.017
25	3.28	0.9662	28.5	43.8	9.05	0.0215
43	3.32	0.9237	12.1	50.0	6.29	0.024
63	3.49	0.9041	9.4	58.2	5.31	0.026
78	3.25	0.8906	8.1	61.6	3.60	0.029
109	3.59	0.8722	6.8	56.0	3.20	0.030
189	3.80	0.8309	4.9	86.9	3.14	0.037
298	3.98	0.7702	3.35	96.36	2.56	0.042

varies like ϵ_1/ϵ_2, Figure 5. The trajectory disappears when it hits H_3, which is still a good approximation for substrate thickness.

This analysis of the general third-order equation showed again that n_H and H_3 are good approximations for wave velocity and substrate thickness, respectively, but that the wave shape differs from that of the second-order model.

Comparison with Experiments

Experimental data on wave structure on falling liquid films with counterflow of gas were recently presented by Zabaras and Dukler (1988). These data are used here to evaluate this model.

Free-falling film

Equation 47 with $s = 0$ can be used to determine n_H, the dimensionless wave velocity at the Hopf bifurcation, and this can be compared with the experimental values to test the conclusion of the phase space study that this must be close to the velocity of the homoclinic orbit and thus to experimental data. Similarly, Eq. 40 provides a value of H_3, the minimum possible film thickness computed from the theory. This can be used to compute the substrate thickness, which can be compared with the data. These comparisons with the data of Zabaras and Dukler (1988) appear in Table 1; surprisingly good agreement is displayed considering the difficulty in experimentally determining the substrate thickness. It should be noted that the Reynolds

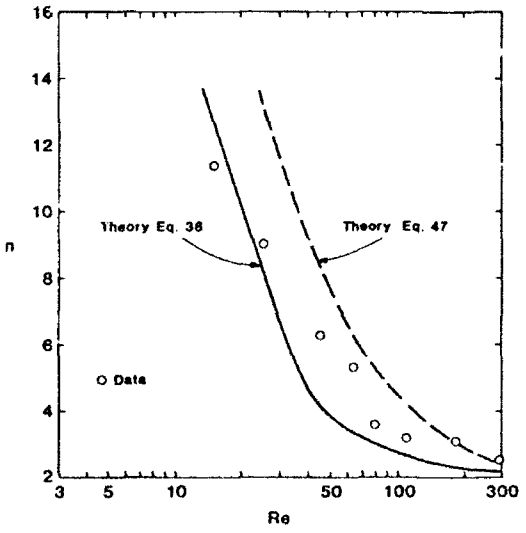

Figure 11. Theory-experiment comparison for wave velocity along flooding curve.

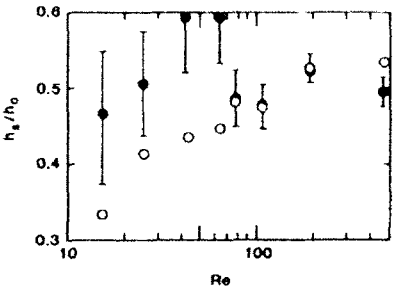

Figure 12. Theory-experiment comparison for substrate thickness along flooding curve.
o Theory; • Experiment

numbers in this work are defined as one-fourth those in the Zabaras and Dukler paper.

At Reynolds number above about 300 turbulent flow is thought to set in, the shape of the velocity profile changes, and the wave velocity would be expected to decrease, as discussed earlier.

Film with countershear

A severe test of the model is a comparison with data taken under the condition of interfacial shear due to counterflow of gas. Table 2 lists some original source data taken from the thesis of Zabaras (1985) during experiments along the flooding curve. Note that in accordance with theory the value of the dimensionless interfacial shear, T, is never less than -1. However at low liquid rates it approaches it closely. Figure 11 compares the experimental values of n with n_H calculated from the simple form of the equation in the limit $\beta \rightarrow 0$, Eq. 38, and from the general analysis, Eq. 47. The comparison is most encouraging, especially considering the fact that when $T \rightarrow -1$, the computed value of $s = T/(1 + T)$ used in both of these equations is extremely sensitive to small errors in T.

Not quite so satisfactory a comparison is shown in Figure 12. Here the dimensionless thickness calculated from Eq. 40 is compared with the dimensionless substrate thickness. The experimental values of s and n were used as input to these calculations. The error bars on the result due to the sensitivity of s to errors in T at the low flow rate is indicated. However it is still clear that the theory is not quite accurate enough in this region. We suspect this deviation is due to the assumption that the interfacial shear stress is independent of position along the interface and thus is the same over the substrate as it is over the wave itself. Experiments suggest that this is not the case and we are now exploring revised models which incorporate shear stress variation along the wave.

Acknowledgment

Financial support by the United States Office of Naval Research is gratefully acknowledged.

Notation

C_i = functions, Eq. 20
c = dimensional wave velocity
D = pipe diameter
f_0, f_1 = parameter in τ_i correlations, Eq. 58
f, g = functions, Eqs. 30, 43
h, H = dimensional, dimensionless film thickness
h_o, h_N = smooth film solution with, without shear
J = Jacobian matrix
l = dimensionless coordinate ξ/L
L = length scale $h_o Re/(1 + T)$
N = wave number
n = dimensionless wave velocity ch_o/Q_f
n_H, n_s = n of the Hopf and homoclinic saddle-loop bifurcations
P = pressure
Q, Q_f = local and feed liquid volumetric flow rate
Re = Reynolds number, Q/ν
s = modified shear parameter $T/(1 + T)$
T = dimensionless interfacial shear, $3\tau_i/2\rho g h_o$
t = time
U_G = linear gas velocity
u, φ = liquid velocity parallel, perpendicular to wall
w = dH/dl
W = surface tension parameter, Eq. 18
W_G, W_F = gas, liquid mass flow rate
x, y = coordinates in direction parallel, perpendicular to wall

Greek letters

α = exponent in power law profile, Eq. 21
β = ratio of time scales, Eq. 47
ν = kinematic viscosity
ρ = density
τ_i = shear at interface
σ = surface tension
η = dimensionless coordinate, y/h
μ = viscosity
θ, ξ = time, distance in a moving frame
ϵ_1, ϵ_2 = dimensionless time scales in terms H_{III}, H_{II}, defined following Eq. 43
ϕ = d^2H/dl^2
λ = eigenvalues of Jacobian matrix

Subscripts

x, y, H, etc. = derivative with respect to denoted quantities

Literature Cited

Alekseenko, S. V., V. Ye, Nakoryakov and B. G. Pokusaer, "Wave Formation on a Vertical Falling Liquid Film," *AIChE J.*, **31**, 1446 (Sept., 1985).

Bach, P., and J. Villadsen, "Simulation of the Vertical Flow of a Thin, Wavy Film Using a Finite-Elements Method," *Int. J. Heat Mass Transfer*, **27**, 815 (1984).

Benney, D. J., "Long Waves on Liquid Films," *J. Math Phys.*, **45**, 150 (1966).

Bharanthan, D., "Air-Water Countercurrent Annular Flow in Vertical Tubes," *Elec. Power Res. Inst. Rept.* EPRI NP-786 (1978).

Chang, H. C., "Nonlinear Waves on Liquid Film Surfaces. I: Flooding in a Vertical Tube," *Chem. Eng. Sci.*, **41**, 2463 (1536).

Chu, K., and A. E. Dukler, "Statistical Characteristics of Thin Wavy Films. III," *AIChE J.*, **21**, 583 (Aug., 1975).

Dukler, A. E., "The Wavy Gas Liquid Interface," *Chem. Eng. Educ.*, 108 (1976).

———, "The Role of Waves in Two-Phase Flow" ASEE Award Lecture, *Chem. Eng. Educ.*, 108 (1977).

Kapitza, P. L., and S. P. Kapitza, "Wave Flow of Thin Layers of a Viscous Fluid," *Zh. Exper. i Teor Fiz.*, **19**, 105 (1949); also in coll. papers of P. L. Kapitza, Macmillan, New York (1964).

Maron, D. M., and A. E. Dukler, "Flowing and Upward Film Flow in Tubes," *Int. J. Mult. Flow*, **10**, 599 (1984).

Maron, D., N. Brauner, and A. E. Dukler, "Interfacial Structure of Thin Falling Films: Piecewise Modeling of the Waves," *Physicochem. Hydrodyn.*, **6**, 87 (1985).

Needham, O. J., and J. H. Merkin, "On Roll Waves Down an Open Inclined Channel," *Proc. Roy. Soc. London*, **A394**, 259 (1984).

Pumir, A., P. Manneville, and Y. Pomeau, "On Solitary Waves Running Down an Inclined Plane," *J. Fluid Mech.*, **135**, 27 (1983).

Zabaras, G. J., "Studies of Vertical Cocurrent and Countercurrent Annular Gas-Liquid Flows," Ph.D. Thesis, Univ. Houston (1985).

Zabaras, G. J., and A. E. Dukler, "Countercurrent Gas-Liquid Annular Flow Including the Flooding State," *AIChE J.*, **34**, 389 (Mar. 1988).

Zabaras, G., A. E. Dukler, and D. M. Maron, "Vertical Upward Cocurrent Gas-Liquid Flow," *AIChE J.*, **32**, 829 (May, 1986).

Manuscript received May 16, 1988 and revision received Sept. 26, 1988.

Chemical Engineering Science, Vol. 47, No. 17/18, pp. 4323–4331, 1992
Printed in Great Britain

0009-2509/92 $5.00 + 0.00

AN EXPERIMENTAL STUDY OF MASS TRANSFER FROM A WALL INTO A WAVY FALLING FILM

FREDERIC K. WASDEN† and A. E. DUKLER‡
Department of Chemical Engineering, University of Houston, Houston, TX 77204, U.S.A.

(*First received* 3 *September* 1991; *accepted in revised form* 7 *January* 1992)

Abstract—Mass transfer from a solid boundary into a thin wavy film was studied for a wide range of laminar flow rates with a novel experimental technique. Speculations that large waves control the transport process through a convection mechanism are validated through an examination of the time variation of the film thickness and solute concentration. Statistical analyses of the data demonstrate that the occurrence of large waves with higher local flow rates coincides with an increased mass transfer both locally and globally. Accordingly, the relative importance of small waves or ripples is shown to decrease rapidly with increasing flow rate.

INTRODUCTION

As a liquid film flows down a solid surface, a wavy interface develops. For flow rates of industrial interest, the free surface quickly becomes covered with a complex array of waves whose amplitudes vary greatly about the mean film thickness. This gravity-driven behavior is observed even in the absence of interfacial shear stresses induced by adjacent gas flow. Figure 1 shows a sample time tracing of the interface of a fully developed laminar film falling freely down a vertical tube. Large waves, having amplitudes from 2 to 5 times the mean thickness, move over the thin substrate at velocities up to several times the mean and carry a large fraction of the total liquid flow. The slope of these large waves seldom exceeds 5%, yet numerical studies of the flow fields (Wasden and Dukler, 1989) show that significant normal velocities exist near the gas–liquid and wall interfaces.

Mass transfer in liquids is a slow process compared to heat transfer, suggesting that mass transfer rates respond more dramatically than heat transfer rates to wave-induced fluctuations in the otherwise parallel flow (cf. Seban and Faghri, 1978; Henstock and Hanratty, 1979). Many analytical studies of transport through flat or slightly rippled films exist, all treating the interface as a regular or periodic surface. For selected large waves, the convective fluxes due to normal velocities near the interfaces dominate the transport and partially explain why the previous analyses underpredicted the overall mass transfer rates (Wasden and Dukler, 1990).

Previous experimental studies of mass transfer into falling films have domonstrated that transfer rates in wavy films are greater than when waves are suppressed, without providing an insight into the mechanisms of enhancement. Gas absorption experiments are typically conducted by contacting the entire film surface with an excess of solute and measuring the bulk outlet concentration (Emmert and Pigford, 1954). This practice yields data averaged over all waves on the surface and makes it impossible to explore the effects of wave characteristics. An alternative arrangement to study wave effects on mass transfer is illustrated in Fig. 2. Solvent flows as a wavy film over a contaminated wall section, which may be located any distance below the solvent entrance. Large waves evolve slowly on the fully developed films; so if the film thickness and the average contaminant concentration are measured directly after the film contacts this section, the effects of wave shape, size, velocity, etc., on the mass transferred into the film should be plain. According to the criterion of Aris (1956), Taylor dispersion in this system is negligible. This configuration is similar to the one studied by Stirba and Hurt (1955) and offers several experimental advantages for studying the effect of waves. First, while the presence of waves causes interfacial transfer rates for gas absorption to be 2–4 times greater than those observed for smooth films (Henstock and Hanratty, 1979), mass transfer from the wall appears to occur 5–10 times faster than in smooth films (Stirba and Hurt, 1955). Second, it is possible to maintain precise control over the amount of contaminant entering the solvent, whereas gas absorption operations are limited to providing contaminant in excess. Third, the effects of wave amplitude and velocity may easily be studied by varying the distance between the film entry and the contaminated section.

Previous experimental studies of this type, which used the dissolution of a solid solute surface by the film (Stirba and Hut, 1955; Kramers and Kreyger, 1956; Oliver and Atherinos, 1968), measured mass transfer rates either by weighing the flow surfaces before and after an experiment or by measuring the bulk concentration of solute in the fluid leaving the apparatus. Such procedures made it impractical to explore the effects of wave characteristics. Simultaneous measurements of mass concentration and film

†Presently with Shell Development Company, Westhollow Research Center, Houston, Texas.
‡Author to whom correspondence should be addressed.

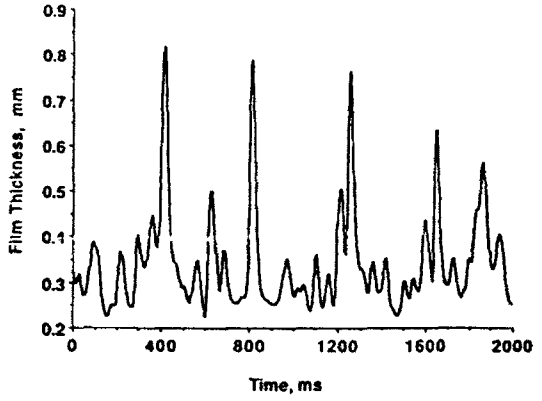

Fig. 1. Film thickness time trace, $Re = 880$.

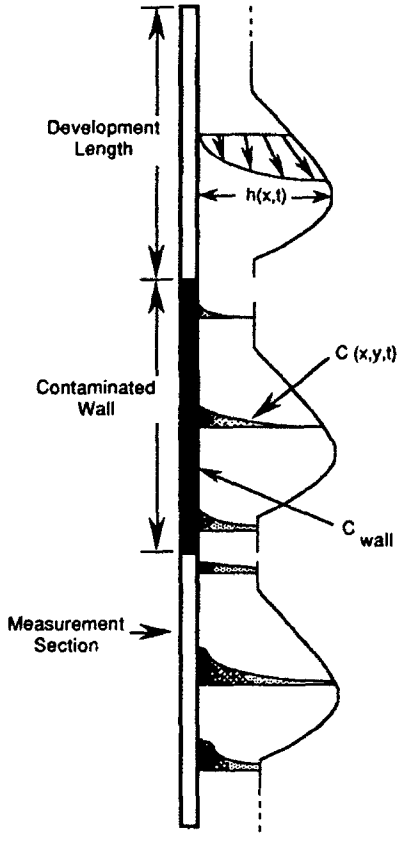

Fig. 2. Mass transfer from the solid boundary into a passing wave.

structure have not been reported for transfer from the wall into a film, but Stainthorp and Wild (1967) measured the film thickness and the concentration averaged over the film thickness in a thin-film liquid–liquid extraction column. Measurements were taken using two photocells located 38 mm apart in the flow direction and an absorbance technique was used to relate photocell readings to film thickness and concentration.

The analysis of mass transfer from the wall to a liquid is represented by a substantial body of literature due to the interest in using electrochemical probes with a redox reaction of measure wall shear stress in high Schmidt number fluids (see the review by Hanratty and Campbell, 1983). Under these conditions, the concentration boundary layer near the wall is exceedingly thin and the velocity profile is considered linear. For quasi-steady conditions a closed-form relation between mass transfer rate and wall shear stress can be derived. However, this method is of little use when the resistance to mass transfer extends through the film as in large waves.

Experimental studies have examined the average effects of waves on transport and numerical approaches have explored transport processes in isolated waves. Both avenues show the importance of wave characteristics and suggest the need for detailed simultaneous local measurements of film structure and concentration. The work presented here includes the description of a novel method to obtain these measurements and an analysis of the laminar film flow results.

EXPERIMENTAL APPARATUS, TECHNIQUE AND PROCEDURE

Flow loop and measuring station

The flow loop is illustrated in Fig. 3. Solvent enters the top of the vertical column through a stainless steel porous sinter which distributes the inlet flow smoothly and uniformly around the tube periphery. Solute is pumped through the pores of a very smooth plastic cylindrical insert located directly above the measuring station. The column is constructed of a number of precisely machined segments of Plexiglas tubing with 50.8 ± 0.2 mm ID. The flow development distance is adjusted by varying the number of segments between the solvent feed and solute input sections. Solvent (an aqueous salt solution) and solute (an aqueous salt and dye solution) were pumped into the system using magnetically coupled gear pumps. The pump drive units contain an internal feedback circuit to maintain constant flow rates with minimal fluid heating. Details of the solvent feed section, pumps and flow loop construction are found elsewhere (Wasden, 1989).

The solute feed section was designed to uniformly distribute a very low flow rate of contaminant both axially and circumferentially so that the section approximates a contaminated solid wall. This arrangement was developed to avoid previously reported difficulties in wetting a solid contaminant surface (Stirba and Hurt, 1955; Kramers and Kreyger, 1956; Oliver and Atherinos, 1968). As shown in Fig. 4, the section is made of an extruded piece of porous polyethylene whose surfaces are very smooth. Surface pore sizes average 10 μm and solute is constantly pumped at very low rates from the annulus through the pores into the solvent stream. The porous plastic ID was slightly larger than the Plexiglas tube ID, so the

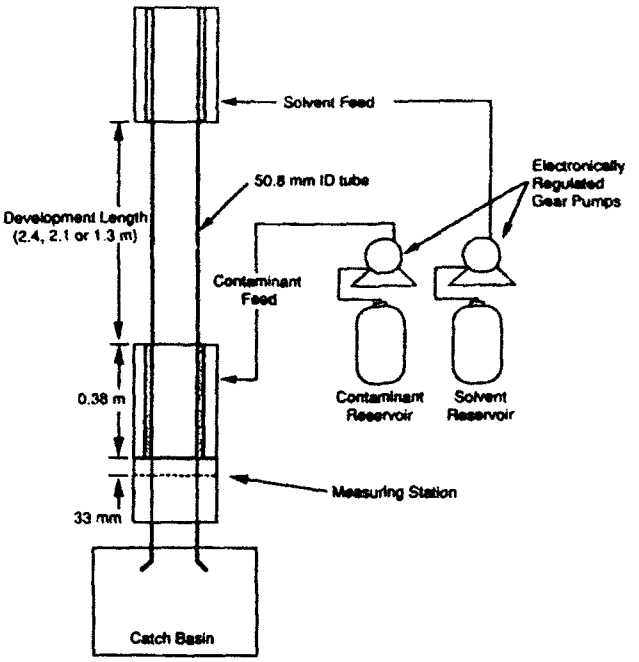

Fig. 3. Experimental flow loop.

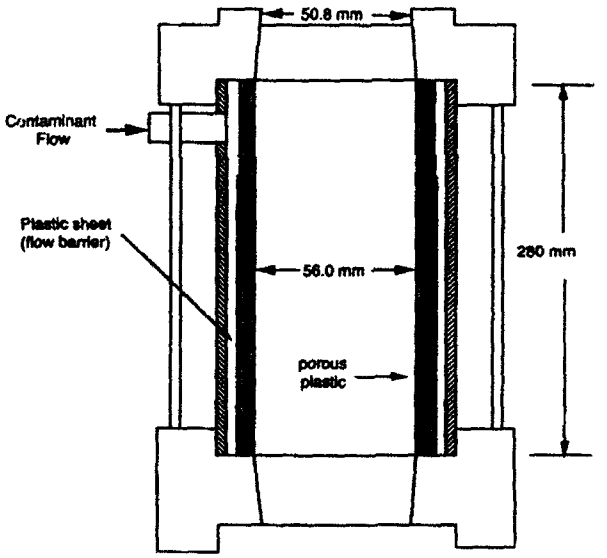

Fig. 4. Contaminant feed section of flow loop.

flanges connecting the 280 mm long porous section to the column were smoothly tapered at a 2.9° angle. Uniform wetting of the surface was achieved by blocking a large portion of the back side of the porous plastic. Fluid enters the solute section through the uncovered portion of the outer surface. Once past this barrier, hydrostatic and pump pressure equalize the fluid distribution in the highly porous central region and force it to the inner wall, where it uniformly saturates the small pores. By adjusting the area closed to flow on the outside of the porous section, fluid was observed to be distributed evenly both axially and circumferentially over the lower 255 mm of the device.

The measuring station (Fig. 5) included provisions for measuring the film thickness at two axial locations and the average concentration at the upper film thickness location. The device was constructed from a piece of Plexiglas bored to 50.8 mm in which two sets of parallel 76 μm diameter Ni–Pt wires axially separated by 25.0 mm were installed to measure the film thickness. A set of collinear quartz rods with highly polished ends was used to transmit a laser light beam

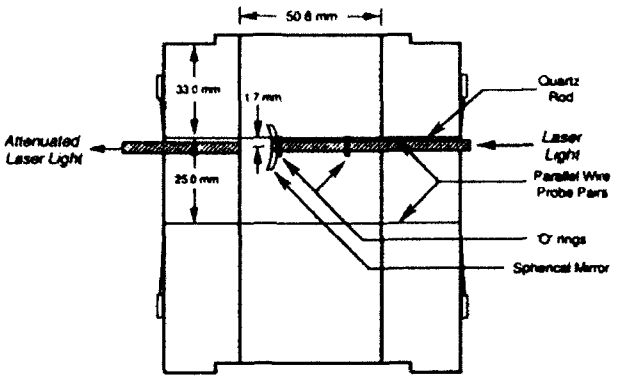

Fig. 5. Wave structure and contaminant-measuring section.

through the contaminated film. The center of the receiving rod was mounted flush with the wall, between and 1.7 mm below the top wires. The transmitting rod penetrated the film on the opposite side of the tube. One end of this rod was positioned so that it was 12.5 mm from the receiving rod end. In order to minimize reflective losses from the liquid surface, 12.5 mm diameter parabolic mirror with a 12.5 mm focal length was placed over the rod end. A pair of 100 μm holes drilled above the central mounting hole permitted the parallel conductance wires to pass through. A set of "O" rings was placed on the outside of the penetrating rod to keep liquid from migrating from the film onto the rod end and obscuring the light path.

Measurement techniques and instrumentation

Two experimental techniques were combined in this study. A high-frequency circuit was used to relate the conductance of the liquid between the parallel wires to the film thickness. The resolution of the method is of the order of 15 μm and the circuit had a time lag of less than 100 μs (Brown *et al.*, 1978). The average concentration was determined by measuring the attenuation of a laser light beam passing through the contaminated film while simultaneously measuring the film thickness with the parallel-wire conductance method. The relation between optical attenuation and solute concentration invokes Beer's law for monochromatic radiation (Knowles and Burgess, 1984). For a single contaminant,

$$A = \varepsilon h \langle C \rangle \tag{1}$$

where A is the optical absorption of the contaminated solution, ε, the molar absorptivity of the contaminant at the particular wavelength, h, the path length of the radiation and $\langle C \rangle$, the average concentration of the contaminant over the path length. The absorption can be related to the incident and transmitted radiation through

$$A = \ln (I_0/I) = \ln (1/T_\lambda) \tag{2}$$

where I_0 is the intensity of the incident beam, I, the attenuated intensity and T_λ, the transmittance of the medium for the wavelength of interest. An optically dense dye solution was used as the contaminant. By using a transparent aqueous salt solution as the solvent, the attenuation of light indicates only the amount of solute in the optical path.

A schematic of the optical measurement system is shown in Fig. 6. The light source was a 5 mW He–Ne laser (632.8 nm) concentrated into a 0.8 mm diameter beam and rated at less than 0.1% RMS noise. A 6" diameter integrating sphere was used to capture light leaving the quartz rod and provide a uniform luminous flux on the face of a photodetector mounted 90°

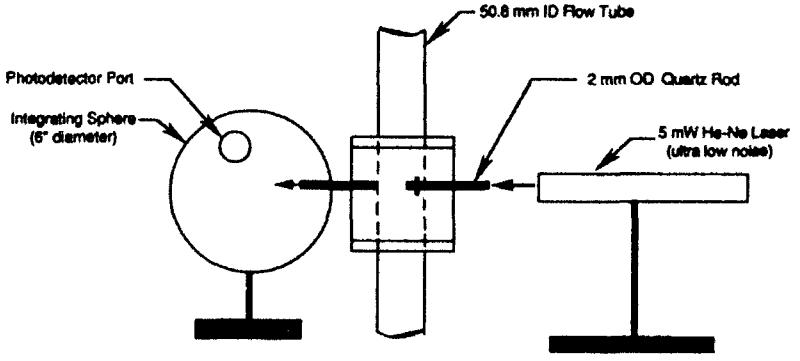

Fig. 6. Optical measurement system.

off-axis of the incoming beam. This arrangement insured that the output of the photodetector was not influenced by the alignment of the photodetector face with respect to the quartz rod. The photodetector current indicates the light transmitted and is expressed as

$$T_\lambda = \exp(-A) = \exp(-\epsilon h\langle C\rangle) \approx 1 - \epsilon h\langle C\rangle \cdots \quad (3)$$

for small values of absorption. The value of $\langle C\rangle$ was determined once h was obtained from the parallel wire probes. Dye concentrations were chosen so that the transmittance was always greater than 95% and the linear approximation [eq. (3)] was accurate to within 0.1%. Analog data collected from the film thickness probes and photodetector circuitry were digitized and subsequently processed. All signals were digitized at a frequency of 1 kHz per channel with a 12-bit analog–digital converter installed in a microcomputer.

Solvent and solute properties

The solvent was a 0.34 M aqueous solution of NaCl with 0.04 $g\,l^{-1}$ dye. The dye used was toluidine blue (Basic Blue 17) which has a peak in its absorption spectra at 628 nm. The molar absorptivity of the dye (ϵ) at 630 nm is quoted as 5000 $M^{-1}\,cm^{-1}$. This highly absorbing dye was chosen so that a very small concentration could be detected. An aqueous solution of 5 $g\,l^{-1}$ dye and 0.34 M NaCl was used as the solute. The solute dye concentration was kept low to insure that the physical properties of the solution were not appreciably altered by its presence. At 22°C the solvent had the following measured properties: density, 1010 $kg\,m^{-3}$, absolute viscosity, 9.845×10^{-4} $kg\,m^{-1}s^{-1}$ and surface tension coefficient, 74.2×10^{-3} $N\,m^{-1}$. The diffusion coefficient for the concentrated organic dye diffusing into a slightly contaminated solvent was estimated to be 2.8×10^{-10} $m^2\,s^{-1}$ (Cussler, 1984). Over the course of the experiments no deviations greater than 0.2°C were noted and fluid properties were considered constant.

Calibration, verification of measurement techniques and procedure

Errors in film thickness measurements were estimated to be no more than 1%. The error in the concentration averaged over the film thickness was shown to be less than 2.5%. Environmental noise in the optical signal was eliminated by covering the entire apparatus in thick black plastic sheeting and losses in the optical arrangement were accounted for in the calibration procedure. The accuracy of the method can be confirmed by examining data obtained for the flow of pure solvent with a uniform dye concentration. The optical signal is converted to the film thickness for a known dye concentration using eq. (3). Figure 7 shows a typical film thickness trace obtained using the conductance method at a Reynolds number of 750. Optical measurements were made simultaneously and the relative deviation between conductance and optical measurements are shown in the figure. The agreement proves that the sensitivity of the optical technique is sufficient to resolve deviations in local dye concentrations of the order of 1% of the solvent or 0.008% of the solute concentration. The agreement also shows that the frequency responses of the instruments are comparable and, thus, can measure small waves.

Each experimental run was preceded by calibration of the system, the procedures for which are described elsewhere (Wasden, 1989). Solute flow rates of roughly 2% of the solvent flow rate were found to provide adequate contaminant without disrupting the flow. Data were collected for solvent flow rates corresponding to Reynolds numbers between 100 and 1000. Each

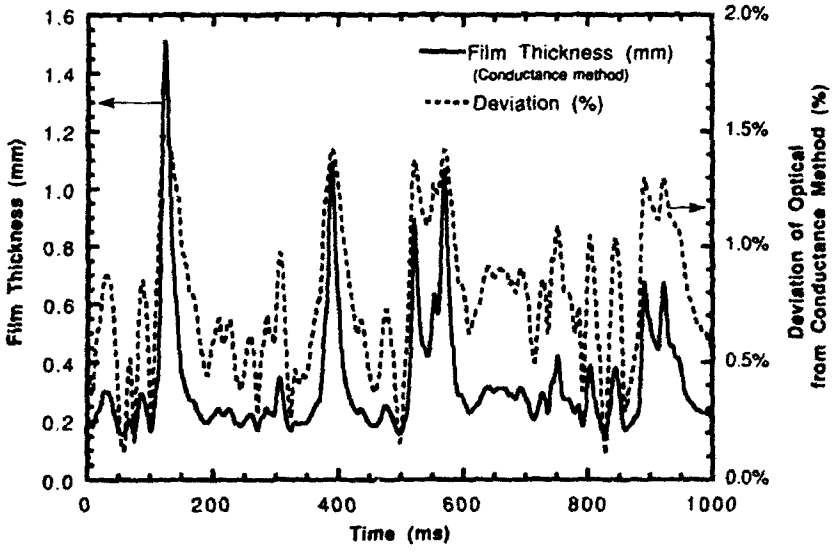

Fig. 7. Film thickness and deviations between optical- and conductance-based measurements, $Re = 750$.

solvent–solute flow rate condition was sampled for 90 s, allowing 500–1000 large waves to pass the measuring station.

DATA ANALYSIS AND DISCUSSION OF RESULTS

Time series of film thickness and the average dye concentration were examined to test the speculation that large waves dominate the transport dynamics. Since dye concentration was measured 1.7 mm below the film thickness, cross correlations of the film thickness signals were computed and used to extract a time delay for time-shifting the concentration signal to approximate simultaneous measurements. The degree of mixing was inferred from a solute distribution coefficient

$$\phi(t) = \frac{1}{C_{wall} h_N} \int_{y=0}^{y=h(t)} C(y,t)\,dy. \qquad (4)$$

The coefficient would be identical in shape to the film thickness for a perfectly mixed film. Conversely, if no mixing occurs (as in a flat film), $\phi(t)$ is constant.

Typical time-dependent measurements of the film thickness and the solute distribution coefficient, ϕ, appear in Figs 8 and 9 for Reynolds numbers of 230, where the large waves are only weakly developed, and

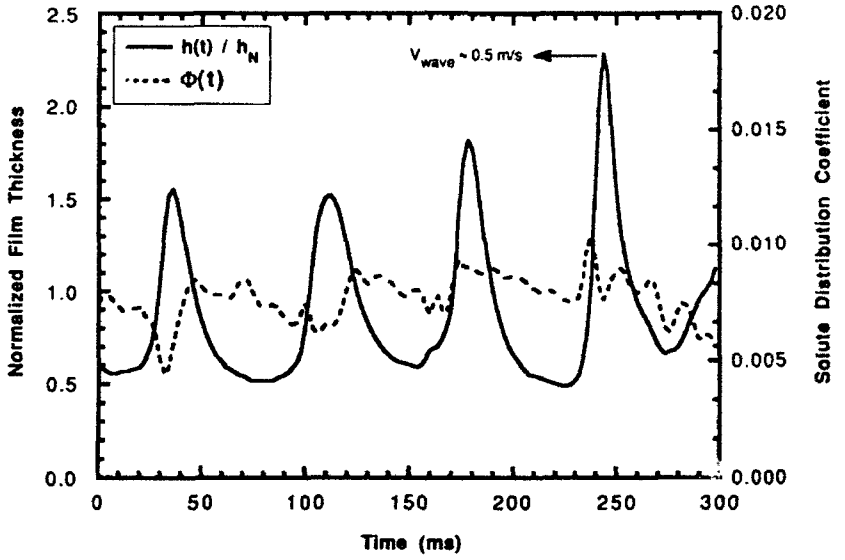

Fig. 8. Film thickness and solute distribution coefficient for a film development length of 2.14 m, $Re = 230$.

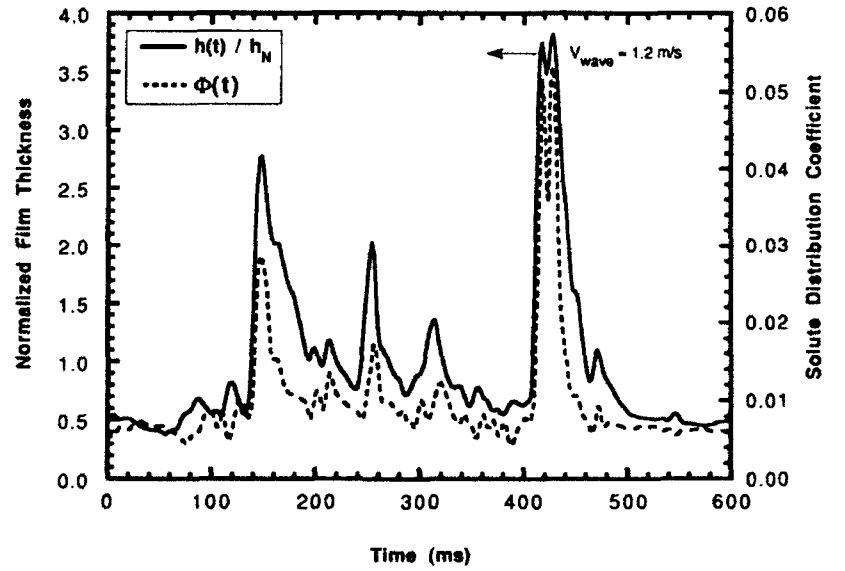

Fig. 9. Film thickness and solute distribution coefficient for a film development length of 2.14 m, $Re = 950$.

950, where they dominate the interface. Film thicknesses are normalized by h_N, the film thickness computed for a laminar film without waves. At low Reynolds numbers the ratio of the wave peak to substrate thickness is as much as four but at $Re = 950$ wave peak to substrate thickness ratios of the large waves range from four to eight. At the higher flow rate the waves are asymmetrical in shape. Wasden and Dukler (1989) computed the flow field for such waves and showed that for large asymmetric waves there exist significant velocities normal to the wall at the front and back of the wave. In addition, there is present a region of fluid recirculation under the wave when viewed in a coordinate system moving with the wave. Thus, in the presence of large waves the convection and circulation are expected to significantly enhance the mass transfer rate.

At $Re = 230$, Fig. 8 illustrates the effect of the wave motion even when the waves are not large. In general, peaks in the values of ϕ appear near the front and back of the wave. When the wave is asymmetric there is a sharp decrease in ϕ below the peak of the wave, indicative of a low concentration in the recirculation region. By contrast, the large waves associated with the higher flow rate in Fig. 9 all show large peaks in the solute distribution coefficient in the front region of the wave. The amount of mass captured by these large waves (proportional to ϕ) is 2–5 times larger than that

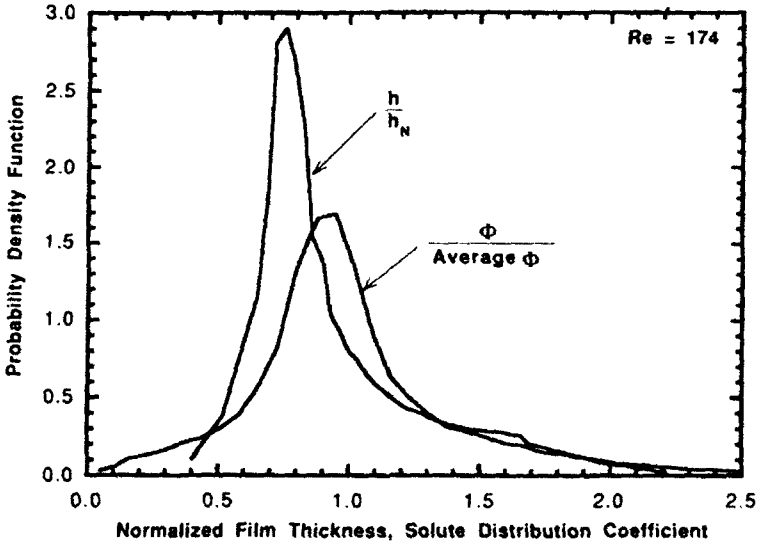

Fig. 10. Probability density functions of normalized film thickness and solute distribution coefficient for $Re = 174$ and a development length of 1.3 m.

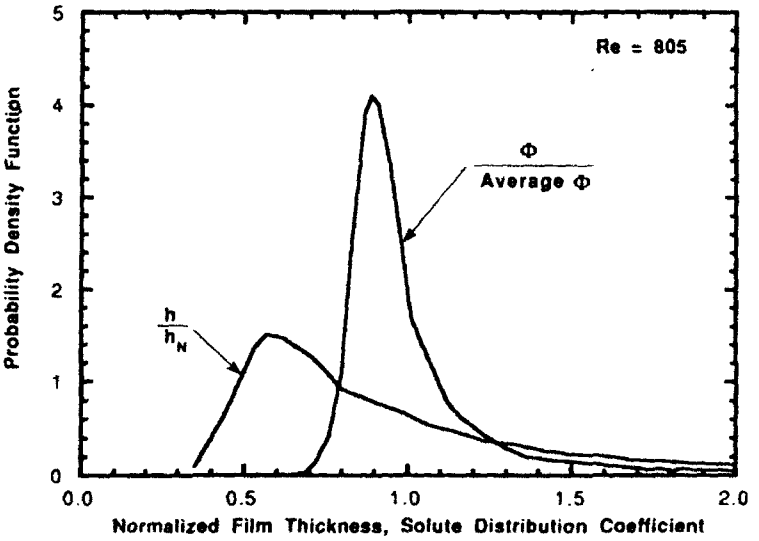

Fig. 11. Probability density functions of normalized film thickness and solute distribution coefficient for $Re = 805$ and a development length of 2.4 m.

for the small-wave system. These data seem to support the qualitative argument that the large waves control the mass transfer process because of the large secondary convections induced by these waves.

Standard techniques were used to compute the probability distributions of h and ϕ (Bendat and Piersol, 1971) and their spectra (Priestley, 1987). Figures 10 and 11 compare the pdfs for high and low Reynolds numbers. The large tail in the distribution of film thickness for $Re = 805$ reflects the presence of large waves. The shift in the probability distribution of ϕ to the region of the larger waves shows again that these waves of larger amplitude control the mass transfer process.

Figures 12 and 13 show the auto spectra of h and ϕ and the coherence function between the two for the two Reynolds numbers. The coherence function in the frequency domain is the analog of the cross-correlation function in the time domain. For these computations the Bartlett–Priestley spectral window was used with a frequency resolution 0.48 Hz. The sample size was such that the standard random error of 12% of the spectrum can be expected at any frequency.

At $Re = 174$ (Fig. 12), the spectrum of the film thickness peaks at about 8 Hz; however, considerable energy is displayed due to the smaller waves at higher frequencies. The spectrum of F is quite flat, suggesting contributions to transfer from the full range of wave

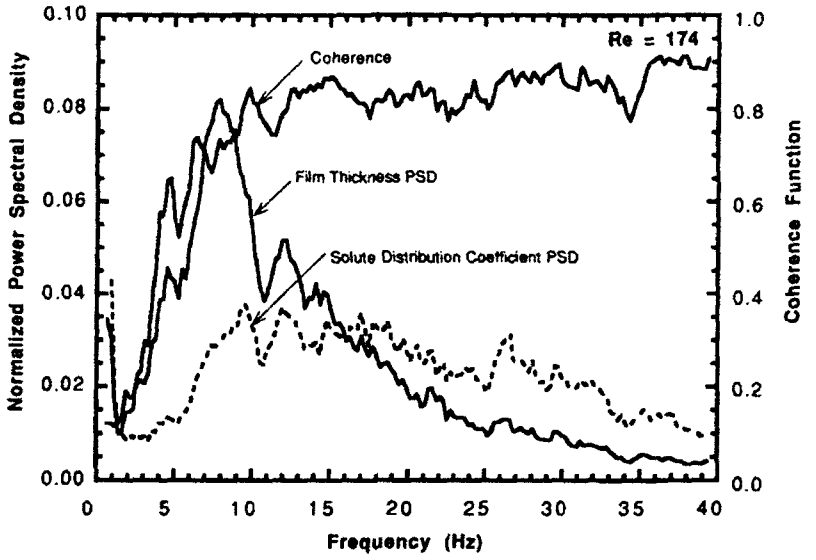

Fig. 12. Power spectral density and coherence functions of normalized film thickness and solute distribution coefficient for $Re = 174$ and a development length of 1.3 m.

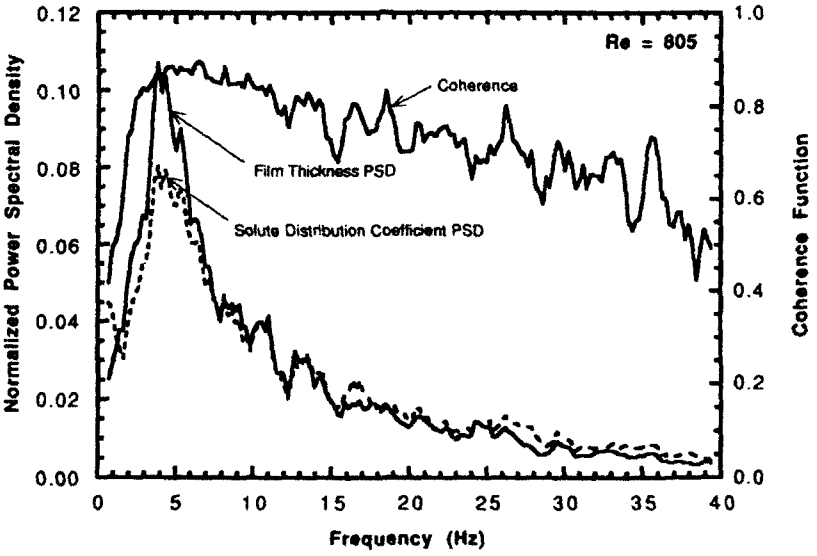

Fig. 13. Power spectral density and coherence functions of normalized film thickness and solute distribution coefficient for $Re = 805$ and a development length of 2.4 m.

frequencies. However, Fig. 13 shows that at $Re = 805$ the dominant frequencies for both the wave motion and the mass transfer overlap in the range of the large-wave frequencies with a much smaller amount of spectral energy in the region associated with the small waves. Again, this suggests that at higher flow rates the large waves dominate the process of mass transfer.

SUMMARY AND CONCLUSIONS

Falling liquid films are covered with a random array of small and large waves interacting in a complex fashion. The experimental technique developed for this study measured the instantaneous local solute concentration averaged over the thickness of the liquid film, simultaneously with a measurement of the local film thickness. Data were collected over a range of Reynolds numbers and development lengths. An analysis of these data revealed that the large waves control the rate of transfer to the film. This result is consistent with recent theoretical studies, which indicate convective circulation paths which exist under the large waves.

Acknowledgements—Financial support of this research by the Office of Naval Research is gratefully acknowledged. One of the authors (FKW) was supported by a National Science Foundation Graduate Fellowship.

NOTATION

A	optical absorption of contaminated solution
C	local contaminant concentration, kg m^{-3}
$\langle C \rangle$	contaminant concentration averaged from the wall to the interface, kg m^{-3}
D	molecular diffusion coefficient, m^2 s^{-1}
g	acceleration due to gravity, m s^{-2}
h	local film thickness, mm
h_N	Nusselt film thickness $(= 3/4\ Re\ \nu^2/g)^{1/3}$
I	intensity of radiation, W m^{-2}
Pe	Peclet number $(= Re\,Sc)$
Q	liquid-film flow rate per unit perimeter, m^2 s^{-1}
Re	film Reynolds number $(= 4Q/\nu)$
Sc	Schmidt number $(= \nu/D)$
T_λ	transmittance of solution at a wavelength λ
u	local streamwise velocity, m^{-1}
v	local velocity normal to the boundary, m^{-1}
V_w	wave velocity, m s^{-1}
x	axial coordinate in lab frame, m
y	coordinate normal to the boundary, m

Greek letters

ε	molar absorptivity of contaminant, m^4 kg^{-1}
μ	liquid absolute viscosity, kg m^{-1} s^{-1}
ν	liquid kinematic viscosity, m^2 s^{-1}
ρ	liquid density, kg m^{-3}
τ_w	wall shear stress, N m^{-2}
ϕ	solute distribution coefficient as defined in eq. (4)

REFERENCES

Aris, R., 1956, On the dispersion of a solute in a fluid flowing through a tube. *Proc. R. Soc.* **A235**, 67–78.

Bendat, J. S. and Piersol, A. G., 1971, *Random Data: Analysis and Measurement Procedures*. Wiley-Interscience, New York.

Brown, R. C., Andreussi, P. and Zanelli, S., 1978, The use of wire probes for the measurement of liquid film thickness in annular gas–liquid flows. *Can. J. chem. Engng* **56**, 754–758.

Cussler, E. L., 1984, *Diffusion: Mass Transfer in Fluid Systems*. Cambridge University Press, New York.

Dukler, A. E., 1977, The role of waves in two phase flow: some new understanding. *Chem. Engng Educ.* 1976 Award Lecture, 108–138.

Emmert, R. E. and Pigford, R. L., 1954, A study of gas absorption in falling liquid films. *Chem. Engng Prog.* **50**, 87–93.

Hanratty, T. J. and Campbell, J. A., 1983, Measurement of wall shear stress, in *Fluid Mechanics Measurement* (Edited by R. J. Goldstein). Hemisphere, Washington, DC.

Henstock, W. H. and Hanratty, T. J., 1979, Gas absorption by a liquid layer flowing on the wall of a pipe. *A.I.Ch.E. J.* **25**, 122–131.

Kapitza, P. L. and Kapitza, S. P., 1949, Wave flow in thin layers of a viscous fluid. *Zh. Exper. i Teor Fiz.* **19**, 105; also in *Collected Papers of P. L. Kapitza, Vol.* II. Macmillan, New York, 1964.

Kramers, H. and Kreyger, P. J., 1956, Mass transfer between a flat surface and a falling liquid film. *Chem. Engng Sci.* **6**, 42–48.

Oliver, D. R. and Atherinos, T. E., 1968, Mass transfer to liquid films on an inclined plane. *Chem. Engng Sci.* **23**, 525–536.

Priestley, M. B., 1987, *Spectral Analysis and Time Series. Volume* 1: *Univariate Series*. Academic Press, London.

Seban, R. A. and Faghri, A., 1978, Wave effects on the transport to falling laminar liquid films. *J. Heat Transfer* **100**, 143–147.

Stainthorp, F. P. and Wild, G. J., 1967, Film flow—the simultaneous measurement of wave amplitude and the local mean concentration of a transferable component. *Chem. Engng Sci.* **22**, 701–704.

Stirba, C. and Hurt, D. M., 1955, Turbulence in falling liquid films. *A.I.Ch.E. J.* **1**, 178–184.

Wasden, F. K., 1989, Studies of mass and momentum transfer in free falling wavy films. Ph.D. dissertation, University of Houston, Houston, TX.

Wasden, F. K. and Dukler, A. E., 1989, Insights into the hydrodynamics of free falling wavy films. *A.I.Ch.E. J.* **35**, 187–195.

Wasden, F. K. and Dukler, A. E., 1990, A numerical study of mass transfer in free falling wavy films. *A.I.Ch.E. J.* **36**, 1379–1390.

Int. J. Multiphase Flow Vol. 15, No. 3, pp. 357–370, 1989
Printed in Great Britain.

0301-9322/89 $3.00 + 0.00

NUMERICAL INVESTIGATION OF LARGE WAVE INTERACTIONS ON FREE FALLING FILMS

F. K. WASDEN and A. E. DUKLER
Department of Chemical Engineering, University of Houston, Houston, TX 77204, U.S.A.

(*Received* 21 *October* 1988; *in revised form* 15 *November* 1988)

Abstract—From experimental measurements of a free falling liquid film at Re = 880, four representative large, evolving or interacting waves were selected for computational domains in which the Navier–Stokes equations were numerically solved. The algorithm computed velocity and pressure fields within each wave, as well as the shape necessary to match experimental wall shear stress data. Results show interaction effects significantly modify flow fields, compared to large solitary waves. Waves having two peaks had two closed recirculation regions, with a mixing layer separating them. The size of the recirculation regions was dependent on the extent of separation of the wave peaks. As with solitary waves, strong streamwise accelerations exist, with both location and magnitude varying with shape and evolutionary character of the wave. Heat and mass transfer rates must be enhanced by these flow properties, which are shown to have a complicated dependence on wave structure. Examination of the flow fields suggests parabolic streamwise velocity profiles are generally deficient, explaining shortcomings experienced by hydrodynamic models based on such simple velocity profiles.

Key Words: falling liquid films, numerical methods

INTRODUCTION

Investigations of hydrodynamic and transport properties of thin falling liquid films remain a fertile research area today. Thin liquid films are encountered in a wide variety of industrial process equipment, including wetted wall absorbers, falling film chemical reactors, condensers and vertical tube evaporators. At flowrates of industrial interest, falling films (even in the absence of gas flow) evolve to a highly irregular wavy interface which is generally considered quasi-stationary. Figure 1 displays a short time trace of such a falling film, 10,000 mean film thicknesses below the inlet. The film surface is covered by a complex array of large and small waves moving over a substrate which is less than the mean film thickness. The large waves, ranging in amplitude from 2 to 5 times the substrate thickness, carry a large fraction of the total mass flowing, and are speculated to control the rates of scalar transport (Dukler 1977). Before the heat or mass transfer rates to such films can be modeled it is necessary to understand the velocity distributions which exist within these waves, as well as the evolution of the interface. The present work focuses on these questions.

Previous modeling efforts generally were limited to either single, non-interacting (solitary) waves of various thicknesses, or the intersection of small waves. While large, solitary waves and small ripples on the substrate symbolize asymptotic behavior of the flow, examination of film thickness measurements, as in figure 1, shows these limiting cases are not representative of the flow. Numerical simulation of the isolated, large waves at the flow conditions of figure 1 (Wasden & Dukler 1989) suggests transport through the film is enhanced by the interaction of large wave peaks with the relatively slowly moving substrate. This same study determined that the seemingly slow evolution of these waves is responsible for significant deviations in the flow field from those determined for solitary waves. The more complicated case of rapidly evolving or interacting waves integrates large wave interactions with the surrounding substrate and the potentially more important effects of wave interactions.

Evolution of the large waves far from the inlet may be regarded as processes of coalescence or splitting, and result from some type of flow instability. Large waves do not grow without limit, but split into daughter waves when sufficiently perturbed. Many large waves overrun smaller, slower moving waves, sometimes incorporating the smaller wave, while often passing over them

without significant mass addition. The wide array of large wave behavior illustrates the need for local measurements to determine relative effects of wave evolution and large wave induced convection on transport enhancement.

Reliable experimental measurements of the velocity distribution in the films is exceedingly difficult due to the extremely small film thickness (≈ 1 mm), very short passage time of each wave (≈ 60 ms) and the random location of the interface, as shown in figure 1. Non-intrusive methods, such as LDA, do not provide sufficiently fine resolution to investigate velocity profiles. Thus, experimental measurements of hydrodynamic variables appear limited to the time variation of wall shear stress and film thickness. Correspondingly, analytical models have been developed in the absence of hard data on the true flow conditions which appear to exist in the waves.

Most analytical models of both single and interacting waves extend the concepts advanced by Kapitza (1964), based on the use of a parabolic velocity profile and assuming that the streamwise hydrodynamic variables scale with the wavelength. In 1972, in examining various models developed to that date, Dukler concluded that all failed to accurately represent any measured characteristics of the wave except at Reynolds numbers well below those of industrial interest.

Modeling the wavy film flow by a direct solution of the Navier–Stokes equations is hampered by numerical stiffness imposed by the stress-free interface; as a result, convergence is difficult except at the lowest flowrates. Previous numerical modeling has focused solely on non-interacting large waves. Bach & Villadsen (1984) explored the application of a finite element scheme to the unsteady problem of solitary waves developing from initial perturbations on the smooth film for Reynolds numbers up to 100. The film Reynolds number is defined as $\mathrm{Re} = 4\,Q/\nu$, where Q is the mass flowrate per unit perimeter and ν is the kinematic fluid viscosity. Their work predicted that the flow far from the inlet would consist of solitary waves having one general shape, a condition contrary to experimental fact even at film Reynolds numbers as low as 1. Kheshgi & Scriven (1987) applied a finite element technique to a problem with periodic boundary conditions in the flow direction, and verified the evolution of infinitesimal disturbances as predicted by Orr-Sommerfeld analyses. Their work was limited to low flowrates, and failed to generate waveforms comparable to those observed experimentally for fully-developed flow.

Recent simulations of solitary waves at a high Reynolds number (880) proceeded by solving the Navier–Stokes equations in a partially determined flow domain (Wasden & Dukler 1989). This work showed that isolated wave velocity is strongly dependent on wave shape, and provided evidence that numerous streamwise length scales existed in the flow. Further, it was determined that effects of wave evolution are important near the solid boundary, shifting the maximum wall shear stress in front of the film thickness peak. The use of a parabolic streamwise velocity profile to describe the flow in large waves was shown to be inappropriate over a large portion of these waves, suggesting analytical models based on such velocity profiles are fundamentally inadequate.

At present, no suitable models for evolving waves exist. In the absence of such models, and experimental methods for measuring velocity profiles in thin wavy films, a series of numerical experiments was performed. The experiments propose to illuminate the subject of transport

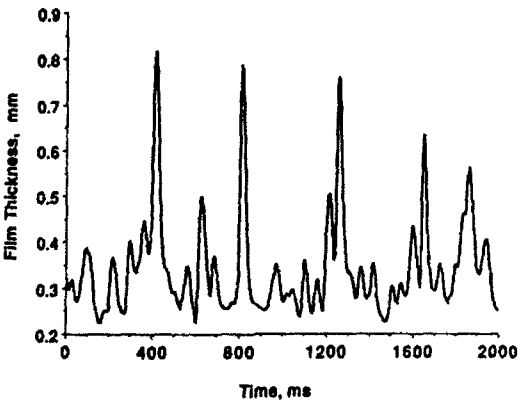

Figure 1. Film thickness time trace: Re = 880.

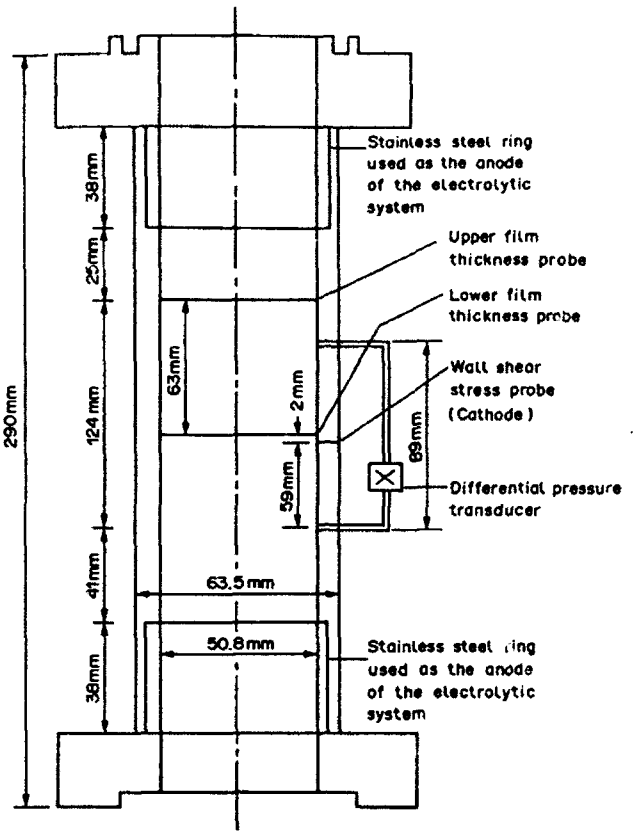

Figure 2. Measuring station.

enhancement due to waves by solving for the hydrodynamics within typical experimentally determined waveforms. For a film Reynolds number of 880, wave shapes and wall shear stress data were measured in our laboratory. Four representative large, interacting or evolving waveforms were converted for use as domains for a finite-difference code developed specifically for free surface problems. The use of experimentally measured waveforms is a novel concept, providing a somewhat simpler numerical task while insuring the results will not represent isolated or idealized cases of film flow. The results of these computations demonstrate the transport enhancement properties peculiar to evolving large waves, and present data useful for future model development.

EXPERIMENTAL PROCEDURE

Flow loop

For fully-developed wavy film flow, film thickness and wall shear stress data were collected in a 50.8 mm i.d. vertical test section in a flow loop described by Zabaras *et al.* (1986). After being pumped through a calibrated rotameter, the fluid entered the column through an annulus whose inner wall consists of a stainless steel porous sinter, having 100 μm pore size. Combined with careful leveling of the column prior to data collection, this entry section ensured minimal deviations from axisymmetric flow, and produced a smooth inlet flow. The measuring station was located 3.1 m (roughly 10,000 mean film thicknesses) below this entry section.

Measuring station and measurement techniques

The measuring station, shown in figure 2, is patterned after that described by Zabaras *et al.* (1986). The removable section allows simultaneous measurement of film thickness and wall shear stress at one location, as well as film thickness at another. The station was constructed of the same material as the flow loop, and was carefully machined to ensure a smooth transition to the station.

Film thickness probes consisted of twin parallel platinum–13% rhodium wires, 0.05 mm dia spaced 2.5 mm apart, which penetrated the flow. Described in detail by Brown *et al.* (1978), a linear relation exists between the resistance of the film between the wires and the film thickness. Calibration proceeded by setting the measuring station horizontal, blocking the ends and introducing different fluid levels, determined to within 10 μm using a cathetometer, followed by measurement of the resulting resistance. Downstream electronics for converting this resistance to a d.c. voltage signal are described elsewhere (Zabaras *et al.* 1986). Conductance of the fluid was monitored closely at all times during the calibration and data collection procedures to insure proper correction of any thermally induced conductance drift.

Wall shear stress measurements were based on the electrochemical mass transfer method described by Hanratty & Campbell (1983). For the present series of measurements, the iodine/tri-iodide system was chosen. The working solution contained 0.1 M KI and 0.004 M I_2(s) in demineralized water, and was replaced every 2 h to minimize errors due to iodine evaporation. A dry nitrogen atmosphere was used in the flow loop to minimize oxygen saturation of the solution. Fluid properties at 25 °C are: density, 1010 kg/m^3; absolute viscosity, 8.5×10^{-4} kg/m s; and surface tension, 7.12×10^{-2} N/m. The cathode for this system consists of a flush-mounted strip of platinum foil, 0.075 mm (in the flow direction) × 1 mm wide, embedded in Plexiglas to insure electrical isolation. By measuring the current produced by an electrochemical reaction at the surface of the cathode, the wall shear stress at that location is determined. For the redox reaction

$$I_3^- + 2e \rightarrow 3I^- \text{ (cathode)},$$

$$3I^- \rightarrow I_3^- + 2e \text{ (anode)},$$

a concentration boundary layer develops on the cathode surface, which is polarized at −0.8 VDC to insure the concentration approaches zero. For the iodine system, the range of polarization voltage is quite broad, insuring large increases in flowrate will not deplete the electron source at the cathode. Details concerning the downstream electronics and calibration associated with this measurement technique are to be found elsewhere (Zabaras *et al.* 1986).

It is now recognized (Mao & Hanratty 1985) that the response of the electrochemical probe is highly dependent of the nature of the "input" wall shear stress. For the ionic system employed in this study, errors in both phase and magnitude are expected to be small due to the large (10^3 s^{-1}) mean velocity gradient, small cathode surface area and large Schmidt number (ν/D) of the fluid (≈ 780). The relationship given by Hanratty & Campbell (1983) between cathode current and wall shear stress was used in this study, as the frequencies in the data were sufficiently low to allow the use of a quasi-steady analysis.

Data collection, processing and analysis

Voltage signals from two film thickness probes and the wall shear stress probe were first low-pass filtered at 1 kHz, then fed to a microcomputer-based A/D converter. Each signal was digitized at 1 kHz by a data translation 12-bit A/D converter installed in a DEC Micro 11/73 microcomputer. The data set comprised 1 min of data, and was stored on the system Winchester disc prior to applying calibration curves and writing the data to magnetic tape for further analysis. Digitization and collection errors are expected to be negligible for all data, while calibration errors for the film thickness measurement are expected to be <3%. Errors innerent in applying steady-state wall shear stress calibration curves depend on the nature of the input signal, requiring separate examination of individual results. Zabaras (1985) reports estimated errors of <7% for this technique.

Film thickness and wall shear stress data was examined to locate typical interacting or evolving waveforms. Due to the limited amount of data provided by the two film thickness probes, determining the evolutionary character of waveforms was difficult. However, several types of wave shapes appeared frequently, although their individual dimensions varied considerably. Four waveforms were chosen as representative of the large wave structures, each having peak thicknesses greater than twice the surrounding substrate thickness. In addition, each was preceded by a reasonably smooth substrate, shown by wall shear stress measurements to be free of acceleration.

Each measured film thickness profile was converted from the time domain into a spatial domain for use with the numerical algorithm. Wave peak passage times between probes were used to estimate "wave velocities"—these values provided initial estimates for the numerical computations.

NUMERICAL METHOD

Solution of free boundary problems requires methods for both hydrodynamic calculations and shape determination. The velocity and pressure fields within the wave were determined by solving the Navier–Stokes equations in primitive variable form. For a film Reynolds number of 880, the wave thickness generally was $<1\%$ of the pipe radius and therefore, a two-dimensional cartesian coordinate system was chosen. The transformation of time traces of film thickness to this coordinate system comprised the shape determination portion of the overall algorithm. The common method of computing the free surface position is to compute film thickness values at fixed streamwise locations. The present work inverts this procedure; for a measured sequence of film thickness values, streamwise locations associated with each value are determined such that the resulting shape and flow field within satisfies all interfacial boundary conditions.

To develop the methodology for treating evolving films, waves were initially modeled as though their shape remained constant with time—these waves are termed solitary. A new streamwise coordinate, z, is fixed on the front of the wave and extends in the opposite direction of gravity. The film thickness profile in the time domain, $h(t_i)$, was converted to the length domain, $h(z_i)$, through the transformation

$$z_i = z_0 + V_w(t_i - t_0), \tag{1}$$

for i ranging from 1 to the number of film thickness points in the isolated wave. Through this transformation, the wave profile was "stretched" for use as a computational domain, and time was removed from the problem. In this coordinate system, the wave remains fixed, and the wall moves upward at a constant speed given by V_w, the wave velocity for the solitary wave.

It is useful to define a new streamwise velocity component,

$$u(z, y) = -u'(x, y, t) + V_w, \tag{2}$$

where $u'(x, y, t)$ is the streamwise velocity in a coordinate system fixed on the wall. The governing equations for this viscous, incompressible and isothermal flow relative to the moving wave become

$$u\frac{\partial u}{\partial z} + v\frac{\partial u}{\partial y} = -\frac{1}{\rho}\frac{\partial P}{\partial z} - g + \nu\left(\frac{\partial^2 u}{\partial z^2} + \frac{\partial^2 u}{\partial y^2}\right), \tag{3}$$

$$u\frac{\partial v}{\partial z} + v\frac{\partial v}{\partial y} = -\frac{1}{\rho}\frac{\partial P}{\partial y} + \nu\left(\frac{\partial^2 v}{\partial z^2} + \frac{\partial^2 v}{\partial y^2}\right) \tag{4}$$

and

$$\frac{\partial u}{\partial z} + \frac{\partial v}{\partial y} = 0, \tag{5}$$

where v is the velocity in the normal (y) direction, P is the pressure, g represents gravitational acceleration and ν and ρ are the kinematic viscosity and density of the fluid, respectively. At the stress-free interface, $y = h(z)$, tangential and normal stress balances require

$$\left(\frac{\partial u}{\partial y} + \frac{\partial v}{\partial z}\right)\left[1 - \left(\frac{dh}{dz}\right)^2\right] - 2\frac{dh}{dz}\left(\frac{\partial u}{\partial z} - \frac{\partial v}{\partial y}\right) = 0 \tag{6}$$

and

$$P = \sigma\frac{\dfrac{d^2h}{dz^2}}{\left[1 + \left(\dfrac{dh}{dz}\right)^2\right]^{3/2}} + \frac{2\mu}{1 + \left(\dfrac{dh}{dz}\right)^2}\left[\frac{\partial u}{\partial z}\frac{dh^2}{dz} - \left(\frac{\partial u}{\partial y} + \frac{\partial v}{\partial y}\right)\frac{dh}{dz} + \frac{\partial v}{\partial y}\right], \tag{7}$$

where σ is the surface tension coefficient and μ is the absolute viscosity. At the wall, $y = 0$,

$$u = V_w, \qquad v = 0, \tag{8}$$

represent the standard no-slip and no-flux conditions.

Velocities at the interface are related through the kinematic condition in a moving frame,

$$v = u\frac{dh}{dz}. \tag{9}$$

The inlet velocity profile is parabolic, representing an acceleration-free falling film, while a sufficient and physically consistent outlet condition for a solitary wave requires a zero streamwise derivative for all variables. The variable V_w replaces $h(z)$ as the final variable to be iteratively determined in the free surface problem.

For each wave profile, a unique, non-uniform finite difference grid mesh was constructed. The mesh for a typical domain is shown in figure 3. The particular wave shape determined the grid spacing used. Mesh refinement continued until no further change in either the computed wave velocity or wall shear stress profile was observed. Of particular importance was the concentration of cells near the front of the wave, since the velocity fields change drastically in this region due to the large interfacial slope. In addition, large curvatures exist at each peak and trough. To insure adequate resolution of capillary pressure induced effects, grids were concentrated near the free interface in these regions. For most waves, 1800 cells of dimension $\delta x\,\delta y$ were sufficient, and produced grid Reynolds numbers [$\mathrm{Re}_{Gx} = u(z, y)\,\delta x/\nu$, $\mathrm{Re}_{Gy} = v(z, y)\,\delta y/\nu$] of order 1 in the y direction, and ranging from 1 to 100 in the streamwise direction.

The curved interface was accomodated by allowing boundary cells to be cut by the boundary, $h(z)$, thus reducing their volume. This situation is illustrated in figure 4. This technique produced areas adjoining two boundary cells, the centers of which were outside the computational domain. As the stress-free interface requires a zero normal derivative of the velocity vector with respect to the boundary, $h(z)$, these regions were treated as inviscid channels through which all fluid leaving one boundary cell on its shared side passed into the neighboring cell through its respective shared side. The total area of these regions represents <0.1% of the total domain, and had little effect on the results.

The equation set was solved on a finite difference grid using a variant of the TEACH-T code (Gosman *et al.* 1969), incorporating the SIMPLER pressure/continuity solution procedure; the principles of this method are described in detail elsewhere (Patankar 1980). The domain includes regions of significant streamwise variation in all variables, thus necessitating an accurate method of discretizing convective momentum terms. The simplest method of convective discretization, upwind differencing, ensures a reasonably stable numerical solution, but introduces numerical diffusion in regions of the flow where streamlines are oblique with respect to the grid lines (Raithby 1976). More importantly, the upwind scheme lacks sensitivity to cross-stream diffusion and source terms (Leonard 1979), which are of tremendous importance in the case of a thin film.

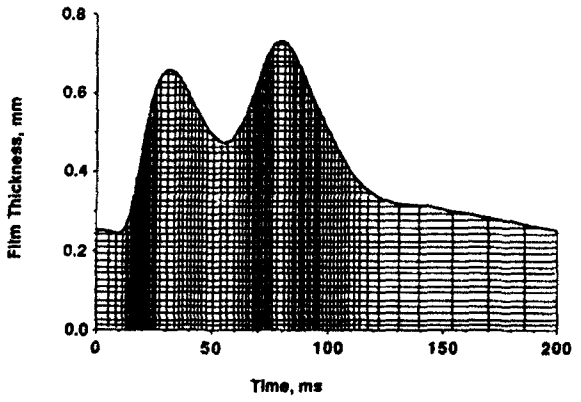

Figure 3. Sample finite difference grid.

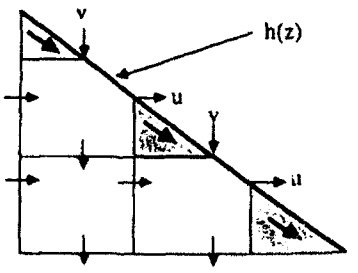

Figure 4. Interface finite difference grid.

This lack of sensitivity diminishes the effects of the y direction diffusion as well as the "v" velocity in the solution of the streamwise velocity. These deficiencies in the upwind and hybrid methods require the use of a QUICK-based scheme, which improves acccuracy by expanding the number of neighboring points included in interpolated values of velocity. Based on Leonard's (1979) third-order accurate discretization scheme QUICK, Pollard & Siu (1982) developed the QUICK-ER (Extended and Revised) method of discretizing convective terms. The QUICK-ER method overcomes stability problems inherent in the QUICK procedure at the expense of slower convergence, and is considered the most satisfactory method of handling convective momentum terms (Huang *et al.* 1985). For application to non-uniform grids, a new version of QUICK-ER was developed. This method follows the spirit of the QUICK-ER formulation, but includes locally variable weighting factors to account for the non-uniformity of the grid in both directions. Although QUICK-ER schemes requires more computational effort per iteration than upwinding, particularly for non-uniform grids, improvements in accuracy allow the use of a slightly coarser grid, so total computational time exceeds that required by the upwind method by only 20%.

The solution procedure began with choosing a value for V_w and creating the transformed domain, given by [1]. The u velocity field was set to a parabolic profile everywhere, and the v velocity field was set to zero. The pressure at each z location was set to the surface pressure due to curvature. Updated velocity and pressure fields within the wave were then computed using [3]–[5]. Through interpolation for the velocity gradients in the interfacial shear stress balance, [6], streamwise and normal velocities in the interior of the flow field were used to derive an expression for the streamwise surface velocity. Coupled with the kinematic condition [9], the velocities on the surface were known for each iteration. The surface pressure computed from [7] was used to determine the first pressure value in the interior of the domain through the use of parabolic interpolation using the surface pressure and two interior pressures. With the newly computed surface variables, the velocity and pressure fields were updated until the sum of residuals of mass and momentum (normalized by the inlet quantities) over the domain was $<10^{-3}$. In addition, the interfacial shear and normal stress balances were required to be within 10^{-2} Pa of zero.

The free boundary shape was determined by examining the converged average outlet pressure in the flat film section. If the average pressure did not approach zero, as required for a non-accelerating film trailing a solitary wave, a new value of V_w was chosen and the process repeated. The adjustment procedure for V_w was simple—if the pressure in the outlet section was higher than zero, the wave (wall) velocity was too high, since the wall was pushing excess fluid through the wave, and a positive pressure at the outlet was opposing this extra fluid in an attempt to satisfy the mass balance for the wave.

The numerical study of evolving or interacting waves retains much of the methodology developed for solitary waves, differing only in the wave shape determination. Examination of the experimental measurements of film thickness reveals the large waves change rapidly between the upper and lower film thickness probe. The waves appear to change from solitary type waves by being perturbed by locally variable mass and momentum sources, physically recognized as small waves. Incorporating this unsteady effect is accomplished through the use of a locally constant stretching parameter, as opposed to the globally constant value used for the classical solitary wave. The domain transformation for this case is given by

$$z_i = z_0 + V_{w,i}(t_i - t_0), \qquad [10]$$

where z is the streamwise coordinate fixed on the wave front. In general, this pseudo wave velocity is

$$V_{w,i} = V_w[1 + e(z_i)], \qquad [11]$$

where $e(z_i)$ is an iteratively determined local stretching variable and V_w represents the wave velocity associated with the substrate. The solitary wave case is recovered by setting $e(z_i) = 0\ \forall i$. As before, we define a new streamwise velocity component as

$$u(z, y) = -u'(x, y, t) + V_w(z_i). \qquad [12]$$

This transformation introduces locally variable mass and momentum sources into the u momentum and continuity equations [3] and [5], which become

$$u\left(\frac{\partial u}{\partial z}+\frac{\mathrm{d}V_w}{\mathrm{d}z}\right)+v\frac{\partial u}{\partial y}=-\frac{1}{\rho}\frac{\partial P}{\partial z}-g+\nu\left(\frac{\partial^2 u}{\partial z^2}+\frac{\partial^2 u}{\partial y^2}-\frac{\mathrm{d}^2 V_w}{\mathrm{d}z^2}\right) \quad [13]$$

and

$$\frac{\partial u}{\partial z}+\frac{\partial v}{\partial y}-\frac{\mathrm{d}V_w}{\mathrm{d}z}=0. \quad [14]$$

The interfacial stress conditions [6] and [7] are modified slightly by the unsteady effects, and become

$$\left(\frac{\partial u}{\partial y}+\frac{\partial v}{\partial z}\right)\left[1-\left(\frac{\mathrm{d}h}{\mathrm{d}z}\right)^2\right]-2\frac{\mathrm{d}h}{\mathrm{d}z}\left(\frac{\partial u}{\partial z}-\frac{\partial v}{\partial y}-\frac{\mathrm{d}V_w}{\mathrm{d}z}\right)=0 \quad [15]$$

and

$$P=\sigma\frac{\dfrac{\mathrm{d}^2 h}{\mathrm{d}z^2}}{\left[1+\left(\dfrac{\mathrm{d}h}{\mathrm{d}z}\right)^2\right]^{3/2}}+\frac{2\mu}{1+\left(\dfrac{\mathrm{d}h}{\mathrm{d}z}\right)^2}\left[\left(\frac{\partial u}{\partial z}-\frac{\mathrm{d}V_w}{\mathrm{d}z}\right)\frac{\mathrm{d}h^2}{\mathrm{d}z}-\left(\frac{\partial u}{\partial y}+\frac{\partial v}{\partial y}\right)\frac{\mathrm{d}h}{\mathrm{d}z}+\frac{\partial v}{\partial y}\right]. \quad [16]$$

The normal stress balance, [16], was found to be insensitive to the additional term, $\mathrm{d}V_w/\mathrm{d}z$, and the term was removed from the formulation. The solution procedure for the pseudo-unsteady equations [13], [4] and [14], subject to [15] and [7]–[9], is identical to that of the solitary wave, with the exception that now a profile of $V_{w,i}$ must be specified instead of a single value. When the velocity and pressure fields have converged for a given set of $V_{w,i}$, the wave shape is adjusted through $e(z_i)$ to meet two criteria. The baseline wave velocity, V_w, is adjusted such that the average pressure in the flat outlet section approaches zero, as before. The computed wall shear stress profile is then compared to the experimental profile, and adjustments made to $e(z_i)$ to correct deviations. Upon arriving at the correct distribution of $e(z_i)$, the solution includes the velocity and pressure fields within the wave, as well as the relative extents of its evolution throughout the wave. Each solution is unique, and the wall shear stress matching procedure insures the accuracy of the velocity fields.

The procedure developed for the solitary waves required an average of 300 iterations of the velocity and pressure fields to converge, with an under-relaxation factor of one-half used for all variables. Between 4 and 8 adjustments to the solitary wave velocity were required to produce a flow with an average outlet pressure $<10^{-2}$ Pa. For the quasi-unsteady case, roughly 500 iterations were required to achieve convergence of the velocity and pressure fields, due to the extra stiffness imposed by the multiple peaks and valleys. Adjustment of the variable wave velocity to match the wall shear stress data took anywhere from 20 to 40 iterations.

The program was coded in FORTRAN 77, and required 2 mbyte of task space. Execution times for convergence of the velocity and pressure fields for a given wave shape were approx. 5 CPU h on a VAX 11-750.

RESULTS

This study concentrated on waves developing from or interacting with isolated waves, identified by comparing film thickness measurements from both upper and lower probes. Examination of the experimental film thickness data shows that many large waves fall into three categories. While nearly solitary waves exist, few are free from small wave induced ripples, an example of which is shown in figure 5. As the wave travels from the upper to the lower probe, the small hump on the wave tail grows, while the wave front retains its structure; we classify this wave as type A. Large waves appear susceptible to splitting when perturbed, as illustrated in figure 6. These waves, classified as type B, cover a large portion of the interface, and suggest that modeling falling films far from the inlet as steady processes neglects important dynamics. The interaction of two large waves of unequal size is shown in the wave trace in figure 7. Although significantly smaller, the trailing wave seen in the upper trace either passes through the larger wave or accumulates a larger

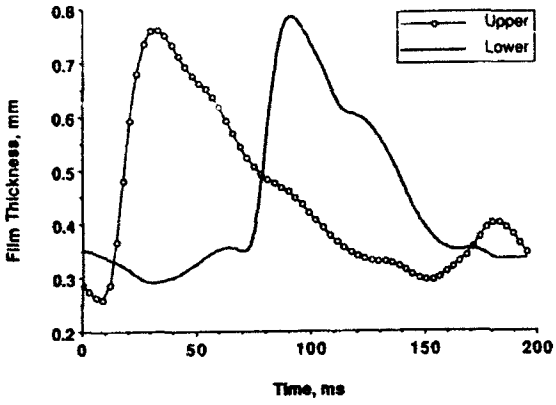

Figure 5. Evolution of a nearly solitary wave: type A.

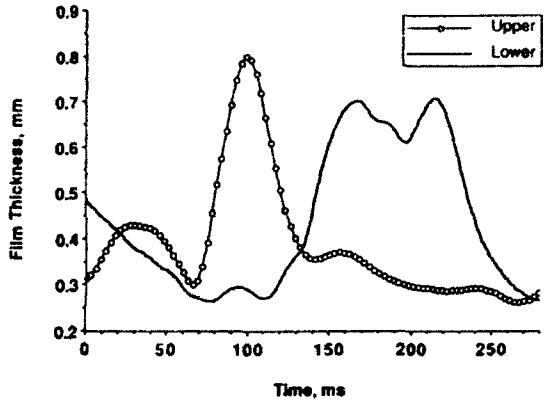

Figure 6. Evolution of a large wave via splitting: type B.

portion of its mass, leading to a situation classified as type C. While each of these cases characterizes a significant fraction of the interface, combinations of these effects are also seen. Figure 8 illustrates the splitting of a large wave coupled with the interaction of the large wave with a small wave preceding it. This type D wave is not representative of all complicated waves, but serves as an example of the combination of evolution and interaction effects.

Description of large waves is generally limited to peak and substrate thicknesses and wavelengths. Experimental data is limited to two time traces of film thickness, which makes quantitative evaluation of these variables difficult. It must suffice to characterize the extent of evolution by the time separation of individual peaks, while the relative mass of each peak is estimated on the basis of the peak thickness. In conjunction with the numerical predictions of flow fields, these data offer new insight into the hydrodynamic processes occurring in the large waves.

Streamlines computed for the type A wave are shown in figure 9. The presence of a large recirculation region is seen within the peak of the wave when viewed in a coordinate system fixed on the wave. The interaction of this large mass of fluid with the surrounding substrate results in regions of strong streamwise acceleration ahead and behind the region. These results were also seen in studies of nearly solitary waves with similar peak/substrate thickness ratios (Wasden & Dukler 1989). The presence of the growing hump on the wave tail increases the size of the recirculation region, compared to a solitary wave, which causes larger disruptions in the substrate as the wave peak passes over. The wall shear stress profile for this wave is shown in figure 10, along with experimental values. Agreement is excellent over most of the wave—the experimental values at the tail suggest outside or cross-stream disturbances are present. This discrepancy is not expected to significantly alter the overall flow field, as the region under the peak is insensitive to downstream disturbances at Re = 880. Matching the wall shear stress data required stretching the wave shape in transforming it from the time domain to the spatial domain, as shown in figure 11. The transformation required that the entire wave stretch in length, compared to a purely solitary wave; the magnitude of $e(z_i)$, [11], is shown in figure 11. Of special interest is the extra stretching caused by the presence of the hump on the tail—previous studies of nearly solitary waves (Wasden & Dukler 1989) show the evolution is confined to the region very near the peak, while in this case, the tail region is stretching as well. From a substrate wave velocity of 1.10 m/s, the wave velocity $V_{w,i}$, [11], increased to 1.89 m/s near the peak. The average, or Nusselt, film velocity for this Re (Kapitza 1964) is 0.51 m/s, showing the wave moves at between 2.1 and 3.7 times the average velocity. The combination of experimental observations and numerical simulations show that the wave is in the early stages of splitting, and that this effect, although seemingly slight upon examining the film thickness measurements, significantly affects the flow field.

Flow within a wave with the peak splitting into daughter waves is shown in figure 12. The flow beneath each peak resembles that seen in the nearly solitary wave A. The recirculating region encloses the entire area under the twin peaks, and again causes large accelerations near the front and rear of the wave. The remnants of the original solitary wave recirculation region are seen at

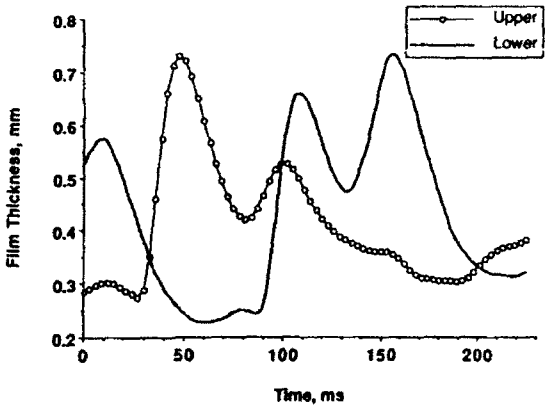

Figure 7. Interaction of large waves: type C.

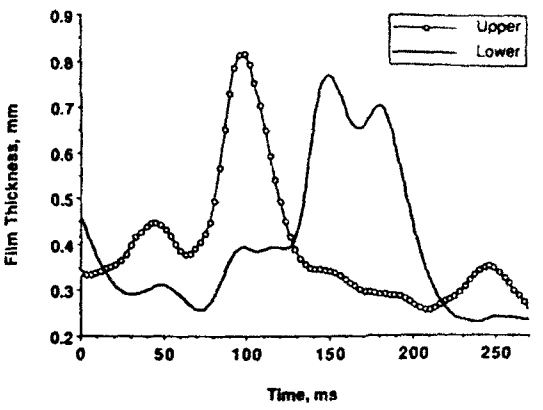

Figure 8. Evolution and interaction of large waves: type D.

the front of the wave, with the newly formed rear peak having a smaller recirculation region, even though it has a roughly equivalent peak thickness. This observation demonstrates the danger of classifying multiple waves based solely on the easily measured parameters such as peak thicknesses and separation time. Comparison of computed and measured wall shear stress is shown in figure 13 to be excellent. The peak in wall shear stress preceding the first peak in film thickness is similar to that observed in an isolated wave, showing how the evolving wave retains part of its original traits. The second shear stress peak is a further indication of the emergence of a new peak. The domain and stretching parameter variation for this wave are shown in figure 14. The stretching parameter was varied such that the peaks were evolving most rapidly, with the trough moving slower than either peak. As expected, the second peak was moving slightly ($\approx 10\%$) slower than the first. The substrate wave velocity was 1.32 m/s, yielding $V_{w,i}$ from 1.32 to 1.91 m/s under the peaks. Compared to the Nusselt velocity, the wave moves roughly 2.6–3.8 times faster.

Flow in an interacting wave sequence is shown in figure 15. The two waves appear to have independent recirculation regions, with the first preceded by the characteristic acceleration region. The size of the recirculation zones appears to be related to the thicknesses of the individual peaks, in contrast to the evolving case, type B. This may result from the extra separation that exists in this case, causing speculation that the type B wave would evolve into a wave similar to type C. Shear stress profiles for the interacting case are displayed in figure 16. The agreement between computed and measured shear stress is excellent, and shows two peaks in shear stress, indicating the wave is evolving into two nearly solitary waves. As the wave peaks separate further, the second wall shear stress peak is closer in magnitude to that expected of an isolated wave, additional evidence of future disintegration of the original wave. The transformed domain and stretching parameter variation are shown in figure 17. Both peaks were evolving at a nearly identical rate, suggesting the effect of the interactions on the natural evolution of the wave was slight. As was

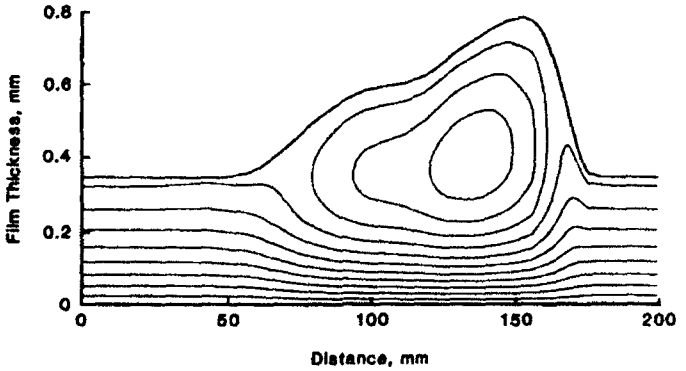

Figure 9. Streamline map: wave A.

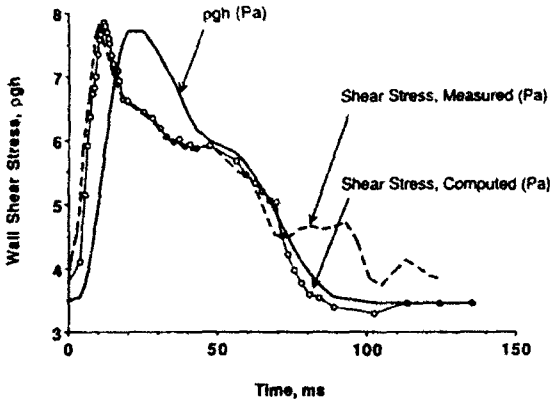

Figure 10. Shear stress comparison: wave A.

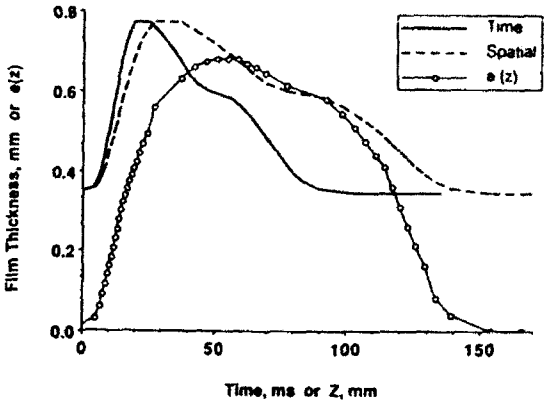

Figure 11. Experimental and computed wave shape: wave A.

previously the case, the trough between the waves was stretching more slowly than the peak regions. The substrate wave velocity was 1.12 m/s, closer to the solitary wave (A) than the splitting wave (B). The wave velocity, $V_{w,i}$, varied from 1.12 to 1.7 m/s under the peaks, roughly 2.1–3.3 times the Nusselt velocity.

The most complicated waveform studied included the effects of evolution and interaction. Flow within this wave, classified as type D, is shown in figure 18. Apparently the interaction of the large wave structure with the small wave near the front has little effect on the overall flow pattern, compared to what occurs in simple evolving waves of this size (see figure 12). A region of moderate acceleration exists at the front of the small forerunner wave, followed by a region of nearly parallel flow. This flow profile suggests the effect of the initial interaction is limited to accelerating fluid away from the wall, and effectively changing the substrate thickness with which the large wave interacts. Further downstream, the large acceleration region is again evident, due to the interaction of the large recirculation region with the slowly moving substrate. As the wave has only begun to evolve, the recirculation region is reminiscent of that associated with a stretched isolated wave, although the area near the trough of the wave implies future separation of the waves. Shear stress data for this wave is shown in figure 19; agreement between the measured and computed values is excellent over the entire wave. The shear stress profile provides further evidence of the dampening effect of the interaction of the large wave with the small forerunner wave. The maximum shear stress preceding the large wave peak is smaller (relative to ρgh) than existed in the previous cases. This may be due to the relative difference in size between the wave peak and the local substrate—previously, wave peak/substrate ratios were ≈ 3, while the ratio between the first peak and the plateau preceding it, in this case, is <2. Since the splitting of the peaks has just begun, no significant secondary peak in shear stress exists. The transformed domain and stretching

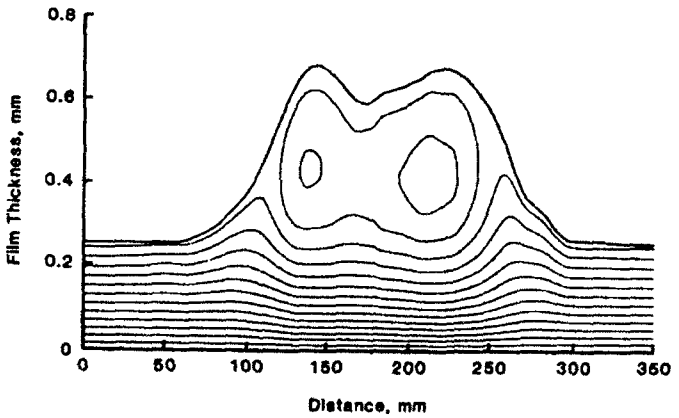

Figure 12. Streamline map: wave B.

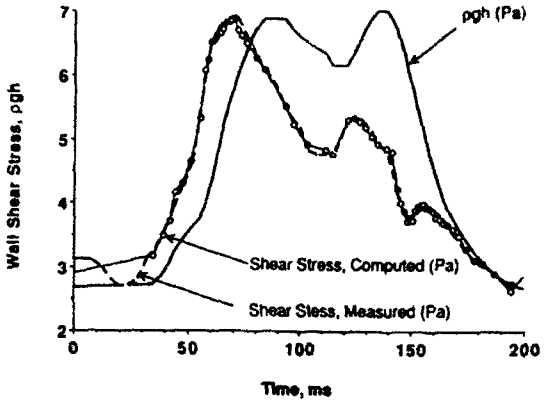

Figure 13. Shear stress comparison: wave B.

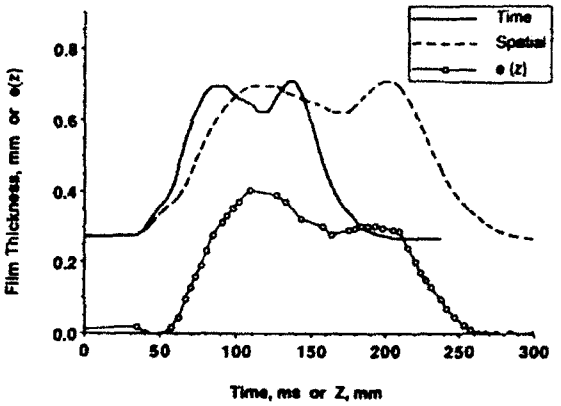

Figure 14. Experimental and computed wave shape: wave B.

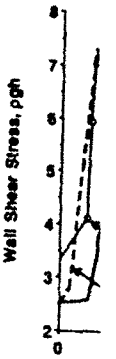

Figu

parameter variation are shown in figure 20, and are similar to cases B and C. Evolution of the forerunner wave is significant; the wave is stretching out in response to the mass descending on it. As before, the second peak is moving slightly slower than the first ($\approx 5\%$); from data shown in case B, the difference is expected to increase with the extent of evolution. From a substrate wave velocity of 1.24 m/s, the wave velocity $V_{w,l}$ increased to 1.89 m/s under the peak, ranging from 2.4 to 3.8 times the Nusselt velocity.

fluid the
the wave
between
and mass
of the en
compare
having tv

SUMMARY AND CONCLUSIONS

Interacting or evolving large waves comprise a large portion of the interface of a falling liquid film. Wave amplitudes of 2–5 times the substrate thickness are common even for moderate Reynolds numbers, ruling out models based on small perturbation theory. From film thickness measurement time traces, four representative large waves were selected as comutational domains for a numerical solution of the Navier–Stokes equations. Computed results included velocity and pressure fields, as well as the wave shape necessary to match shear stress measurements. Values of $V_{w,l}$ [11], remain near those expected for solitary waves with similar peak and substrate thicknesses, as reported by Wasden & Dukler (1989). The stretching technique developed for this study allowed simple accomodation of local unsteady effects by decoupling the hydrodynamic and shape determination problems. An interesting extension of the present work would be to measure the film thickness at several closely spaced locations, and attempt to compute $e(z)$ from the data.

The bulk of the liquid in large interacting or evolving waves is carried in the region above the substrate, and is nearly stationary in a coordinate system moving with the wave. As the wave moves rapidly over the slow substrate, it causes acceleration of fluid from the front into the peak. The

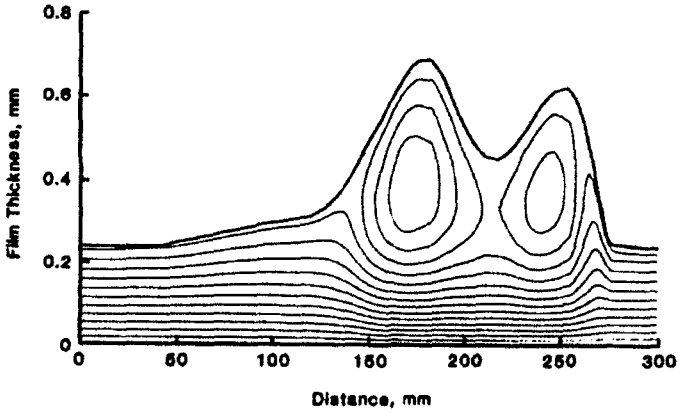

Figure 15. Streamline map: wave C.

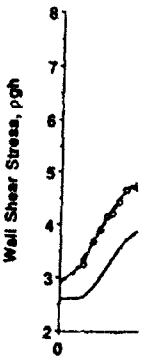

Figure 19

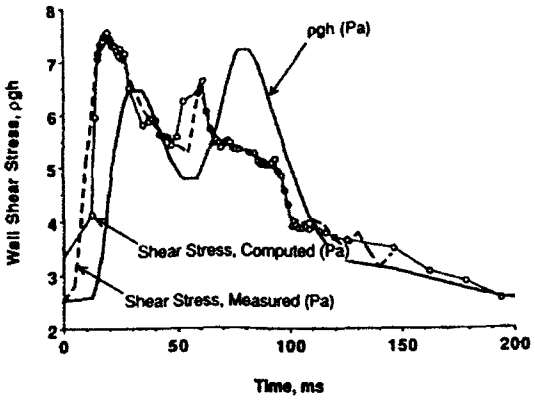

Figure 16. Shear stress comparison: wave C.

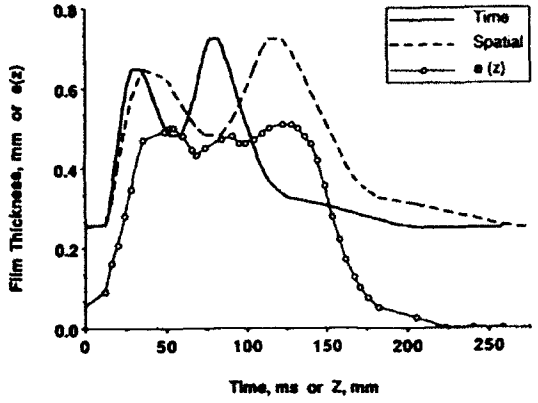

Figure 17. Experimental and computed wave shape: wave C.

fluid then decelerates as it passes out of the wave tail, generating a closed recirculation region in the wave peak. Waves with multiple peaks have multiple regions of recirculation, with mixing zones between them. These regions occur only in multiple-peak waves, and may be responsible for heat and mass transfer enhancement above that due to fluid acceleration and circulation. The magnitude of the enhancement due solely to multiple wave interactions is unknown, but may be significant compared to that associated with isolated large waves. The computations were limited to waves having two peaks, but these results are expected to extrapolate well for cases of more than two

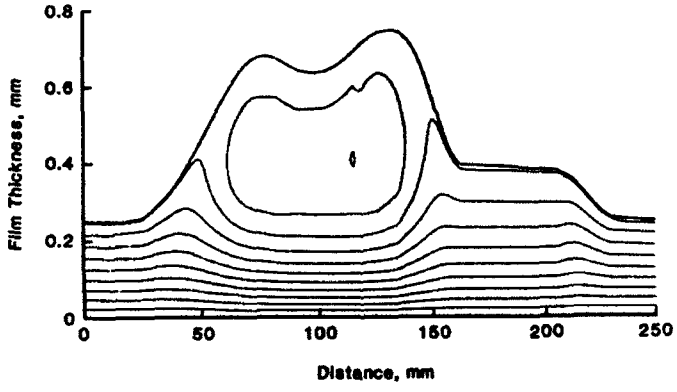

Figure 18. Streamline map: wave D.

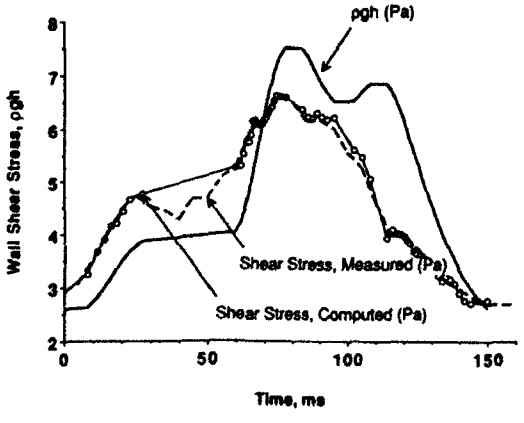

Figure 19. Shear stress comparison: wave D.

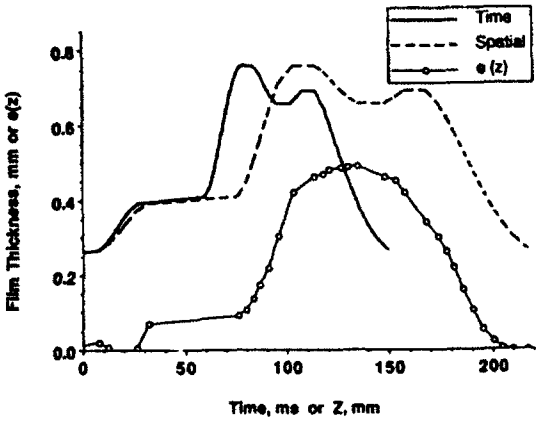

Figure 20. Experimental and computed wave shape: wave D.

peaks. As a majority of the surface is covered by evolving or interacting waves, further efforts toward determining relative effects of competing hydrodynamic processes is justified.

Perhaps the most surprising result of this study concerned the similarity between flow fields resulting from the interaction of large waves and those generated by the splitting of a large wave into two waves. This similarity suggests the shape of the interface controls the fluid dynamics within, regardless of the evolutionary process from which the wave resulted. This may simplify further analyses of transport processes, and allow characterization based primarily on peak and substrate thicknesses, as well as separation times.

Modeling large wave interactions will require the use of velocity profiles capable of representing the large streamwise accelerations existing in the flow. Previous work (Wasden & Dukler 1989) has shown a cubic polynomial reasonably approximates the normal (y) variation of the streamwise velocity at all axial locations: its use for modeling the evolution of large waves is recommended.

Acknowledgements—Financial support for this research by the Office of Naval Research is gratefully acknowledged. One of the authors (F.K.W.) was supported by a National Science Foundation Graduate Fellowship.

REFERENCES

BACH, P. & VILLADSEN, J. 1984 Simulation of the vertical flow of a thin wavy film using a finite-element method. *Int. J. Heat Mass Transfer* **27**, 815–827.

BROWN, R. C., ANDREUSSI, P. & ZANELLI, S. 1978 The use of wire probes for the measurement of liquid film thickness in annular gas–liquid flows. *Can. J. chem. Engng* **56**, 754–757.

DUKLER, A. E. 1972 Characterization, effects and modelling of the wavy gas–liquid interface. *Prog. Heat Mass Transfer* **6**, 207–223.

DUKLER, A. E. 1977 The role of waves in two phase flow: some new understanding. *Chem. Engng Educ.* **1976**, 108–138 (Award Lecture).

GOSMAN, A. D., PUN, W. M., PUNCHAL, A. K., SPALDING, D. B. & WOLFSTEIN, M. 1969 *Heat and Mass Transfer in Recirculating Fluid Flow*. Academic Press, London.

HANRATTY, T. J. & CAMPBELL, J. A. 1983 Measurement of wall shear stress. In *Fluid Mechanics Measurements* (Edited by GOLDSTEIN, R. J.), pp. 559–617. Hemisphere, Washington, D.C.

HUANG, P. G., LAUNDER, B. E. & LESCHZINER, M. A. 1985 Discretization of nonlinear convection processes: a broad-range comparison of four schemes. *Comp. Meth. appl. mech. Engng* **48**, 1–24.

KAPITZA, P. L. 1964 Wave flow of thin layers of a viscous fluid. In *Collected Papers of P. L. Kaptiza*, Vol II. Macmillan, New York.

KHESHGI, H. S. & SCRIVEN, L. E. 1987 Disturbed film flow on a vertical plate. *Phys. Fluids* **30**, 990–997.

LEONARD, B. P. 1979 A stable and accurate convective modelling procedure based on quadratic upstream interpolation. *Comp. Meth. appl. mech. Engng* **12**, 59–98.

MAO, Z.-X. & HANRATTY, T. J. 1985 The use of scalar transport probes to measure wall shear stress in a flow with imposed oscillations. *Expts Fluids* **3**, 129–135.

PATANKAR, S. V. 1980 *Numerical Heat Transfer and Fluid Flow*. Hemisphere, Washington, D.C.

POLLARD, A. & SIU, A. L. W. 1982 The calculation of some laminar flows using various discretisation schemes. *Comp. Meth. appl. mech. Engng* **35**, 293–313.

RAITHBY, G. D. 1976 A critical evaluation of upstream differencing applied to problems involving fluid flow. *Comp. Meth. appl. mech. Engng* **9**, 75–104.

WASDEN, F. K. & DUKLER, A. E. 1989 Insights into the hydrodynamics of free falling films. *AIChE Jl* **35**, 187–196.

ZABARAS, G. J. 1985 Studies of vertical, annular gas–liquid flow. Ph.D. Dissertation, Univ. of Houston, Tex.

ZABARAS, G. J., MARON, D. M. & DUKLER, A. E. 1986 Vertical upward concurrent gas–liquid annular flow. *AIChE Jl* **32**, 829–843.